

NONLINEAR OPTICS IN THIN FILM INTERFERENCE COATINGS

VON DER FAKULTÄT FÜR MATHEMATIK UND PHYSIK
DER GOTTFRIED WILHELM LEIBNIZ UNIVERSITÄT HANNOVER

ZUR ERLANGUNG DES AKADEMISCHEN GRADES
DOKTOR DER NATURWISSENSCHAFTEN

DR. RER. NAT.

GENEHMIGTE DISSERTATION VON
M.SC. MORTEN STEINECKE

2023

Referent: Prof. Dr. Detlev Ristau
Korreferent: Prof. Dr. Uwe Morgner
Prof. Dr. Wolfgang Rudolph
Tag der Promotion: 12.07.2023

Kurzfassung

Nichtlineare optische Effekte spielen eine essenzielle Rolle in modernen optischen Systemen. Sie finden Anwendung in der Modenkopplung zur Erzeugung ultrakurzer Laserpulse, bei der Generation von Laserwellenlängen, die auf andere Weise nicht verfügbar wären und bei neuartigen Messverfahren. Die Implementierung der benötigten nichtlinearen optischen Prozesse basiert dabei auf konventionellen optischen Aufbauten aus einzelnen Komponenten in Freistrahlfunktionen, was die Möglichkeiten für Miniaturisierung und Integration von Funktionsgruppen limitiert. Im Gegensatz dazu sind optische Interferenzbeschichtungen ein hochentwickeltes Verfahren für die Kombination von optischen Funktionen in einzelne, monolithische Schichtsysteme aus transparenten Materialien. Bisher waren die Anwendungen von optischen Beschichtungen dabei auf den linearen Bereich der optischen Wechselwirkung beschränkt. Wenn nichtlineare optische Effekte berücksichtigt wurden, dann üblicherweise nur, um diese als unerwünschte Effekte zu unterdrücken.

Diese Arbeit untersucht daher die Kombination von ausgewählten nichtlinearen optischen Effekten mit speziell entworfenen optischen Beschichtungen. Ziel hierbei ist die Schaffung von neuartigen Komponenten, die als Alternative zu etablierten optischen Systemen fungieren können. Wegen der amorphen Struktur der Beschichtungsmaterialien, basieren die zwei betrachteten nichtlinearen Effekte auf der Suszeptibilität der dritten Ordnung $\chi^{(3)}$. Der erste Effekt ist der optische Kerr-Effekt, welcher genutzt wird, um einfallendes Licht ausschließlich optisch zu schalten. Im zweiten Fall werden optische Beschichtungen genutzt, um das Problem der Phasenanpassung bei Erzeugung der dritten Harmonischen in frequenzverdreifachenden Spiegeln zu lösen und so die Konversionseffizienz deutlich zu erhöhen. Für beide dieser Anwendungen werden die Herstellungsverfahren, die Untersuchung der benötigten optischen Materialien, sowie die experimentelle Überprüfung der hergestellten Komponenten präsentiert.

Die Untersuchungen haben gezeigt, dass die frequenzverdreifachenden Spiegel zwar die Konversionseffizienz deutlich steigern können, aktuell aber noch durch die Generation freier Elektronen sowie die daraus resultierenden Effekte limitiert werden.

Die optischen Schalter zeigen eine deutliche Modulation ihrer optischen Eigenschaften mit Änderungen der Transmission und Reflexion um etwa 20 % beziehungsweise 30 %. Der Modulationsprozess ist dabei ein reproduzierbarer Prozess, der klar von der laserinduzierten Zerstörung bei höheren Intensitäten unterschieden werden kann. Der geschaffene optische Schalter kann daher eine funktionale Alternative zu etablierten Schaltkonzepten darstellen.

Schlagwörter: Interferenzbeschichtungen, Erzeugung der dritten Harmonischen, optischer Schalter

Abstract

Nonlinear optical effects play a crucial role in modern optical systems. They are applied in mode-locking for the generation of ultrashort optical pulses, in the generation of otherwise unavailable wavelengths, or for new approaches in measurement techniques. However, implementing the required nonlinear optical processes mainly relies on conventional optical systems comprising separate components and free-space constructions, which limits the possibilities for miniaturization and integration of functional groups.

Contrary to this, optical interference coatings offer highly developed capabilities for combining optical functions into a single, monolithic stack of transparent materials. So far, the applications of optical coatings have generally been limited to the linear optical regime. If nonlinear effects were considered, it was mostly directed at their suppression to avoid undesired effects.

This thesis, therefore, investigates the combination of selected nonlinear optical effects with specially designed optical coatings to create novel components as alternatives to established optical systems. Due to the amorphous nature of thin film coating materials, the two effects chosen for investigation are based on the third-order susceptibility $\chi^{(3)}$. The first effect is the optical Kerr effect, which is utilized to achieve all-optical switching of incident light. In the second case, optical coatings are utilized to solve phase matching issues for the third harmonic generation in frequency tripling mirrors and significantly increase conversion efficiency. The manufacturing processes and material research are presented for both approaches, together with the experimental testing of the novel components' function.

It was found that while the frequency tripling mirrors provide a greatly enhanced efficiency compared to the third harmonic generated in more typical optical coatings, the total efficiency is currently limited by free-electron effects occurring during the conversion process. The optical switches show significant modulation of 20% in transmittance and 30% in reflectance with a repeatable process which can be clearly distinguished from laser-induced damage occurring at higher intensities. Therefore, the created optical switch can present a viable alternative to established switching concepts.

Key words: Interference coatings, third harmonic generation, optical switch

Contents

1	Introduction	1
2	Nonlinear optics	5
2.1	Third-order effects in isotropic materials	6
2.2	The optical Kerr effect	7
2.3	Third harmonic generation	9
2.3.1	Phase matching	10
2.4	Free-electron effects	14
2.4.1	Photoionization	15
2.4.2	Avalanche ionization	16
2.4.3	Relaxation	17
2.4.4	Influence of free electrons	18
3	Nonlinear refractive index of optical materials	21
3.1	Dielectric materials	21
3.2	Epsilon-Near-Zero materials	22
3.2.1	Excitation of free electrons	23
3.2.2	Enhancement of the electric field	24
3.3	Semiconductors	25
4	Thin film interference coatings	27
4.1	Dielectric coatings	27
4.1.1	Transfer-matrix-formalism	28
4.2	Band-pass designs	32
5	Kerr-band-switches	35
5.1	Optical switching with the Kerr effect	35
5.2	Calculation of intensity-dependent refractive indices in layer stacks . .	36
5.2.1	Simulation process	37
5.2.2	Simulation of single pulses	37
5.2.3	Figure of merit	41
5.2.4	Optimization of KBS designs	42

Contents

5.2.5	Beam profile considerations	45
6	Frequency tripling mirrors	47
6.1	Third harmonic generation in thin film coatings	47
7	Manufacturing of thin film coatings	51
7.1	Ion beam sputtering	52
7.1.1	Monitoring of the deposition process	53
7.2	Coating of Kerr-band-switches	56
7.3	Coating of frequency tripling mirrors	57
7.3.1	High-resolution broadband-monitor	58
7.3.2	Coating stability considerations	59
8	Manufacturing and characterization of active materials	63
8.1	Indium tin oxide	63
8.1.1	Deposition process and thermal treatment	63
8.1.2	Characterization methods	64
8.1.3	Structural investigations	66
8.1.4	Index of refraction and extinction coefficient	67
8.1.5	Electrical properties	69
8.1.6	Laser-induced damage threshold	70
8.2	Gallium arsenide	72
8.2.1	The concept of GaAs-KBS	72
8.2.2	Manufacturing of GaAs-KBS	73
9	Experimental setups	75
9.1	Characterization of frequency tripling mirrors	75
9.2	Measurement of the nonlinear refractive index	76
9.3	Measurement of optical switching	80
9.3.1	LIDT measurement	84
10	Results and discussion	87
10.1	Frequency tripling mirrors	87
10.2	Nonlinear refractive index	91
10.2.1	ITO	91
10.2.2	GaAs	92
10.3	Kerr-Band-Switches	93
10.3.1	Optical switching	93
10.3.2	Thermal effects	98

Contents

10.3.3 Relation to the LIDT	99
11 Conclusion and outlook	101

1 Introduction

Shortly after the invention of lasers by Maiman in 1960, [1], the newly available, intense electromagnetic fields enabled the measurement of the second harmonic generation by Franken *et al.* in 1961 [2], and with that, one of the first observations of a nonlinear optical effect. Since then, nonlinear optics has grown into a large field of modern optics and continues to be the subject of fundamental research.

Nonlinear optical processes are utilized in the generation of higher harmonics, which are applied in the investigation of highly charged ions [3], squeezed light exploited in highest sensitivity gravitational wave detectors depends on parametric down-conversion [4], and Raman-spectroscopy based on four-wave mixing is applied in medical imaging [5]. The more established nonlinear processes are widespread in industrial applications. For example, commercial as well as research-grade ultrashort pulsed lasers often rely on the optical Kerr effect, a nonlinear optical effect caused by the third-order susceptibility, for mode-locking to achieve sub-picosecond pulses [6, 7]. The second harmonic generation, as well as the closely related processes of sum- and difference-frequency generation, are utilized in accessing laser wavelengths away from classical laser wavelengths in the near-infrared.

However, most nonlinear optical processes in research and industry rely on conventional optical setups with individual, macroscopic components. Commercial kits for frequency conversion, for example, consist of individual crystals, waveplates, and polarizers [8]. Although an arrangement like this can provide a high degree of flexibility in the alignment of the single components, it is not suited for miniaturized, integrated optical systems required in the future. Utilizing the unique properties of optical interference coatings could mitigate these disadvantages of classical optical setups.

Optical coatings have been utilized to enhance the function of optical components since antiquity. An early example are metal-coated mirrors already known in Rome of the first century A.D. [9]. While these metal coatings for mirrors were perfected over centuries [10], coatings based on interference effects in dielectric materials were developed only around the beginning of the 20th century [11, 12]. These coatings allow a much higher degree of flexibility with regard to anti- and high-reflective

1 Introduction

properties by stacking different transparent materials. Various manufacturing processes and techniques have been in development since then.

Today, optical interference coatings are essential to optical systems and setups. They are used in state-of-the-art research applications to precisely control the group delay dispersion for ultrashort pulsed, high-power laser systems [13] or provide the smallest possible losses in gravitational wave detectors [14]. Further drive for development in optical coatings is provided by new applications in quantum technologies [15] and the desire for integration of optical systems. However, most applications of optical coatings are limited to the linear regime of optics. When nonlinear effects in optical coatings are considered, they are mostly the source of absorption or even laser-induced damage and, therefore, avoided whenever possible.

In this thesis, the utilization and integration of different nonlinear effects in optical interference coatings are investigated. As optical coatings are almost exclusively made up of amorphous materials, the nonlinear optical effects available for the intended applications are limited to those caused by oddly numbered orders of the susceptibility. Therefore, and with regard to the efficiency of the desired effects, only third-order nonlinearities are considered. The investigations are focused on two closely related optical effects:

The first effect under consideration is the optical Kerr effect. This effect is known to cause a change in the index of refraction of optical materials under intense electromagnetic radiation. The deviation in the refractive index n from its undisturbed value n_0 depends on the incident intensity I and the nonlinear refractive index n_2 , a parameter of each optical material. This effect is already applied to deliberately change the properties of optical systems, and the integration into thin film coatings with their freedom of design with regard to spectral properties and internal intensity distribution has excellent potential.

One aspect that could significantly impact future optical systems is the possibility of an efficient, ultrafast optical switch. This novel component could be integrated into laser cavities as mode-locking device or function as a safety module, passively limiting the transmitted intensity.

The second effect investigated in this thesis is the generation of the third harmonic of infrared lasers. Currently, direct third harmonic generation is difficult to achieve due to the challenges related to phase matching. By exploiting the potential for phase control inherent in optical coatings, these challenges can be overcome with special coating designs. The internal intensity enhancement caused by interference in thin film coatings can then be utilized to increase the efficiency of the conversion further. This part of the thesis was done in cooperation with the University of New

Mexico and the Leibniz University Hannover, so only a part of the total work related to manufacturing and material-related issues will be presented here.

For investigation of these two concepts, this thesis will firstly discuss the necessary foundation of nonlinear optics in isotropic media as well as the generation and effects of free electrons in Chapter 2 and go into more detail about the optical Kerr effect for different materials in Chapter 3. Afterwards, the basics of optical coatings and their design principles are presented in Chapter 4. With these theoretical foundations established, the concepts for an optical switch and frequency tripling mirrors are discussed in Chapters 5 and 6. Next, chapter 7 details the methods used for manufacturing the optical coatings, and Chapter 8 specifically details the adaptations made for the integration of highly nonlinear materials. To validate the theoretical predictions, the experimental setups introduced in 9 are applied to characterize the produced materials and components. The results of these experiments are then presented and discussed in 10. Chapter 11 concludes the work of this thesis and provides an outlook into the potential next steps in the applications of nonlinear optics in thin film interference coatings.

2 Nonlinear optics

When electromagnetic radiation interacts with a material, two cases can be distinguished. At weak intensity levels of radiation, the properties of the material stay constant, and the interaction is called linear with regard to the incident field. When higher intensity levels are considered, the electric field of the incident radiation changes the electronic structure of the material, which in turn influences the interaction between light and material. The interaction becomes nonlinear in nature.

The overview of third-order effects presented here is limited to the part of nonlinear optics necessary for the understanding of this work and is derived from [16] and [17]. Nonlinear optics has been a field of research for several decades, and a multitude of different interactions with different materials has been explored. Typically, the interactions are classified by their degree of dependence on the incident electric field. In the most basic case of linear interaction, the polarization \mathbf{P} in the optical medium is linearly related to the incident electric field \mathbf{E} :

$$\mathbf{P}(t) = \varepsilon_0 \chi^{(1)} \mathbf{E}(t) \quad (2.1)$$

In this Equation, ε_0 is the dielectric constant, and $\chi^{(1)}$ is called linear susceptibility. In the more general case of linear and nonlinear interactions, this equation changes. Due to the tensor-like nature of the susceptibility for higher orders of interaction, index notation is used:

$$P_i(t) = \varepsilon_0 \left(\sum_j (\chi_{ij}^{(1)} E_j(t)) + \sum_{j,k} (\chi_{ijk}^{(2)} E_j(t) E_k(t)) + \sum_{j,k,l} (\chi_{ijkl}^{(3)} E_j(t) E_k(t) E_l(t)) + \dots \right) \quad (2.2)$$

Here, again the polarization induced in the material is described by P_i . This polarization is then broken down into different terms resulting from the different orders of interaction. The second- and third-order terms are resulting from $\chi^{(2)}$ and $\chi^{(3)}$, respectively. Although higher orders of interaction exist, due to their weaker nature, those will not be considered here.

2.1 Third-order effects in isotropic materials

Equation 2.2 contains the relevant terms for calculating the polarization induced into any medium for interaction with an intense electric field. The nonlinear effects produced by each interaction strongly depend on the structure of the involved medium. Effects with even-numbered orders, in this case, specifically the second order, only appear in media without symmetry to inversion and, therefore, not in centrosymmetric crystals and isotropic materials. Thin film materials produced by standard coating processes are ideally amorphous in structure, and second-order nonlinear effects can therefore be neglected in most cases. The remaining terms are the linear part, with the first-order interactions, and the nonlinear part, which only consists of the third-order term:

$$P_i^{(3)}(t) = \sum_{j,k,l} (\chi_{ijkl}^{(3)} E_j(t) E_k(t) E_l(t)) \quad (2.3)$$

This term contains all third-order nonlinear effects that could occur. In the applications considered in this thesis, isotropic media interact with a linearly polarized electrical field $\mathbf{E}(t)$ with the fundamental frequency ω :

$$\mathbf{E}(t) = \frac{1}{2} [\tilde{\mathbf{E}}(\omega) e^{i\omega t} + c.c.] \quad (2.4)$$

When the linear polarization is chosen to be along the x-axis of the coordinate system, Equation 2.3 can be simplified as follows:

$$\mathbf{P}^{(3)}(t) = \epsilon_0 \chi_{xxxx}^{(3)} \mathbf{E}(t) \mathbf{E}(t) \mathbf{E}(t) \quad (2.5)$$

Substituting the electric field in Equation 2.5 with the field from Equation 2.4, the induced polarization is obtained:

$$\mathbf{P}^{(3)}(t) = \frac{1}{2} [\tilde{\mathbf{P}}^{(3)}(\omega) e^{i\omega t} + c.c.] + \frac{1}{2} [\tilde{\mathbf{P}}^{(3)}(3\omega) e^{i3\omega t} + c.c.] \quad (2.6)$$

The induced polarization can therefore be separated into two principal terms. The polarization included in first term, designated as $\tilde{\mathbf{P}}^{(3)}(\omega)$ in Equation 2.6, possesses the frequency ω of the fundamental wave:

$$\tilde{\mathbf{P}}^{(3)}(\omega) = \frac{3}{4} \chi^{(3)}(\omega : \omega, \omega, -\omega) \tilde{\mathbf{E}}(\omega) \tilde{\mathbf{E}}(\omega) \tilde{\mathbf{E}}^*(\omega) \quad (2.7)$$

The second term of Equation 2.6 contains a polarization $\tilde{\mathbf{P}}^{(3)}(3\omega)$ with the frequency of 3ω :

$$\tilde{\mathbf{P}}^{(3)}(3\omega) = \frac{1}{4}\chi^{(3)}(3\omega : \omega, \omega, \omega)\tilde{\mathbf{E}}(\omega)\tilde{\mathbf{E}}(\omega)\tilde{\mathbf{E}}(\omega) \quad (2.8)$$

These two different polarizations generated in the interaction between isotropic media and linearly polarized radiation are responsible for the nonlinear optical effects discussed in this thesis. They will be investigated in more detail in the following sections.

2.2 The optical Kerr effect

The first polarization term derived in the previous section and listed in Equation 2.7 is responsible for the so-called optical Kerr effect. Kerr effects, in general, describe a change in the index of refraction of optical materials when interacting with electric fields. The optical Kerr effect, in particular, describes a change in refractive index induced by nonlinear interaction with an electromagnetic wave. To achieve a better understanding of the induced change in refractive index, Equation 2.2 can, in combination with 2.7, be rewritten as follows:

$$\tilde{\mathbf{P}}(t) = \epsilon_0\chi^{(1)}\tilde{\mathbf{E}}(\omega) + \epsilon_0\frac{3}{4}\chi^{(3)}(\omega : \omega, \omega, -\omega)\tilde{\mathbf{E}}(\omega)\tilde{\mathbf{E}}(\omega)\tilde{\mathbf{E}}^*(\omega) \quad (2.9)$$

$$= \epsilon_0\left(\chi^{(1)} + \frac{3}{4}\chi^{(3)}|\tilde{\mathbf{E}}(\omega)|^2\right)\tilde{\mathbf{E}}(\omega) \quad (2.10)$$

$$= \epsilon_0\left(\chi^{(1)} + \frac{3\chi^{(3)}}{2n_0\epsilon_0c}I\right)\tilde{\mathbf{E}}(\omega) \quad (2.11)$$

Where $|\tilde{\mathbf{E}}(\omega)|^2$ was substituted with the intensity of an electromagnetic wave [17]. Here, n_0 represents the material's index of refraction without the influence of nonlinear effects, and c represents the speed of light in a vacuum:

$$I = \frac{1}{2}n_0\epsilon_0c|\tilde{E}(\omega)|^2 \quad (2.12)$$

Equation 2.11 is in a form where the effective nonlinear coefficient χ can be derived. χ is split into two terms, the linear component $\chi^{(1)}$ and the component $\Delta\chi$ resulting from the nonlinear interaction:

$$\chi = \chi^{(1)} + \Delta\chi = \chi^{(1)} + \frac{3\chi^{(3)}}{2n_0\epsilon_0c}I \quad (2.13)$$

2 Nonlinear optics

Furthermore, the following relation is valid for optical materials [18]:

$$1 + \chi = n^2 \quad (2.14)$$

If the refractive index is separated, similarly to the susceptibility, in the constant part n_0 and a variable part Δn caused by nonlinear interactions, Equation 2.14 can be rewritten:

$$1 + \chi = \chi^{(1)} + \Delta\chi = n_0^2 + 2n_0\Delta n = n^2 \quad (2.15)$$

$$\Rightarrow n_0^2 = 1 + \chi^{(1)} \quad (2.16)$$

$$\Rightarrow \Delta n = \frac{\Delta\chi}{2n_0} \quad (2.17)$$

It is assumed here, that the nonlinear interaction is small compared to the linear interactions ($\Delta n \ll n_0$) and that, therefore:

$$n^2 = n_0^2 + 2n_0\Delta n + (\Delta n)^2 \approx n_0^2 + 2n_0\Delta n \quad (2.18)$$

Equations 2.13 and 2.17 can be combined, to define the nonlinear refractive index n_2 :

$$\Delta n = \frac{1}{2n_0} \frac{3\chi^{(3)}}{2n_0\epsilon_0 c} I = \frac{3\chi^{(3)}}{4n_0^2\epsilon_0 c} I =: n_2 I \quad (2.19)$$

$$\Rightarrow n_2 = \frac{3\chi^{(3)}}{4n_0^2\epsilon_0 c} \quad (2.20)$$

The resulting index of refraction n for optical materials under influence of the optical Kerr effect, therefore, is as follows:

$$n = n_0 + n_2 I \quad (2.21)$$

As can be seen from Equation 2.21, the final refractive index has two principal components: A constant component n_0 and a variable part $n_2 I$. The magnitude of the variable part is proportional to the intensity of the electromagnetic wave causing the nonlinear interaction, as well as to a so-called nonlinear refractive index n_2 . This nonlinear refractive index is directly related to the nonlinear susceptibility of the material and therefore can be treated as a material parameter.

2.3 Third harmonic generation

The second term derived in Equation 2.8 contains a polarization at the frequency 3ω . Therefore, the nonlinear interaction between the material and an electromagnetic wave with frequency ω creates a new electromagnetic wave at the third harmonic of the fundamental frequency. The corresponding process is called **Third Harmonic Generation (THG)** [16].

The efficiency of the conversion process can be calculated by assuming a medium with length l , which interacts with an electromagnetic wave with frequency ω and intensity I_0 , as presented schematically in Figure 2.1 and investigating the evolution of the electric fields at both frequencies [19]. When the efficiencies for the generation of the third harmonic stay relatively low (below approximately 30%), the depletion of the fundamental wave and back conversion from the third harmonic to the fundamental can be neglected. The intensity of the generated third harmonic wave at

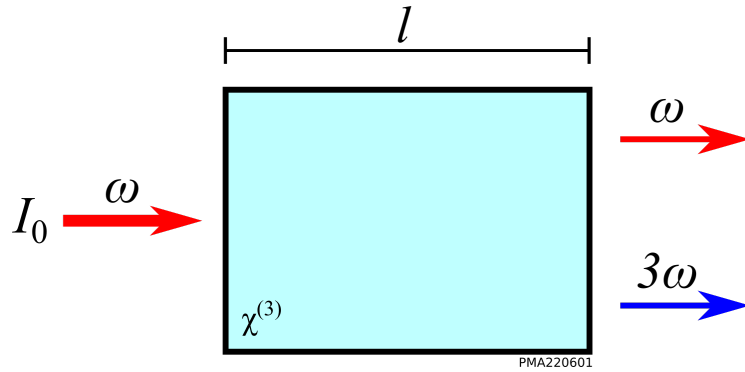


Figure 2.1: A schematic representation of the third harmonic generation in a medium with length l , an incident wave with intensity I_0 , and frequency ω .

the end of the conversion medium then results to:

$$I(3\omega, l) = \left(\frac{3\omega\chi^{(3)}(3\omega)}{4n_1n_3c_0^2\epsilon_0} \right)^2 l^2 I^3(\omega) \text{sinc}^2 \left(\frac{\Delta k l}{2} \right) \quad (2.22)$$

Here, n_1 is the the material's index of refraction at the fundamental frequency, n_3 the index at the third harmonic's frequency, and Δk refers to the phase mismatch of the participating photons:

$$\Delta k = k(3\omega) - 3k(\omega) \quad (2.23)$$

The efficiency of the conversion process is calculated by dividing the intensity of the generated third harmonic by the intensity of the fundamental wave:

$$\eta = \frac{I(3\omega, l)}{I(\omega)} = \left(\frac{3\omega\chi^{(3)}(3\omega)}{4n_1n_3c_0^2\epsilon_0} \right)^2 l^2 I^2(\omega) \text{sinc}^2 \left(\frac{\Delta k l}{2} \right) \quad (2.24)$$

2.3.1 Phase matching

To achieve an efficient conversion process, so-called phase matching is necessary. Phase matching ensures that photons of the third harmonic generated in the conversion medium will be in phase with previously generated photons, which leads to constructive interference. If phase matching is not achieved (e.g., $\Delta k \neq 0$), the conversion process will oscillate between generation and depletion of third harmonic photons over the length of the conversion medium, as the interference oscillates between constructive and destructive. This oscillating behavior is illustrated in Figure 2.2 for different phase mismatches.

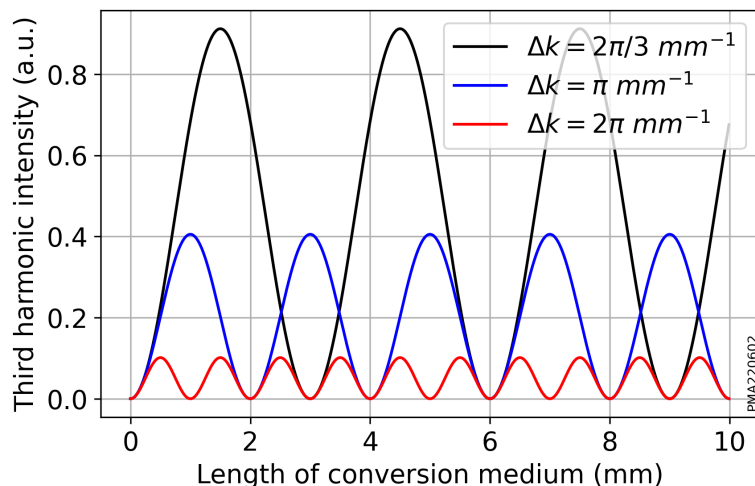


Figure 2.2: Phase mismatch between fundamental and third harmonic waves causes the generated third harmonic to oscillate between constructive and destructive interference. Higher phase mismatches Δk lead to faster oscillations with smaller amplitude.

Depending on the phase mismatch, the maximum intensity and period of the oscillation vary, with smaller mismatches resulting in higher peak intensities and slower oscillation. The period length in a medium, at which the maximum intensity of the generated harmonic is achieved, is called the coherence length l_c . This length

is equal to the section of the medium, where the phase change in the generated harmonic is smaller than 180° or π . It can be calculated from the phase mismatch:

$$l_c = \frac{\pi}{\Delta k} = \frac{\pi}{3 \frac{2\pi}{n_\omega \lambda_\omega} - \frac{3 \cdot 2\pi}{n_{3\omega} \lambda_\omega}} = \frac{\lambda}{6} \left(\frac{1}{n_\omega} - \frac{1}{n_{3\omega}} \right)^{-1} \quad (2.25)$$

This equation illustrates that the difference in the refractive indices between the fundamental n_ω and the third harmonic $n_{3\omega}$ needs to be small for an efficient conversion process, which is achieved with long coherence lengths l_c . Consequently, phase matching is typically achieved by ensuring an identical index of refraction for the fundamental wave and its third harmonic. Due to the naturally occurring spectral dispersion of the refractive index, however, this is problematic for the THG. Figure 2.3 gives an example of the significant difference in the refractive index resulting from this natural dispersion for a typical coating material and application wavelength of third harmonic conversion processes. The coherence length for this dispersion curve and the selected fundamental wavelength is equal to $2.57 \mu\text{m}$.

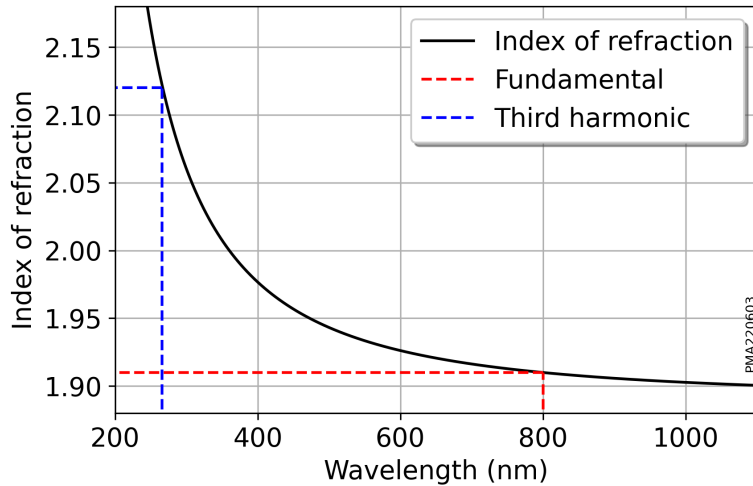


Figure 2.3: The black curve presents the wavelength dispersion of the index of refraction for an exemplary material, in this case HfO_2 . The red and blue curves showcase the resulting difference in refractive index for a fundamental wavelength of 800 nm and its third harmonic at 267 nm. The coherence length for this dispersion curves and the selected fundamental wavelength is equal to $2.57 \mu\text{m}$.

In many frequency conversion processes, especially for the generation of the second harmonic, this difference is usually compensated by taking advantage of birefringent conversion media. By using different polarization for the fundamental and the higher harmonics, two different dispersion curves determine the refractive indices. Figure 2.4 presents a typical case of phase matching for the second harmonic generation of a laser at 1064 nm in a biaxial LBO-crystal.

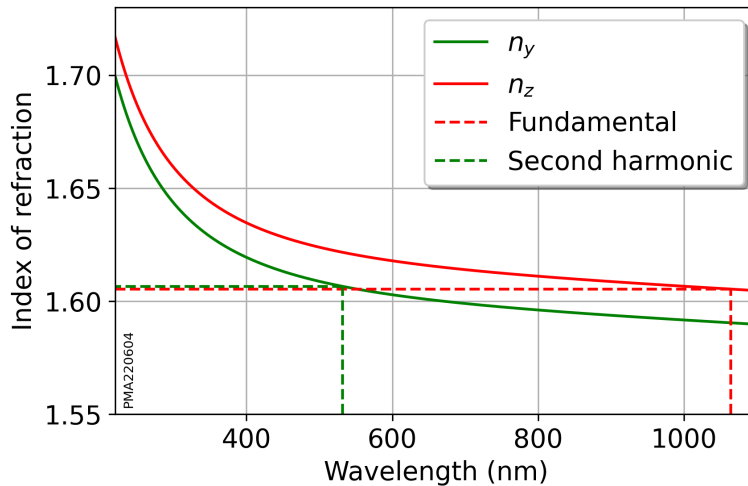


Figure 2.4: Two dispersion curves for different optical axes in an LBO-crystal. By aligning the propagation axis of the fundamental wave with the x-axis of the crystal and utilizing different polarizations, phase matching can be achieved. Data from [20].

By irradiation with a fundamental wave polarized along the z-axis and propagating along the x-axis, an almost perfectly phase matched second harmonic polarized along the y-axis can be generated. Because both waves propagate along the same axis, this variant of phase matching is called non-critical. Usually, the different temperature coefficients of the ordinary and extraordinary indices are exploited to achieve non-critical phase matching for the desired application wavelength. The conversion medium is then stabilized at a temperature where the two refractive indices are equal.

There are many other ways to achieve phase matching in more complicated situations. An often used approach is phase matching by angle tuning, where the angles between fundamental and harmonic wave in relation to the optical axis of the conversion crystal is used to achieve phase matching [16]. A strategy of particular importance for this work is the so called **Quasi-Phase-Matching** (QPM) [21]. When QPM is applied, the normally homogeneous conversion medium is changed to a crystalline medium with periodic changes of the grid orientation along the optical propagation axis. This kind of conversion crystal is then called 'periodically poled'. A schematic illustration of a periodically poled conversion medium is given in Figure 2.5. With this conversion approach, true phase matching is not achieved. Instead, the phase of the generated third harmonic changes at each interface in the medium due to the change in crystal orientation. When the length of the single sections is chosen so that it is equal to a multiple of the coherence length defined in Equation 2.25, the generated harmonics in each section can add up.

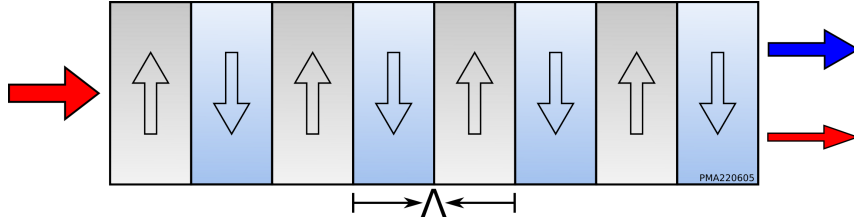


Figure 2.5: A schematic illustration of a periodically poled conversion medium. The orientation changes with the period $\Lambda/2$.

To achieve the optimum case of quasi phase matching, the period Λ of the crystal has to be equal to two times the coherence length [21]:

$$\Lambda = 2l_c = \frac{2\pi}{\Delta k} \quad (2.26)$$

With this periodic phase change of the generated harmonic, true phase matching is unnecessary, as illustrated in Figure 2.6. However, the conversion efficiency is still reduced compared to true phase matching. This can often be compensated in practical applications since the alignment and, therefore, the effective nonlinear coefficients of the crystals used for the conversion process can be chosen more freely.

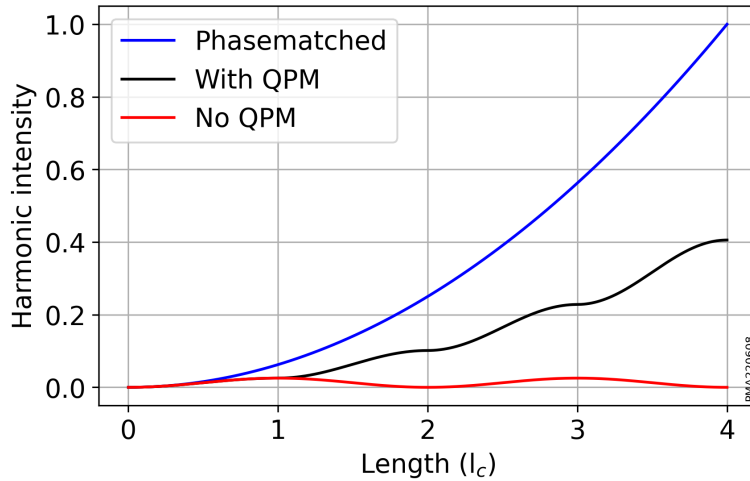


Figure 2.6: The intensity development for different phase matching approaches. The blue curve shows the case for ideal phase matching e.g. $\Delta k = 0$. The black curve shows the highest intensity achievable with QPM, and the red curve represents the same case for no phase matching.

In classical QPM, the sign of the nonlinear susceptibility is inverted with the periodic poling. However, a so-called on-off modulation is also possible, where the conversion material is made up of 'active' sections, which generate the harmonic

and 'inactive' sections, where only the phase mismatch is compensated [21]. The intensity of the generated harmonic achievable obtained with optimal QPM and the 'on/off'-modulation is compared in Figure 2.7. This approach leads to a further reduction in conversion efficiency, but also offers additional flexibility with regard to the selection of the conversion materials. For instance, a version of this approach can be applied to amorphous materials, such as the materials used in optical coatings. By combining one material with a high nonlinear susceptibility with one that features a low susceptibility in layers with the optical thickness of a coherence length, effective conversion can be achieved. This is the fundamental principle of the **F**requency **T**ripling **M**irrors (FTMs) discussed in this thesis. By exploiting the interference and intensity enhancement of thin film coatings, the efficiencies of FTMs can greatly exceed those of simple QPM approaches. They are discussed in more detail in Chapter 6.

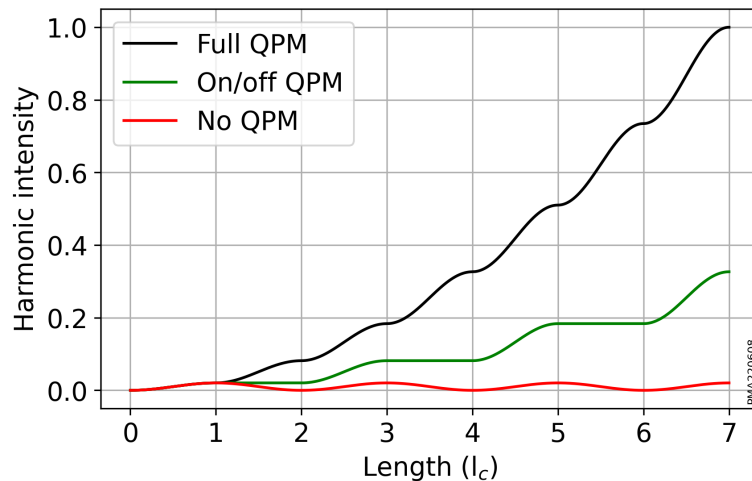


Figure 2.7: The intensity development for different approaches of QPM. The black curve shows the highest intensity achievable with ideal QPM e.g. a sign inversion of the nonlinear susceptibility after a thickness equal to l_c . The green curve shows the intensity obtained, when the nonlinear susceptibility is equal to zero in every second section of the conversion medium ('on/off'-modulation). The red curve shows the same case for no phase matching.

2.4 Free-electron effects

The nonlinear optical effects in solid-state materials described in the earlier section are all based on small disturbances of the atomic potential of the electrons caused by intense electric fields. These disturbances create the nonlinear components in the interaction between ions and electrons, which are responsible for the nonlinear

optical effects. Although the potential for the interactions of the bound electrons in a material is disturbed in this case, the electrons are in this model still bound by it. When solid-state, transparent dielectrics are considered, the electrons, therefore, stay in the valence band, and the incident photons do not possess enough energy to allow an excitation to the conduction band.

At very high intensities of laser radiation, this assumption is no longer valid. Several mechanisms contribute to the excitation of electrons from valence to the conduction band, when high intensities of laser radiation are present. This causes different optical effects, for example, increased absorption [22], a changed index of refraction [23], and in extreme cases, the destruction of the dielectric medium [24]. Because of this, much research has already been conducted about the total electron density in dielectric solid-state materials and how to theoretically model it [25, 26, 27]. A formalism to describe the temporal evolution of the total electron density ρ in the conduction band is summarized in [28]:

$$\frac{\partial \rho}{\partial t} = W_{\text{PI}}(I, t) + W_{\text{av}}(\rho, t) - W_{\text{rel}}(\rho, t) \quad (2.27)$$

The different terms here represent the different mechanisms of ionization and relaxation: W_{PI} represents the photoionization, which can be further divided into tunnel- and multiphoton ionization, and W_{av} represents the avalanche ionization. The last term represents the relaxation of electrons from the conduction band back to the valence band. The different mechanisms are explained in more detail in the following section.

2.4.1 Photoionization

The direct ionization from the valence to the conduction band, which is caused by the intensity I of incident radiation, is described by the photoionization term $W_{\text{PI}}(I, t)$. This term can be further broken down into two contributing mechanisms; the multiphoton and tunnel ionization. Both mechanisms fundamentally describe the same process, the ionization of electrons caused by several photons with individual energy smaller than the total energy required for ionization. In the case of multiphoton ionization, multiple photons interact with an electron simultaneously and transfer their energy. If the accumulated energy becomes larger than the band gap energy required for ionization, the electron is excited to the conduction band. This process is illustrated in Figure 2.8 (a). Due to the frequency-dependent energy of photons, this process is strongly related to the wavelength of the electric field

[29]. When the intensity of the electric field is further increased, the shape of the electronic potential starts to deform, and the probability for electrons to tunnel out of their bonding potential increases. Since the tunnel ionization is caused by the electric field, its dependence on the wavelength of the electric field is weak. The process is illustrated in Figure 2.8 (b). Both processes can happen simultaneously when the energy of multiple absorbed photons is not high enough to overcome the potential barrier, but the potential is also not deformed enough to allow tunneling from the ground state. When both processes happen in parallel, the energy from the absorbed photons lifts the energy state sufficiently to allow tunneling through only slightly deformed potential barriers. The rates of both the multiphoton ionization and the tunnel ionization can be modeled with an approach based on the Keldysh-theory of ionization in strong electromagnetic fields [25].

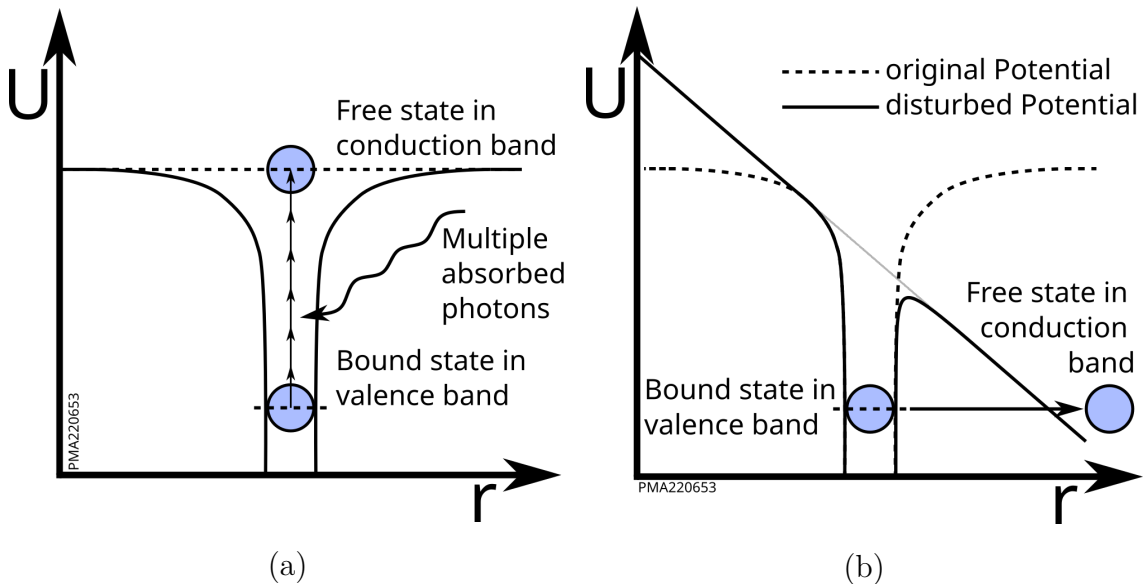


Figure 2.8: The different mechanism of photoionization. (a) depicts the multiphoton ionization, where several photons transfer their energy simultaneously to a single electron. (b) illustrates the tunnel ionization, where the electronic potential is disturbed by the electric field of the incident radiation. Due to the deformed potential, electrons can tunnel out of their bounding potential.

2.4.2 Avalanche ionization

After the photoionization has caused an initial amount of free carriers in the conduction band, another mechanism can contribute to further increasing the density of free carriers. This mechanism is known as impact or avalanche ionization and will be explained in this section. In avalanche ionization, free carriers in the conduction band interact with the electric field of the incident radiation and gain kinetic energy

by inverse Bremsstrahlung absorption [23]. When the energy of a free carrier is increased above a certain critical energy E_{crit} , it can create more free carriers by energy transfer via collision. The process is depicted schematically in Figure 2.9. The modeling of avalanche ionization goes beyond the scope of this work, the different approaches for modeling can be found in [30, 31, 27].

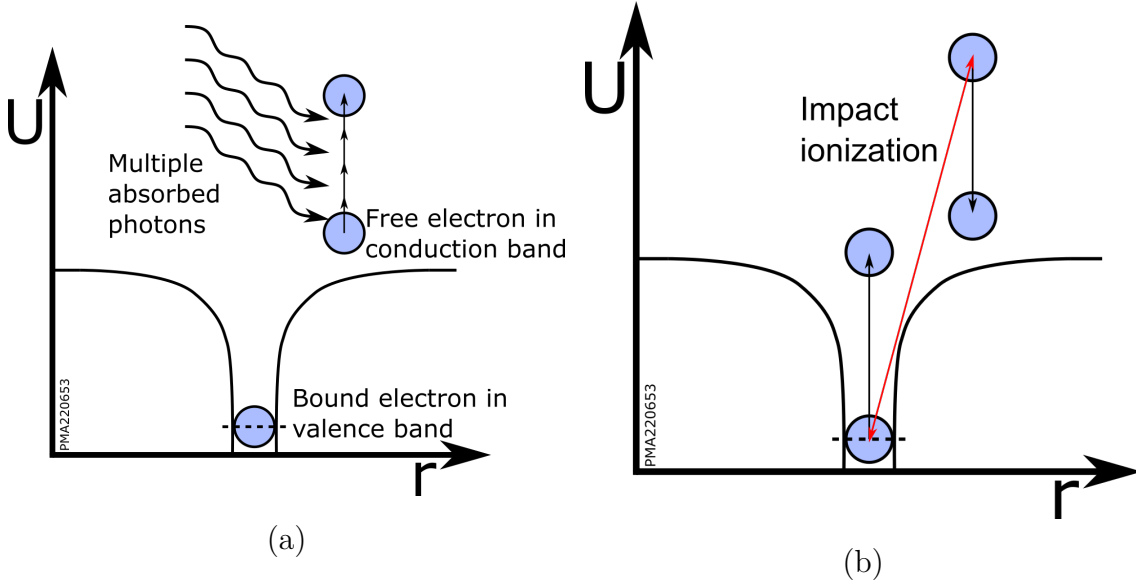


Figure 2.9: A schematic depiction of avalanche ionization. The ionization happens in two steps. (a) an already ionized electron absorbs energy from the incident electric field and is further energized in the conduction band. Then, it can collide with a bound electron in its ground state and subsequently transfers its energy (b), ionizing the bound electron in turn.

2.4.3 Relaxation

The final mechanism influencing the electron densities in dielectrics is the relaxation of excited electrons. The relaxation of electrons can result from different processes in solid-state materials. Especially in amorphous coating materials, many states near the materials' band gap contribute to the relaxation of electrons. The resulting relaxation processes with time constants in the order of ultrashort laser pulse durations can be summarized in the following equation:

$$\frac{\partial \rho(t)}{\partial t} = -\frac{\rho(t)}{\tau_{\text{rel}}} \quad (2.28)$$

Here, τ_{Rel} is the lifetime of free carriers. These lifetimes were measured in several experiments for different coating materials (TiO_2 , Ta_2O_5 , HfO_2 , Al_2O_3 and SiO_2), and determined to be in the range of 220 fs to 1100 fs [32].

2.4.4 Influence of free electrons

The free carriers generated by the mechanisms introduced in the previous sections are the root cause of various physical effects that cannot be neglected when nonlinear optical effects in thin film coatings are investigated. The central effects considered in this work are laser-induced damage, nonlinear absorption, and a changed refractive index.

laser-induced damage has different mechanisms depending on the duration of the incident laser pulses. For continuous wave irradiation, the damage is thermally induced and mainly determined by heat-related properties, such as conductivity and melting point of the samples under test. When the pulse duration is decreased into the nanosecond range, this changes and the damage mechanisms can vary between heat-based damage caused by absorption in the sample and intensity-based effects. In practice, however, defects on optical surfaces act as absorption seeds and start a thermal damage process in this regime [28].

When the pulse duration is reduced further to approximately 10 ps and shorter, purely intensity-based effects dominate. The intensity of the laser pulse creates, via the mechanisms introduced in the previous sections, free carriers. When the carrier density reaches a critical value (about $1 \times 10^{21}/\text{cm}^3$, the internal electronic structure of the dielectric material is disturbed too much, and the material is destroyed. The destruction itself is the product of different subsequent processes on different time scales that result from the high density of free electrons [33]. In practice, the LIDT F_{th} of an optical material in the ultrashort pulse regime mostly depends on its band gap energy E_{gap} and the actual pulse duration τ_p of the incident pulses:

$$F_{\text{th}} = (c_1 + c_2 E_{\text{gap}}) \tau_p^\kappa \quad (2.29)$$

With $c_1 = -0.16 \pm 0.02 \text{ Jcm}^{-2}\text{fs}^{-\kappa}$, $c_2 = 0.074 \pm 0.004 \text{ Jcm}^{-2}\text{fs}^{-\kappa}\text{eV}^{-1}$ and $\kappa = 0.30 \pm 0.03$ being material and pulse duration independent parameters [24].

For applications at high intensity, achieving low absorption in the utilized optical components and materials is of critical importance to achieving good optical performance. The free electrons generated by highly intense ultrashort pulsed lasers can, however, add another loss mechanism, the nonlinear absorption. Nonlinear absorption is a direct result of the multiphoton ionization introduced in Section 2.4.1. The underlying ionization by coincident photons strongly depends on the intensity,

which in turn causes an intensity-dependent absorption. For the mostly dominant two-photon absorption process, the intensity $I(z)$ in an optical medium results to:

$$I(z) = \frac{I_0}{1 + \beta I_0 \cdot z} \quad (2.30)$$

Here, I_0 is the initial intensity that enters the medium, and β is the so-called two-photon absorption coefficient, which is a material parameter. Typical values for the coefficient depend on the material and conditions of the light-matter interaction. For indium tin oxide, a material with very high optical nonlinearity, β can range from -3 cm/GW down to almost -8000 cm/GW , depending on the wavelength of the incident radiation [34].

The final process considered in this thesis is the change in the refractive index caused by the free electrons. Mero *et al.* demonstrated, that high-intensity laser radiation can alter the dielectric function of the material under irradiation [35]. The effects observed for optical coating material show a reduction of the real part and an increase of the imaginary part of the materials' dielectric functions. In practice, this effect, therefore, results in a reduced index of refraction and increased losses during the irradiation with intense laser pulses.

3 Nonlinear refractive index of optical materials

The optical components, which are the topic of this thesis, rely on nonlinear optical effects in their constituent coating materials. Materials for thin film coatings are typically almost perfectly amorphous and, therefore, isotropic in nature [36]. This isotropic nature fundamentally excludes all nonlinear effects of even order. Effectively, this reduces the nonlinear optical effects occurring in thin film coating to the third order, as discussed in more detail in Section 2.1.

3.1 Dielectric materials

The dielectric material typically chosen for dielectric coatings consists of SiO_2 , which is the most prevalent low-index material, and a range of high-index materials such as HfO_2 , Ta_2O_5 , Nb_2O_5 and TiO_2 . The material Al_2O_3 is also applied frequently but can be used, depending on the second material, either as high-index material when combined with SiO_2 or as low-index material in combination with other materials. Other materials are available for more exotic spectral ranges, such as fluoride salts that are most frequently applied in coatings for the ultraviolet spectral range, or amorphous semiconductor materials, which are suited for optics in the far-infrared range. In the visible and near-infrared range, oxides are most widespread. Since these high- and low-index materials are combined in coating stacks, it is advantageous for the integration of nonlinear effects, when these materials already show a significant optical nonlinearity. The nonlinear refractive indices for the most commonly used oxidic coating materials are listed in Table 3.1.

For SiO_2 and Al_2O_3 , literature values are available, and their nonlinear refractive indices are very similar. The high-index materials show more variability and, in general, exhibit a stronger nonlinear refractive index, but the values are still relatively low, and high intensities are required for significant changes in the overall refractive index of a material.

3.2 Epsilon-Near-Zero materials

The first group of highly nonlinear materials discussed in this section are the so-called **Epsilon-Near-Zero-materials** (ENZ-materials). These materials are distinguished by their zero-permittivity wavelength, for which the real part of the permittivity vanishes. Based on this, a high field enhancement and strongly increased conversion efficiency for nonlinear processes was predicted around this wavelength [48, 49]. The material class has been under investigation for approximately ten years due to their special characteristics [50, 51, 52]. The origins of this strong nonlinearity are discussed in [49], so only a brief overview will be given here. As discussed in Section 2.2, the total change of the refractive index $\Delta n = n_2 I$ usually scales linearly with the nonlinear refractive index n_2 and the intensity I . Therefore, to increase this change at a given intensity, a material with larger n_2 has to be found. Usually, n_2 is defined as follows:

$$n_2 = \frac{3\chi^{(3)}}{4n_0 \operatorname{Re}(n_0)\epsilon_0 c} \quad (3.1)$$

This is equal to the definition in Equation 2.20, when the refractive index is a real number, e.g. the material is free of absorption. In the derivation of this relation, it is, however, assumed that $\delta n = n_2 I \ll n$, which is not necessarily true for the highly nonlinear ENZ-materials. It is, therefore, advantageous to calculate an intensity-depended refractive index directly from the nonlinear susceptibility:

$$n(I) = \sqrt{\epsilon(E)} = \sqrt{\epsilon^{(1)} + 3\chi^{(3)}|E|^2} \quad (3.2)$$

Table 3.1: The linear and nonlinear refractive indices for the most common oxidic coating materials. The nonlinear refractive index increases with the linear one.

Material	n_0	$n_2 \cdot 10 \times 10^{-16} \text{ cm}^2/\text{W}$	wavelength (nm)
SiO ₂	1.9 – 3 [37]	1.4707 [38]	1064
Al ₂ O ₃	1.6655 [39]	3.1 [40, 41, 42]	1064
HfO ₂	1.9564 [43]	5.8 [44]	1550
Ta ₂ O ₅	2.0957 [45]	72.3 [46]	800
TiO ₂	2.3078 [47]	94.3 [40]	1064

For comparison with other materials, the nonlinear refractive index n_2 is redefined to be the initial slope of the curve $n(I)$, where the total index change Δn is still small:

$$n_2 = \left. \frac{dn}{dI} \right|_{I=0} \quad (3.3)$$

The strong nonlinear behavior of ENZ-materials, however, can not be explained by the third-order susceptibility alone. Although the nonlinearity increases around the near-zero wavelength, the increase is only by about a factor of four, which is not sufficient to account for the factor of 100 that nonlinear effects are amplified in ENZ-materials [49]. It was therefore concluded, that instead of a large $\chi^{(3)}$, ENZ-materials feature a combination of excitation of free electrons with a strong internal enhancement of the external electric field $|E|$.

3.2.1 Excitation of free electrons

ENZ-materials such as noble metals or highly doped semiconductors can be described by the Drude-model[53]. The dispersion of the permittivity is then given by:

$$\epsilon(\omega) = \epsilon_\infty - \frac{\omega_P^2}{\omega^2 + i\gamma\omega} \quad (3.4)$$

Here, ϵ_∞ is the high-frequency permittivity, γ the electron damping, and ω_P the plasma frequency. The plasma frequency can be calculated by

$$\omega_P = \sqrt{\frac{Ne^2}{m_e^* \epsilon_0}}. \quad (3.5)$$

N represents the density of free electrons, e is the elemental charge, and m_e^* is the effective mass of electrons. Different mechanisms during irradiation allow the modification of the plasma frequency: For photon energies larger than the band gap (or intraband transition energy in the case of metals) of the considered materials, irradiation directly increases the electron density in the conduction band, which increases the plasma frequency. For photons with energies smaller than the materials' band gap, the distribution of the electrons in the conduction band is changed by electron heating. When the conduction band deviates from a parabolic shape, this will increase the effective mass of the electron and therefore shift the plasma frequency to longer wavelengths. When the frequency of the incident radiation is equal to the plasma frequency, the interaction is resonant [34, 54]. The second case

of low-energy photons is especially relevant for highly doped semiconductors such as **I**ndium **T**in **O**xide (ITO) and **A**luminum **Z**inc **O**xide (AZO). Their, compared to metals small, density of free electrons results in a smaller heat capacity of the electrons and, therefore, larger changes in their temperature for the same incident energy. Secondly, they feature a non-parabolic conduction band [34, 55], which causes a strong dependency on the effective mass and, consequently, the plasma frequency on the electron temperature. When the plasma frequency is changed by either of the two mechanisms, it directly influences the relation in Equation 3.4, and changes the permittivity and, in effect, the refractive index of the material under consideration.

3.2.2 Enhancement of the electric field

The enhancement of the electric field in ENZ-materials is based on different mechanisms. The first directly results from the continuity of the normal component of the electric field at interfaces. In general, when surface charges are neglected, the perpendicular and parallel components of the electric field at an interface between two media is related by:

$$E_1^{\parallel} = E_2^{\parallel} \quad (3.6)$$

$$\epsilon_1 E_1^{\perp} = \epsilon_2 E_2^{\perp} \quad (3.7)$$

Here, E_1 and E_2 are the electric fields in the first medium, and second medium, respectively. When an electric field E interacts with an ENZ-material featuring the permittivity ϵ_{ENZ} under an angle of incidence θ , the absolute value of $|E_{\text{ENZ}}|$ the resulting electric field in the ENZ-materials can be calculated as follows:

$$|E_{\text{ENZ}}| = |E_0| \sqrt{\cos^2 \theta + \frac{\epsilon_1 \sin^2 \theta}{\epsilon_{\text{ENZ}}}} \quad (3.8)$$

Due to the nearly zero permittivity ϵ_{ENZ} , the second term in this equation becomes very large. At high angles of incidence, the total field in the ENZ-material can be strongly enhanced due to the continuity of its perpendicular component. The second mechanism is based on the formation of special propagation modes in very thin films of ENZ-materials [49]. In combination with the enhancement effects resulting from the interface to different materials, this special ENZ-mode features a high field enhancement [56]. This mode is confined to really thin layers of less than $\lambda/50$, and degrades at layers thicker than this. Another mechanism that is suspected to take

part in the field enhancement is the vanishing group velocity in ENZ-materials. In a lossless ENZ-medium, the group velocity is given by [57]:

$$v_g = \sqrt{\epsilon_{\text{ENZ}}}c \quad (3.9)$$

With c being the speed of light. The group velocity in ENZ-materials can asymptotically vanish at their ENZ-wavelengths, which would cause a slow-light phenomenon [58]. Slow light is often associated with enhancement of the electric field [59] and therefore suspected to also contribute to the enhancement in ENZ-materials[56], but more research is necessary to confirm this.

3.3 Semiconductors

The second material class that is promising as active nonlinear optical material in the frame of this work are semiconductors. The dielectric materials typically applied in optical coatings have a band gap energy starting at 3.3 eV for TiO₂, and larger values for other materials, especially for the low index material such as SiO₂, with 8.3 eV [60]. This leads to a transparency of these materials for the complete visible spectral range, limited by TiO₂ at approximately 380 nm and approximately 150 nm for SiO₂. In contrast to that, semiconductor materials used in the optical context feature a much smaller optical band gap energy, ranging from approximately 2.8 eV for zinc selenide over 1.42 eV for gallium arsenide, 1.14 eV for silicon and up to 0.67 eV for germanium [61]. These (and many more) semiconductor materials are frequently used in optical applications, especially infrared spectral range, due to their high transparency in this region and their very high refractive indices [62, 63, 64]. In addition to these beneficial properties, semiconductor materials feature a strong optical nonlinearity. This results from their small optical band gaps and the, therefore, higher likelihood of **Two-Photon-Absorption** (TPA) (see also Section 2.4.1), which creates free carriers and therefore induces localized nonlinearities [65]. Additionally, the field-induced motion of the free carriers creates non-localized changes in the electric field of the material and changes in the optical properties of the material [66].

These effects also influence the nonlinear index of refraction, which is the parameter of most interest for this work. Since the nonlinearities created in semiconductors rely on the TPA as fundamental mechanism, photon energies that are just above half of the band gap energies deliver the strongest nonlinear interaction. In [67], a theoretical prediction for the relation of nonlinear refractive index and photon energy is discussed. The behavior resulting from these calculations is illustrated in

3 Nonlinear refractive index of optical materials

Figure 3.1. Below the TPA-threshold, the n_2 (normalized to the material's bandgap and refractive index n_0) increases, until it reaches a maximum just above a photon energy of $1/2 \cdot E_{\text{Gap}}$. Over this threshold, free carriers take part in the interaction, and the effective n_2 decreases and even becomes negative at high photon energies. For typical optical applications with wavelengths of around $1 \mu\text{m}$, which is equivalent to a photon energy of approximately 1.24 eV , the best fitting of the semiconductors listed above are zinc selenide and gallium arsenide. Unfortunately, little data from literature is available about their nonlinear refractive index around $1 \mu\text{m}$. Relatively well researched is their behavior at the telecommunication wavelengths around $1.55 \mu\text{m}$, where they feature high nonlinear refractive indices of $1590 \times 10^{-16} \text{ W/cm}^2$ for gallium arsenide and $445 \times 10^{-16} \text{ W/cm}^2$ for silicon. Due to the dispersion of n_2 around the TPA-threshold, this value is believed to again increase strongly for applications at $1 \mu\text{m}$, which makes especially gallium arsenide a promising material for the integration of nonlinear optics into thin films.

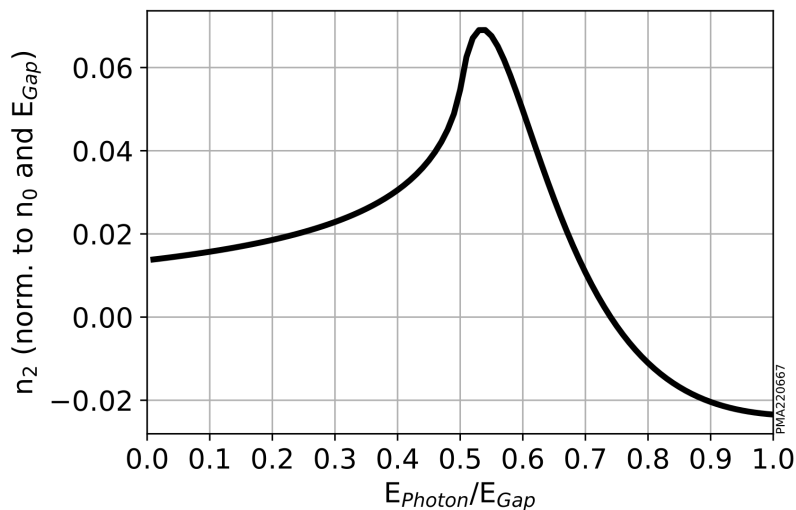


Figure 3.1: The expected dispersion of the nonlinear refractive index n_2 in relation to the photon energy. n_2 was normalized to account for the first order index of refraction n_0 and the bandgap E_{Gap} of different materials. The photon energy E_{Photon} is given in relation to the bandgap of the material. A clear maximum with positive n_2 can be observed just above a relative photon energy of 0.5. Plot reproduced with data from [67].

4 Thin film interference coatings

For efficient use of optical components, functional coatings have been applied since antiquity [9, 10]. While early coatings relied on metals to produce mostly mirrors, interference coatings utilizing dielectric materials were invented in the early 20th century [11, 12]. In this section, a brief overview of the working principles of optical interference coatings is presented with the aim of achieving a theoretical understanding of the concept of Kerr-band-switches.

4.1 Dielectric coatings

Optical interference coatings are based on the reflections and interference caused in stacks of transparent materials. These materials are typically either dielectric materials or, less commonly, semiconductors. As discussed in Section 3.3, dielectric materials are defined by their optical band gap energy, which ideally is much larger than the energy of interacting photons. The larger band gap energy causes dielectric materials to be transparent to radiation. The interaction of an ideal dielectric interference coating is, therefore, mainly determined by refraction, reflection, and transmission at the interfaces of transparent materials. The interaction for a single interface between two transparent materials is illustrated in Figure 4.1. With the refractive indexes n_0 and n_1 , the transmitted (A_t) and reflected (A_r) amplitudes for parallel (\parallel) and perpendicular (\perp) polarizations are described by the Fresnel equations, which are derived in detail in [18].

With these equations, the fundamental behavior of a single interface can be described. A typical curve for the angular reflectance for the different polarizations at an interface with $n_0 = 1$ and $n_1 = 1.5$ is presented in Figure 4.2. The expected increase in reflectance for higher angles of incidence as well as the minimum at the Brewster-angle for p-polarized radiation, can be observed.

Similarly, the Fresnel equations allow the complete modeling of thin film coatings. For a single layer on an optical substrate, the solution can be achieved relatively straightforward as presented in [68]. The modeling of more complex layer systems is based on another approach, which is presented in Section 4.1.1.

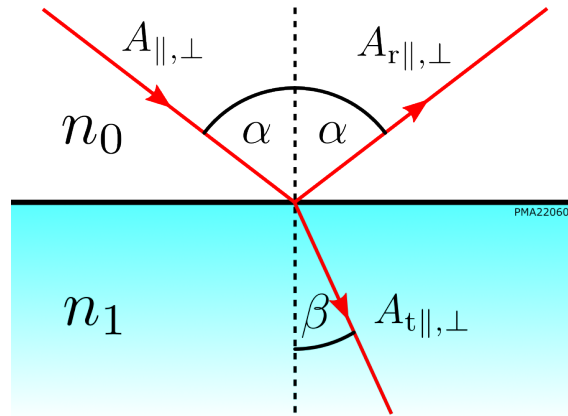


Figure 4.1: Reflection, transmission, and refraction and an interface between two optical media with refractive indices n_0 and n_1 .

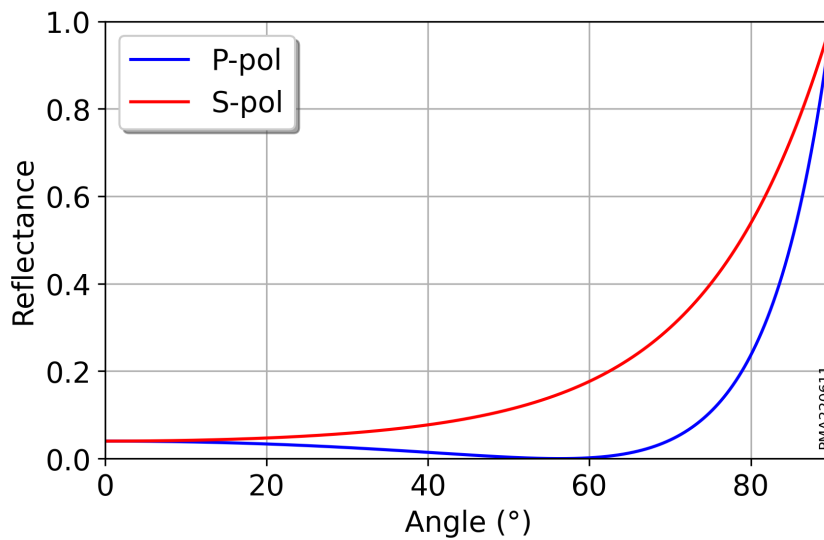


Figure 4.2: The angular reflectance for s- and p-polarized light of an interface with $n_0 = 1$ and $n_1 = 1.5$. An overall increase in reflectance for higher angles of incidence can be observed. The p-polarized radiation exhibits a minimum of reflectance at the Brewster-angle.

4.1.1 Transfer-matrix-formalism

The modeling of a thin film stack with Fresnel's equations alone quickly becomes unpractical when higher layer numbers are considered. A widely used alternative method is the transfer matrix method, which relates the change of the electric field E and the magnetic field H between the two interfaces of a layer with a linear matrix

operation. Here, the formalism introduced in [68] is used. The fields at the $m - 1$ interface can be obtained from the fields at interface m as follows:

$$\begin{pmatrix} E_{m-1} \\ H_{m-1} \end{pmatrix} = \begin{bmatrix} \cos(\delta_m) & \frac{i}{\mu_m} \sin(\delta_m) \\ i\mu_m \sin(\delta_m) & \cos(\delta_m) \end{bmatrix} \begin{pmatrix} E_m \\ H_m \end{pmatrix} := \mathbf{M}_m \begin{pmatrix} E_m \\ H_m \end{pmatrix} \quad (4.1)$$

The effective refractive index μ_m depends on angle of incidence θ_m and polarization of the incoming light:

$$\mu_m = n_m \cos(\theta_m) \text{ for s-pol. and } \mu_m = \frac{n_m}{\cos(\theta_m)} \text{ for p-pol.} \quad (4.2)$$

Consequently, δ_m is the phase difference of the light obtained by propagation through layer m and defined as:

$$\delta_m = \frac{2\pi n_m d_m \cos(\theta_m)}{\lambda}, \quad (4.3)$$

where n_m represents the index of refraction and d_m the physical thickness of layer m . The effect of a complete stack of N layers then results from the product of all layer matrices M_m :

$$\begin{pmatrix} E_0 \\ H_0 \end{pmatrix} = \prod_{m=1}^N \mathbf{M}_m \begin{pmatrix} E_m \\ H_m \end{pmatrix} \quad (4.4)$$

To retrieve reflectance R and transmittance T from the introduced matrix formalism, the product matrix \mathbf{M}_p can be rewritten as:

$$\mathbf{M}_p =: \begin{bmatrix} A & iB \\ iC & D \end{bmatrix} \quad (4.5)$$

With the so-defined matrix elements, the amplitude coefficients R of reflection and T for transmission can be calculated as follows:

$$\mathcal{R} = \frac{\mu_{\text{env}}A - \mu_{\text{sub}}D + i(\mu_{\text{env}}\mu_{\text{sub}}B - C)}{\mu_{\text{env}}A + \mu_{\text{sub}}D + i(\mu_{\text{env}}\mu_{\text{sub}}B + C)} \quad (4.6)$$

$$\mathcal{T} = \frac{2\mu_{\text{env}}}{\mu_{\text{env}}A + \mu_{\text{sub}}D + i(\mu_{\text{env}}\mu_{\text{sub}}B + C)} \quad (4.7)$$

4 Thin film interference coatings

The reflectance and transmittance consequently can be calculated as follows:

$$R = \mathcal{R}\mathcal{R}^* = \frac{(\mu_{\text{env}}A - \mu_{\text{sub}}D)^2 + (\mu_{\text{env}}\mu_{\text{sub}}B - C)^2}{(\mu_{\text{env}}A + \mu_{\text{sub}}D)^2 + (\mu_{\text{env}}\mu_{\text{sub}}B + C)^2} \quad (4.8)$$

$$T = \frac{4\mu_{\text{env}}\mu_{\text{sub}}}{(\mu_{\text{env}}A + \mu_{\text{sub}}D)^2 + (\mu_{\text{env}}\mu_{\text{sub}}B + C)^2} \quad (4.9)$$

The effective index of refraction of the substrate μ_{sub} and the environment μ_{env} are defined analogously to Equation 4.2. For a typical mirror coating, this formalism can be applied to calculate the reflectance at the design wavelength.

For a mirror coating, the layer thickness is chosen in such a way, that the optical thickness of each single layer in the sequence of alternating materials is equal to a quarter of the design wavelength. This type of layer is named QWOT-layer (QWOT standing for **Q**uarter **W**avelength **O**ptical **T**hickness). In this case, the phase difference obtained in each layer, is, per the definition of a QWOT-layer, equal to $\delta_m = \pi/2$. Therefore, the transfer Matrix for any one layer is of the form:

$$\mathbf{M}_m = \begin{bmatrix} \cos(\pi/2) & \frac{i}{\mu_m} \sin(\pi/2) \\ i\mu_m \sin(\pi/2) & \cos(\pi/2) \end{bmatrix} = \begin{bmatrix} 0 & i/\mu_m \\ i\mu_m & 0 \end{bmatrix}. \quad (4.10)$$

For a typical stack of layers, starting with a high-index material with an effective refractive index μ_1 and continuing with pairs of low-index (μ_2) and high-index layers, the matrix of a stack with N pairs results in the following product of $N + 1$ matrices:

$$\mathbf{M}_p = \begin{bmatrix} 0 & i/\mu_1 \\ i\mu_1 & 0 \end{bmatrix} * \begin{bmatrix} 0 & i/\mu_2 \\ i\mu_2 & 0 \end{bmatrix} * \begin{bmatrix} 0 & i/\mu_1 \\ i\mu_1 & 0 \end{bmatrix} * \dots * \begin{bmatrix} 0 & i/\mu_1 \\ i\mu_1 & 0 \end{bmatrix}. \quad (4.11)$$

Multiplying this sequence of matrices results in one Matrix for the $N+1$ layers:

$$\mathbf{M}_p = \begin{bmatrix} 0 & i(-\mu_2/\mu_1)^N/\mu_1 \\ i\mu_1(\mu_2/\mu_1)^N & 0 \end{bmatrix} \quad (4.12)$$

After obtaining the matrix characterizing the layer stack, the reflectance can be calculated by applying Equation 4.8:

$$R = \left(\frac{\mu_1^{2(N+1)} - \mu_{\text{env}}\mu_{\text{sub}}\mu_2^{2N}}{\mu_1^{2(N+1)} + \mu_{\text{env}}\mu_{\text{sub}}\mu_2^{2N}} \right) \quad (4.13)$$

For large N and $\mu_2 < \mu_1$ this can be further simplified to:

$$R = 1 - 4\mu_{\text{env}}\mu_{\text{sub}} \frac{\mu_2^{2N}}{\mu_1^{2(N+1)}} \quad (4.14)$$

With this simple formula, the reflectance of a QWOT-stack mirror can now be calculated easily. For typical conditions for normal incidence, $\mu_{\text{env}} = 1$, $\mu_{\text{sub}} = 1.45$, $\mu_1 = 2.1$, $\mu_2 = 1.45$ and 31 layers, resulting in $N = 15$, the reflectance results in $R = 0.99998 = 99.998\%$.

For the intended applications in utilizing nonlinear effects in thin film coatings, not only reflectance and transmittance are of interest, but also the enhancement of the incident electric field is an essential property of a thin film design. Using the established matrix formalism, the positive and negative propagating electromagnetic fields in layer j at a position z between the interface positions z_j and z_{j+1} of layer j :

$$E_j^+(z) = \frac{\mathcal{T}_{0j} \exp[-2\pi i n_j (z - z_j) \cos(\theta_j)] / \lambda}{1 - \mathcal{R}_{j0} \mathcal{R}_{j,N+1} \exp(-4\pi n_j d_j \cos(\theta_j)) / \lambda}, \text{ and} \quad (4.15)$$

$$E_j^-(z) = \frac{\mathcal{R}_{j,N+1} \mathcal{T}_{0j} \exp[-2\pi i n_j (z - z_{j+1} - d_j) \cos(\theta_j)] / \lambda}{1 - \mathcal{R}_{j0} \mathcal{R}_{j,N+1} \exp(-4\pi n_j d_j \cos(\theta_j)) / \lambda}. \quad (4.16)$$

The relative intensity enhancement $I_s(z)$ for the s-component and $I_p(z)$ for the p-component of the polarization at the same position then results to:

$$I_s(z) = \frac{1}{4} |E_j^+(z) + E_j^-(z)|^2 \quad (4.17)$$

$$I_p(z) = \frac{1}{4} |E_j^+(z) + E_j^-(z)|^2 \cos^2(\theta_j) + |E_j^+(z) - E_j^-(z)|^2 \sin^2(\theta_j) \quad (4.18)$$

The intensity distribution in the layer stack for an exemplary mirror coating consisting of QWOT-layers as specified above, is presented in Figure 4.3. In the last layers (meaning the last layers to be coated, e.g. the first layers to interact with incident radiation), a peak in the internal intensity enhancement can be observed at the last interface. The further the radiation propagates into the layer stack, the less intensity remains.

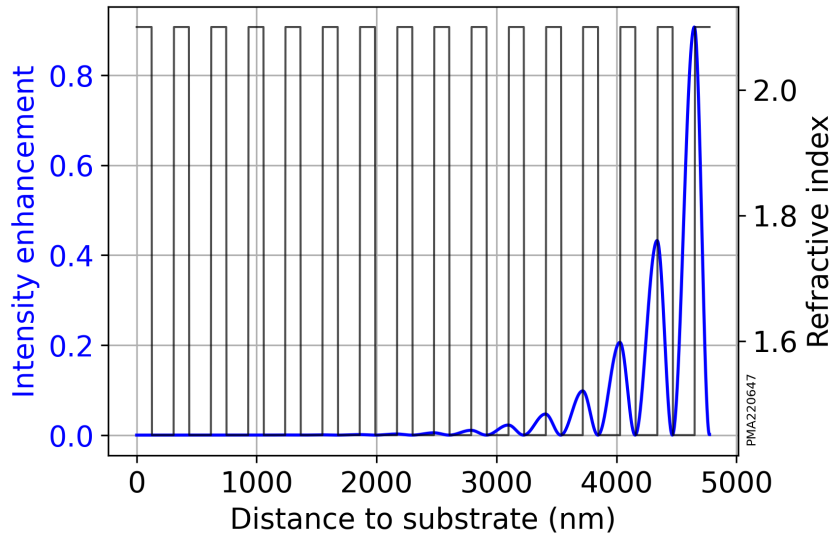


Figure 4.3: The internal intensity enhancement in a QWOT-stack (blue) in combination with the refractive index of the layer materials (gray). The internal intensity enhancement reaches a maximum at the last interface of the layer stack and decreases, the further the radiation propagates into the mirror.

4.2 Band-pass designs

For many applications, spectral filtering or limiting of electromagnetic radiation is desired. One way of achieving a narrow spectrum or selecting a certain spectral range is a thin film band-pass filter. From a coating point of view, the simplest band-pass filter is a variation of the QWOT-stack mirror coating introduced in the previous section. The differences in the coating designs can be observed efficiently when the notation for thin film coatings is utilized. Here, H represents a QWOT-layer of the high- and L a QWOT-layer of the low-index material.

Instead of the $H(LH)^N$ schematic of the mirror, a band-pass features a central spacer layer with a thickness of 2 QWOT. The resulting design schematic then takes the form of $(HL)^N 2H(LH)^N$. This arrangement of layers, in essence, creates a Fabry-Perot cavity with the QWOT stacks at the start and the end of the sequence forming the end mirrors and the central 2 QWOT layer forming the space inside of the cavity. This central layer and similarly utilized layers in optical coatings are therefore called 'spacer layers'. With the analogy of a Fabry-Perot resonator, the principal function of this coating design becomes apparent: Incident radiation is reflected, unless the condition for resonance is fulfilled, meaning that for a wavelength λ of the radiation, a physical thickness d and an index of refraction n the following relation is valid:

$$n \cdot d = 2k \cdot \lambda/2, \quad (4.19)$$

where $k \in \mathbb{N}$. The simple form of a band-pass design introduced above is equivalent to the case for $k = 1$, e.g. the shortest resonator length possible. The previously established transfer matrix formalism can then be used to calculate the properties of the coating design. Figure 4.4 shows the spectral transmittance of a band-pass design with a central wavelength of 1030 nm.

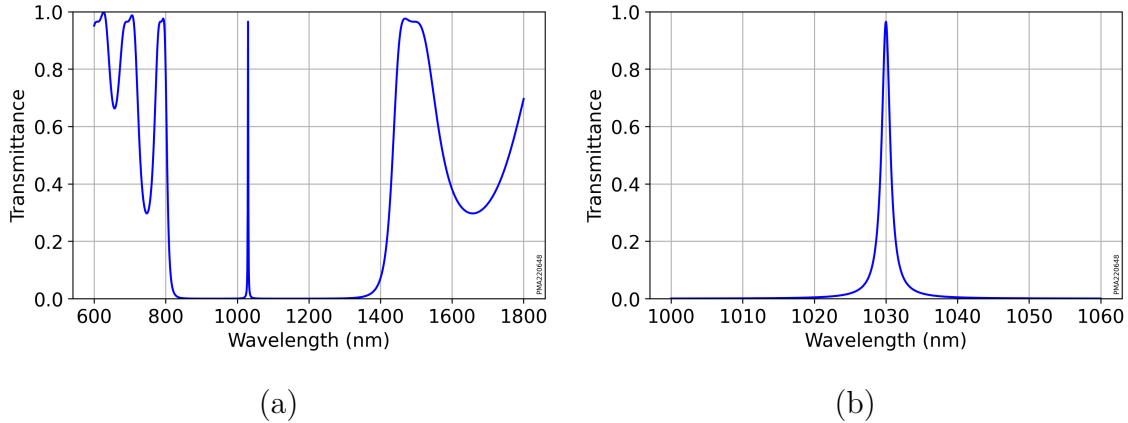


Figure 4.4: The spectral transmittance of a band-pass filter, shown in a (a) wide and (b) narrower spectral range.

As expected from the analogy to a Fabry-Perot resonator, a peak of transmittance at the design wavelength is visible with low transmittance/high reflectance at higher and lower wavelengths. The spectral region of high reflectance is limited by the bandwidth of the mirror coatings, which causes varying transmittance below approximately 800 nm and above approximately 1400 nm, in this case. The analogy is not limited to the transmittance however when the internal intensity enhancement of the coating design is considered. The behavior is again very similar to a Fabry-Perot resonator. Figure 4.5 shows the intensity enhancement in the exemplary band-pass coating. A clear maximum in the central spacer layer can be observed. This enhancement is caused, identical to a classical resonator, by the interference in the 'cavity', which is, in this case, formed by the spacer layer. The decreasing intensity enhancement towards the outer edges is a product of the thin film coatings that form the end mirrors of the resonator. Similar to the distribution of the intensity enhancement in Figure 4.3, the internal enhancement decreases, the further the radiation propagates from the cavity outwards.

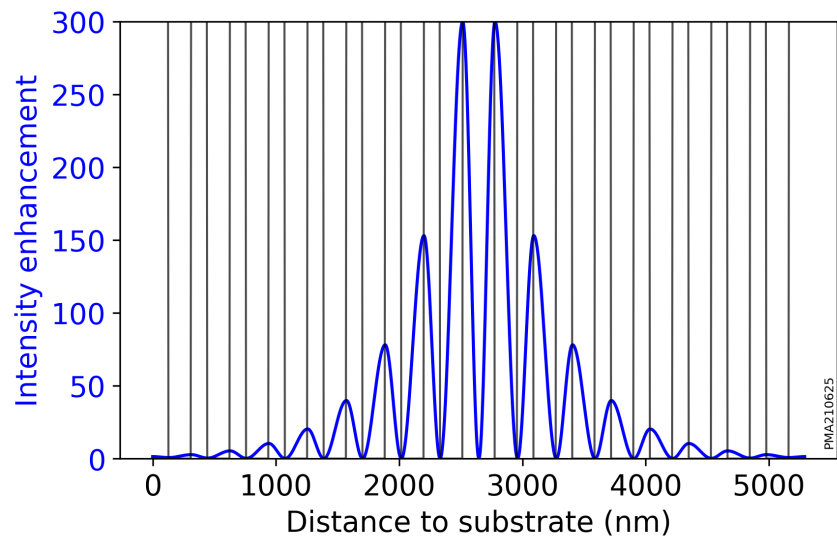


Figure 4.5: The internal intensity enhancement in a band-pass coating (blue) in combination with the refractive index of the layer materials (gray). The internal intensity enhancement reaches a maximum in the central spacer layers of the coating stack due to the resonant nature of the interference in the layer sequence.

5 Kerr-band-switches

This chapter introduces the concept of the **Kerr-Band Switch (KBS)**, a novel optical component intended as an ultra-fast optical switch. To this end, the fundamental idea based on thin film band-pass coatings is explained, and a method for calculation and optimization of the switching function is developed.

5.1 Optical switching with the Kerr effect

The KBS is based on integrating the nonlinear optical Kerr effect into specially designed thin film coatings. To achieve the desired optical switching in these interference coatings, the coating design has to fulfill three principle requirements:

Firstly, the coating stack needs to exhibit the desired spectral behavior in its initial, undisturbed state. For example, for a typical band-pass design, the requirement would be a sufficient transmittance at the central wavelength of the design, as well as a bandwidth that does not limit the later application of the KBS.

Secondly, these desired spectral characteristics should be dependent on a change in optical thickness in one or more of the layers constituting the coating stack. This change in refractive index can then be introduced by the optical Kerr effect and influence the characteristics of the design.

The third property concerns the 'selectivity' of the design. When the design interacts with intense laser radiation during its application, as far as possible, only the layers specified by the second property should change their refractive index, so the design changes its spectral properties in the intended manner. This selectivity can typically be achieved through two methods. When applying the first method, the design needs to enhance the intensity of the incident electric field in the sensitive layers, which will ensure that these layers experience higher changes in the refractive index. The second method relies on the different nonlinear indices n_2 of refraction, different materials possess. If the sensitive layers in the coating stack consist of a material with a, compared to the remaining materials in the coating, much higher n_2 , they will exhibit a stronger shift of the refractive index at the same electric field intensity.

These three properties occur almost 'naturally' in the band-pass designs that were explained in the previous section. Band-pass designs exhibit desirable optical properties at selectable wavelengths. The pass band typically depends strongly on the optical thickness of one or a few selected layers, and the intensity enhancement in these selected layers is typically high. Figure 5.1 presents the spectral characteristics as well as the intensity enhancement of a simple band-pass design addressed to an application wavelength of 1030 nm.

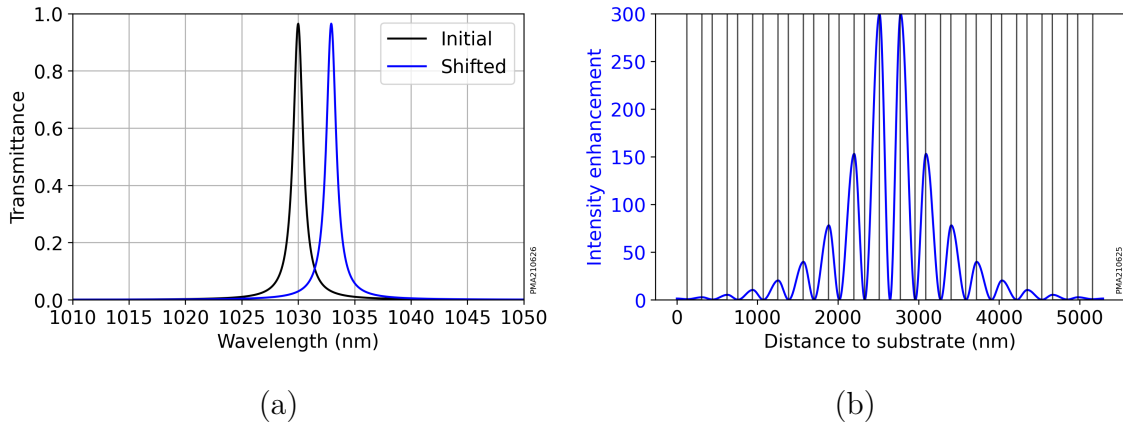


Figure 5.1: (a) The spectral transmittance of a band-pass design intended for an application wavelength of 1030 nm. The black trace represents the initial, undisturbed state, and the blue curve illustrates the "shifted" state, created by an increase in the refractive index of 1% in the central spacer layer. (b) illustrates the enhancement of the intensity of the electric field in the layer stack (blue). A strong enhancement is shown in the central spacer layer. The boundaries of the layers are overlaid for illustration (gray).

5.2 Calculation of intensity-dependent refractive indices in layer stacks

As illustrated in the previous section, the optical Kerr effect can be utilized to initiate optical switching, when electromagnetic radiation of sufficient intensity is provided. The interaction demonstrated is, however, simplified. In real-life interactions, it cannot be assumed that an equilibrium state is reached, because, in addition to the design's transmission spectrum also, the internal intensity enhancement is changed. This, in turn, directly influences the intensity in the active layers, which will consequently change the refractive index of these layers.

To realistically investigate the interaction between a thin film coating and intense laser radiation, the interaction has to be simulated as realistically as possible, includ-

ing the time-dependent intensity of the laser pulse and taking the design's "response" into account. The following sections will detail the simulation process developed in this work as well as give insight into the results obtained by this method.

5.2.1 Simulation process

The simulation process required for analyzing the behavior of Kerr-band-switches can be divided into two parts:

The first part has to be based on the transfer-matrix-formalism explained in Section 4.1.1. It contains all calculations related to the interference coatings, especially the calculation of the internal field enhancement as well as the desired optical properties as, for example, reflection and transmission.

The second part of the software has to handle the external interaction of the layer stack. This includes the properties of the assumed laser source, the shift in the refractive indices caused by the Kerr effect, and the generation of new layer designs with the changed material properties.

In this work, the two parts are handled by different software solutions. The first part is performed by the established thin film software *Spektrum32* [69]. *Spektrum32* is widely used for the design of thin film coatings as well as the fitting of material data to measured spectra. In this work, *Spektrum32* will be interfaced to by using its command line features, which allow control of its capabilities from alternative platforms.

To utilize this control mechanism and handle the tasks of the second software part, a Python program [70] was developed during this work. This program takes control of *Spektrum32* and creates new thin film designs based on the design properties calculated by *Spektrum32*. The next section gives a brief summary of the principle procedure.

5.2.2 Simulation of single pulses

As described in the previous section, the actual thin film calculations are handled by an established thin film software, which is being controlled by a program written in the language *Python* [70]. This program does not only indirectly control the thin film, but also provides additional parameters and iterates the overall process. The steps of these calculations are outlined in this section.

In the explanation presented here, it is assumed that a design intended for switching from transmission to reflection is investigated. After this KBS design is created in accordance with the criteria specified in Section 5.1, the initial state of the field

enhancement and the desired optical properties are recorded. When the initial properties and performance of the design are measured and saved, the design has to be "sliced" into so-called sub-layers with a thickness in the range of a few nanometers. This is necessary because the internal intensity enhancement varies strongly not only over the design but also in each single layer, as can be clearly seen in Figure 5.2 (a). Therefore, the initially constant refractive index of a layer will change to a gradient over the layer, caused by the optical Kerr effect. This effect is illustrated in Figure 5.2 (b), where a comparison between a normal and a shifted design is given.

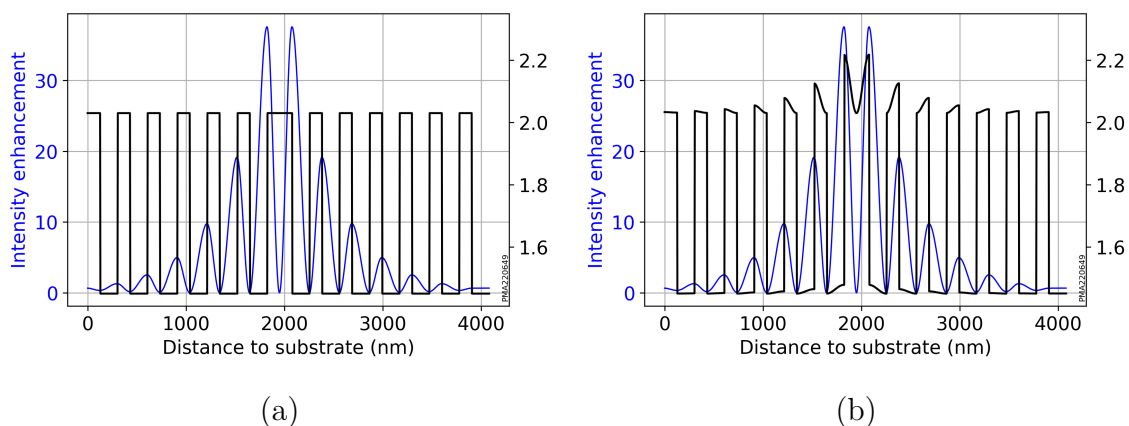


Figure 5.2: (a) The internal intensity enhancement (blue) in a KBS-coating design in combination with the refractive index of the layers (black). (b) shows the same design, but with the effect of the optical Kerr effect taken into account. For the calculations, a $n_2^{\text{high}} = 20 \times 10^{-16} \text{ cm}^2/\text{W}$ and a $n_2^{\text{low}} = 3 \times 10^{-16} \text{ cm}^2/\text{W}$ was assumed for the high- and low index-material, respectively. For the external intensity incident on the design, $I_{\text{ext}} = 1 \text{ TW}/\text{cm}^2$ was chosen to enhance the visibility of the index shift.

Since taking the average of this change would disturb the accuracy of the calculations, the approach of the sub-layers is taken. These sublayers are thin enough that the change of the refractive index over their individual extent can be neglected, and the average of the refractive index is assumed for each single sub-layer. The resulting design of sub-layers can then be treated normally by the thin film calculations to retrieve optical properties and internal intensity enhancement.

This, in principle, enables the calculation of a design's response to a given external intensity. In real applications, the temporal pulse profile of the final laser has to be taken into account, and the incident intensity varies continuously. To calculate the response of a design to a given pulse profile, the incident intensity for each point in time, therefore, has to follow this temporal pulse profile. For the calculations presented in this work, a Gaussian pulse profile was assumed, and calculations starts

$2.4 \cdot \tau_p$ before the peak of the Gaussian pulse profile and ends $2.4 \cdot \tau_p$ after this peak, with τ_p being the **F**ull **W**idth at **H**alf **M**aximum (FWHM) pulse duration in this case. With the basics of sublayers and pulse profile established, a schematical workflow of the software routine for the calculation is given below:

1. During initialization of the calculation, the initial design is loaded, split into sublayers, and the initial properties, in this case, transmittance and intensity enhancement, are calculated by *Spektrum32*. Additionally, the remaining necessary parameters, such as external pulse shape and intensity, nonlinear refractive indices for the coating materials, and number of time steps, are defined.
2. In this step, the current external intensity is calculated based on the pulse profile and the current time step.
3. With the external intensity, the absolute internal intensity is calculated based on the internal intensity enhancement of the current step in the iteration.
4. The internal intensity is, in combination with the nonlinear refractive indices, used to calculate a new index of refraction for each sublayer to create a new design for the current iteration.
5. The new design is handed over to *Spektrum32* for calculation of transmittance and intensity enhancement. The results are saved for later evaluation.
6. After saving the results, the current iteration is finished. When the current time step is not the last one, the current time step incremented, and the calculation returns to step 2. When the last step is reached, the calculation stops.

This procedure enables the observation of the interaction between a KBS design and a single pulse of electromagnetic radiation with a fixed pulse energy/peak intensity. An example of this is presented in Figure 5.3, where the simulation results for a KBS-coating are presented.

The coating design depicted in the figure follows the schematic $(HL)^8 2AL(HL)^8$, where the central spacer of the active material with thickness 2 QWOT is denoted by the letter A . The refractive indices of the materials assumed for this simulation are $n_H = 2.03$ for the high-index and $n_L = 1.44$ for the low-index material. The nonlinear refractive indices of the materials were assumed to be $n_{2,H} = 20 \times 10^{-16} \text{ cm}^2/\text{W}$ for the high index material, $n_{2,L} = 3 \times 10^{-16} \text{ cm}^2/\text{W}$ for the low index material and $n_{2,A} = 2 \times 10^{-12} \text{ cm}^2/\text{W}$ for the active material. For this coating design, the effect

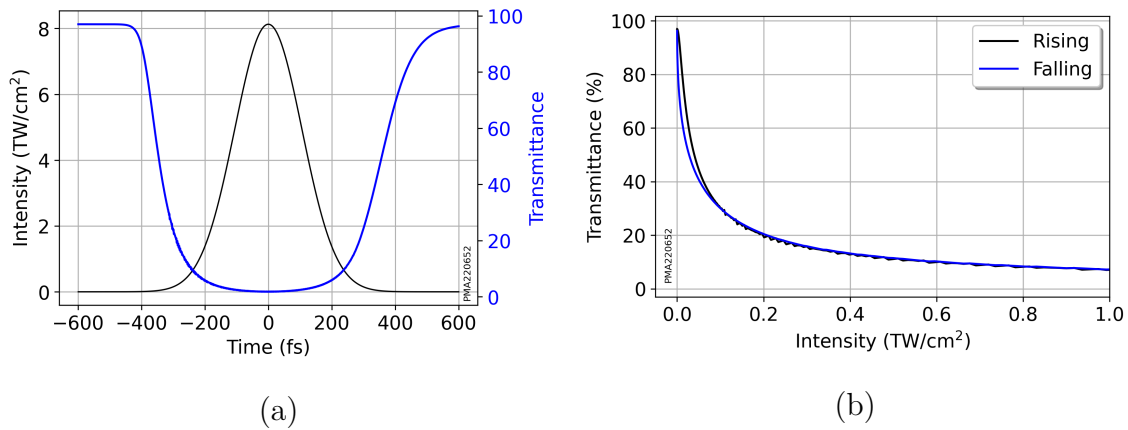


Figure 5.3: The behavior of a KBS-coating during the interaction with a single Gaussian pulse. (a) shows the intensity of the electromagnetic radiation and the transmittance of the KBS over the time of the simulation. A strong reduction of transmittance can be observed during the peak intensity. (b) shows the transmittance of the coating plotted over the incident intensity, separated into the rising and falling side of the Gaussian profile.

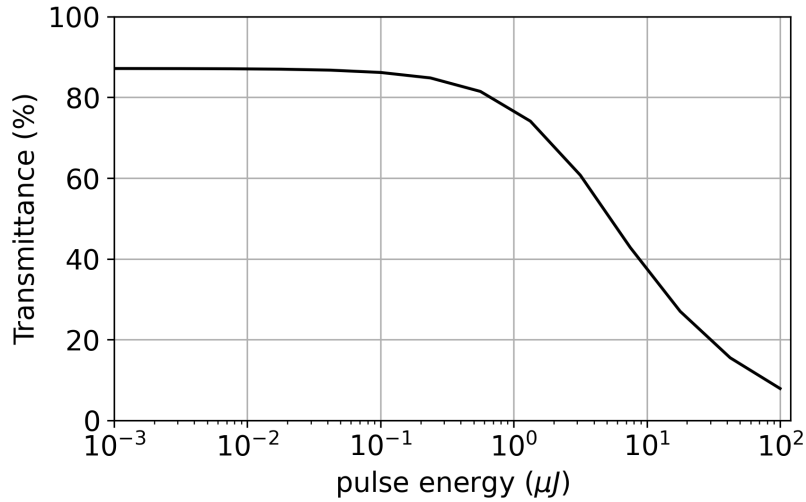
of a laser pulse with a duration of 250 fs, a pulse energy of 100 μJ , and a spot size of 100 μm was calculated.

Figure 5.3 (a) shows the intensity of the electromagnetic radiation incident on the KBS and its transmittance over the time of the simulation. At high intensities, the transmittance is strongly reduced, which is the behavior that was intended in designing the KBS. Figure 5.3 (b) shows the transmittance over the incident intensity separated into the rising and falling side of the Gaussian profile.

For later application as well as easier comparison with validations, the behavior for pulses with different pulse intensities is of high interest. To evaluate this behavior, the established simulation routine, which loops over the temporal profile of a pulse with fixed peak intensity, is, in turn, integrated into a loop to evaluate the performance of a KBS design over its complete range of applications. The resulting characteristic curve of the transmittance of the design versus the pulse energy of the incident pulse is given in Figure 5.4.

The calculation of the characteristic switching curve of a design then allows the comparison between different design approaches and enables the validation with experimental data, because the characteristic curve can be measured with relative ease, especially when compared to the single pulse curves presented in Figure 5.3. But to further improve the performance of the KBS, the switching mechanism has to be optimized in software.

This is already common practice in current thin film design, where commercial software is used almost universally for the creation of advanced coating designs. A



PMA220606

Figure 5.4: The transmittance for various pulse energies of the incident radiation. A clear decrease in transmittance can be observed for increasing pulse energies, which is caused by the optical switching in this KBS design.

similar approach is presented in this work in Section 5.2.4, but for any optimization algorithm to be effective, a figure of merit has to be defined that can be used to compare the performance of different variations of a design candidate.

5.2.3 Figure of merit

When different design candidates are compared with regards to their switching performance and designs are being optimized for larger switching amplitudes, it is critical to have an accurate **Figure Of Merit** (FOM) to analyze said performance. In the simulations presented in this work, mainly the change in transmittance is used as an indicator for a valid KBS design. There are two challenges to a naive approach of calculating and comparing the two characteristic switching curves of the candidates under consideration that make this approach not feasible for application in realistic simulations.

Firstly, a calculation over the complete peak intensity range intended for later applications is time-consuming. Therefore, instead of using the complete range of peak intensities, a single intensity is used as point of reference for a design's switching performance. This point is determined in the first evaluation of a new design and set to an intensity at which the transmittance of the design roughly reaches 50% of its initial value ($I_{50\%}$).

Secondly, when the switching performance of designs shall be improved by optimizing algorithms, taking the transmittance at the reference wavelength as a parameter

leads to erroneous results. The optimization will, in this case, naturally lead to spectrally narrower transmission bands with higher internal intensity enhancement. While this would improve the switching performance for spectrally limited radiation, the ultrashort pulsed lasers with pulse durations of around 10 ps and shorter, which are the main application for KBS typically feature bandwidths greater than 0.1 nm. Very narrow designs will therefore limit the initial transmission and switching amplitudes because they can only interact with a small part of the pulse spectrum of the incident radiation. To avoid this, the spectral bandwidth of the design has to be included in a FOM chosen for this optimization problem. Different FOMs were tested during the course of development of the KBS-optimizations, and the following was found to perform best.

The FOM is determined by first calculating the undisturbed transmittance spectrum of a design candidate and subtracting the transmittance spectrum of the same design at $I_{50\%}$. The resulting difference of the two spectra is then integrated over the range of the bandwidth previously defined for the particular application the design candidate is being optimized for. This integral is divided by the bandwidth for normalization. This results, in effect, in the averaged change of transmission in the desired spectral range, which is the FOM applied in this work.

5.2.4 Optimization of KBS designs

With the capabilities described in the previous section, the characteristic switching curve of a KBS design can be calculated and compared with other design approaches. This directly enables the programmatic optimization of the switching properties. In this work, the optimization is implemented using the previously established software solution in combination with random variations of the layer thicknesses. The implementation follows the schematic presented below:

1. In the first step, the initial design is loaded, and the initial switching curve and figure of merit (FOM) are calculated. The results are saved for later comparison. The remaining parameters for the optimization are also defined in this step, such as the total number of steps, bandwidth of the intended application, the pulse energy range for the calculation of the characteristic switching curve, and the parameters of the intended laser source the component is going to be used with.
2. The FOM is calculated as defined in Section 5.2.3 and saved for later comparison.

3. The layer thicknesses are randomly varied with the maximum variation set initially at 1 % of the layer thickness.
4. Since all layers are varied, any spacer layers that may define the resonant wavelength of the design will also be affected. Any shift in these layers causes the design to shift out of resonance, and switching will not happen, since no initial intensity enhancement is present. To mitigate this, the new shifted transmittance peak created with the current iteration is detected, and the complete design is shifted so that the wavelength of the current transmittance peak matches that of the initial design.
5. The switching behavior for a single pulse with a peak intensity of $I_{50\%}$ is calculated, and the FOM is calculated for the design of the current iteration.
6. The calculated FOM of the current iteration is compared to the currently best FOM (or the initial if no better FOM was identified). If the current FOM is better, the current design is saved and used for further calculations. If the current FOM is worse, the currently best design remains unchanged, and the number of steps without improvement is incremented.
7. If the number of steps without improvement reaches a limit (typically 5, for calculations in this work), the maximum variation of the layer thickness is reduced. This allows a better resolution of minima in the FOM later in the optimization process, while initially enabling the finding of an overall good minimum at the start.
8. If the number of the current step is smaller than the total number of steps set for the optimization, the process returns to step 3. When the number of steps is equal to the set limit, the optimization loop is terminated, and the currently best design is saved as the final design.
9. The characteristic switching curve of the final design is calculated and saved for comparison with the initial design.

An exemplary result of this optimization algorithm is presented in Figure 5.5. The two included designs exhibit a similar characteristic switching curve, but the optimized variant has a higher initial transmittance and starts to 'switch', e.g. its transmittance starts to decrease, at lower pulse energies. Both effects can be explained by the optimization process, as both the higher initial transmittance as well as, the earlier decrease of transmittance increase the difference between the undisturbed transmittance spectrum and the spectrum at an intensity of $I_{50\%}$, which in

turn increases the FOM. It can be observed that the pulse energies necessary for switching of the KBS could be decreased by almost an order of magnitude, which is a significant improvement.

A comparison between the transmittance of the initial and the final designs is presented in Figure 5.6. Minor differences are visible, but no significant change in the transmittance spectrum can be observed. Figure 5.6 (b) shows the transmittance peak of both designs, and the optimized variant has a slightly smaller bandwidth, which could explain a part of the seen improvements.

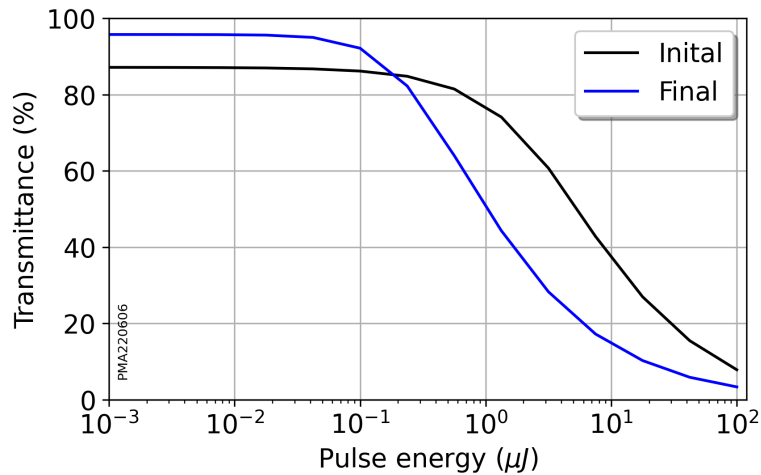


Figure 5.5: The transmittance for various pulse energies of the incident radiation. A clear decrease in transmittance can be observed for both designs, but the optimized candidate (blue) has higher initial transmittance and starts to decrease at lower energies.

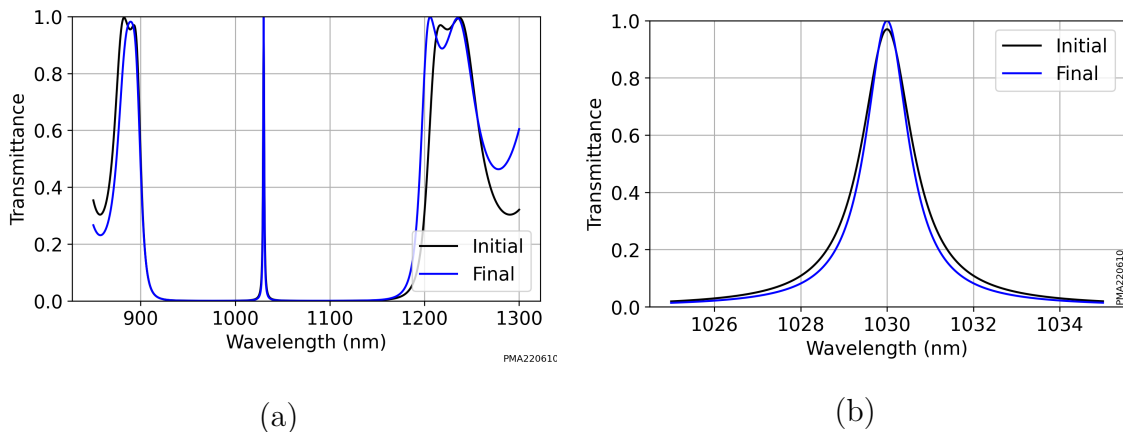


Figure 5.6: The transmittance of an initial band-pass design (black) and a KBS design that was optimized for switching amplitude. The optimization causes minor changes to the spectral shape of the transmittance, but the original pass-band is clearly recognizable.

5.2.5 Beam profile considerations

So far, only the temporal shape of the Gaussian beam was considered for the simulations and optimizations. The spatial profile of the intensity was assumed to be homogeneous, e.g. equivalent to a flat top beam shape. Most laser systems, however, feature a Gaussian spatial intensity profile, or a profile that closely resembles a Gaussian shape. For the switching function of the KBS under consideration in this chapter, the inhomogeneous spatial intensity distribution of this beam profile effectively means that the results presented up to this point are only valid for the peak intensity of a Gaussian beam, and the switching is going to be less pronounced for points with a greater distance to the beam's center due to the reduced intensity. To estimate the difference between the simulations performed for a flat-top beam profile and a Gaussian profile that is closer to real-life laser systems, the switching characteristic of a KBS as displayed in Figure 5.6 can be utilized. Each data point in that graphic represents the averaged transmittance of a laser pulse with a temporal Gaussian shape. The different pulse energies represented in this graph can then be converted to the peak intensity of this temporal pulse shape. This information can be used to calculate the switching performance of a spatial Gaussian beam profile, by approximating the local switching amplitude for every point in the beam profile with the switching amplitude of a pulse with matching peak intensity.

Due to the rotational symmetry of a Gaussian beam, this results in a radial dependency of the transmittance $T(r)$ for a given beam profile. An example of $T(r)$ for the pulse parameters described in Section 5.2.2 is depicted in Figure 5.7 (a). By integrating $T(r)$ over the beam area in polar coordinates and normalizing the result to the total beam area, the average transmittance of a Gaussian beam profile T_G can be calculated:

$$T_G = \frac{1}{\pi R^2} \int_0^{2\pi} \int_0^R T(r) \cdot r \, dr \, d\varphi = \frac{2}{R^2} \int_0^R T(r) \cdot r \, dr. \quad (5.1)$$

The radius of the beam's area cannot be exactly defined for a Gaussian beam. For the calculations presented here, the maximum radius R of the integration is equal to the $1/e^2$ -radius w that is the established measurement for the size Gaussian beams and contains approximately 86.5 % of the beam's energy.

The resulting transmittance for different peak intensities of a Gaussian beam together with the same intensities of a flat-top beam is presented in Figure 5.7 (b). For the same intensity value, the Gaussian beam shows a reduced switching amplitude. The difference between the two beam shapes varies depending on the intensity

5 Kerr-band-switches

and reaches a maximum of approximately 22%. The function of the KBS seems to be identical qualitatively but shifted to higher intensities for the Gaussian beam.

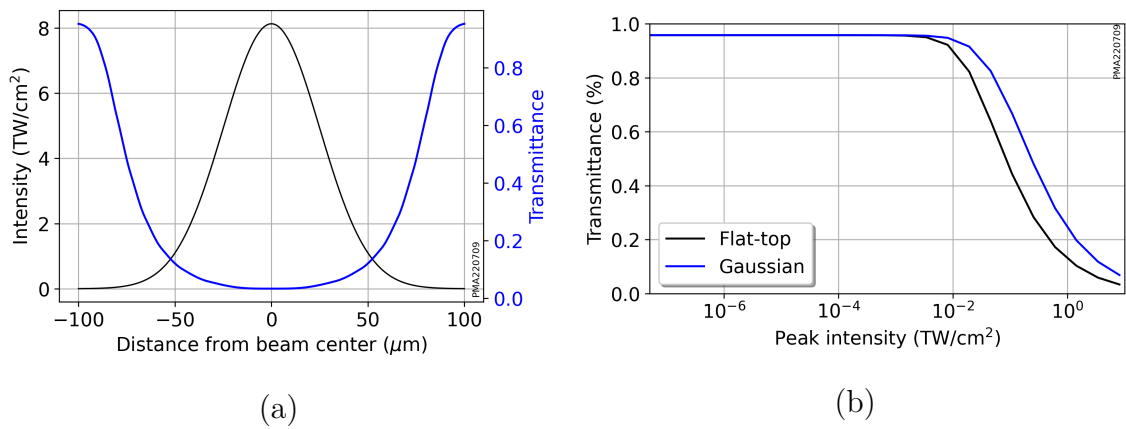


Figure 5.7: The radial dependency of the transmittance during the interaction of a Gaussian beam and a KBS. (a) The black line represents the spatial intensity profile of the laser pulse, and the blue line represents the transmittance at each distance to the beam's center. In (b), a comparison of the switching obtained by a flat-top and a Gaussian shape for an identical KBS is depicted. The function of the KBS seems to be identical qualitatively but shifted to higher intensities for the Gaussian beam.

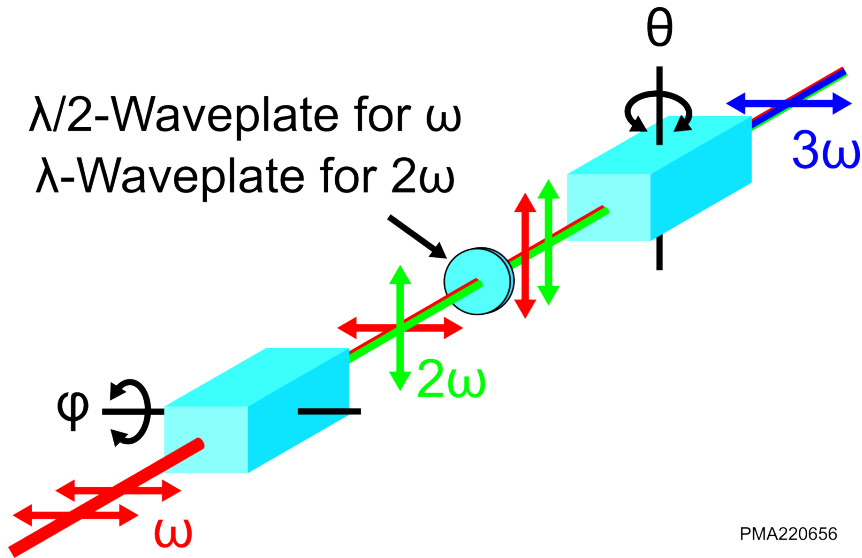
6 Frequency tripling mirrors

Since the most established laser gain media operate in the near-infrared spectral range around $1\ \mu\text{m}$, the generation of the third harmonic of these fundamental laser wavelengths is of high interest for many applications based on ultraviolet radiation [71, 72, 73]. The most straightforward way to obtain this third harmonic is the direct third harmonic generation as described by Equation 2.8 in Section 2.1. But because the two wavelengths participating in this conversion process are spectrally far apart, the natural dispersion of the refractive index makes phase matching very difficult for this direct THG, and additional effects or construction techniques have to be utilized to achieve meaningful efficiencies [74, 75]. Therefore, the most efficient way to generate the third harmonic of an infrared laser currently is the combination of two second-order nonlinear processes. With these, the fundamental firstly gets converted into its second harmonic by direct second harmonic generation and secondly into its third harmonic by sum frequency generation of the fundamental and the newly generated second harmonic [76, 77]. This process is highly efficient, with conversion efficiencies of about 30 %, but the optical setup is relatively complicated, requiring multiple components in a free-space setup. A schematic representation of the necessary components is presented in Figure 6.1.

As an alternative to the inefficient direct THG and the complicated generation via two second-order processes, frequency tripling mirrors based on thin film interference coatings were proposed and will be investigated in this section. The original concept was developed at the University of New Mexico (UNM) [79, 80]. The concept was further investigated in cooperation with the Leibniz University of Hannover (LUH) and the LZH in a combined research project, where the work presented in this thesis took place.

6.1 Third harmonic generation in thin film coatings

Thin film interference coatings offer the possibility to freely tailor the optical properties of the component to be manufactured. These properties include transmittance and reflectance, but also dispersion and phase characteristics, which are exploited



PMA220656

Figure 6.1: An example of a THG-process based on two second-order nonlinear processes. In the first step, the fundamental is converted to the second harmonic. The polarization of both waves is then aligned by a wave plate, and by an SFG-process the third harmonic is generated in the second step. The phase matching for both conversion processes is done by tuning the respective angles ϕ and θ . Schematic recreated from [78].

in chirped mirrors, for example. In addition, the laser-induced damage threshold of these coatings can greatly exceed those of metallic mirrors [81, 82]. The combination of these advantageous properties suggests that with the correct design of the layer sequence, interference coatings can be utilized as nonlinear conversion media. In this application, the phase mismatch naturally occurring in the coating materials would be compensated by phase delays intentionally designed into the coating stack. In addition to this degree of freedom created by the properties of the interference coating, the inclusion of resonant structures enables high internal field enhancements meaning any external laser radiation will be enhanced in selected layers used for the conversion process. This is similar to the band-pass structures utilized in Kerr-band-switches introduced in Section 4.2.

The design of frequency converting optics was developed by the UNM and investigated in detail in the Ph.D. work resulting from the joined research project [83]. Here, a brief summary of this method is presented. In principle, the intensity of the third harmonic generated in a coating is calculated by implementation of the conversion without depletion of the fundamental as described by Equation 2.22 with the thin film matrix formalism as described in Section 4.1.1. The input parameters for this formalism are the layer thicknesses \vec{d} , the complex refractive indices of the corresponding layer materials \vec{n} and their nonlinear susceptibilities $\vec{\chi}^{(3)}$. The vectors

contain $(N + 1)$ elements, with the first N components describing the layer stacks and the $(N + 1)$ th component describing the substrate material. This calculation method then yields the forward and backward traveling waves of third harmonic radiation and allows the calculation of the efficiency of the in-stack conversion.

The overall energy of the conversion in reflection S_{TH} is then defined by the peak amplitude of the incident fundamental field radiation $E_{\text{F},0}$, an integral over the normalized temporal and spatial pulse shape of the fundamental field $\hat{E}_{\text{F}}(t, r)$, with $\hat{E}_{\text{F}}(0, 0) = 1$, and a quality parameter $q(\vec{d}, \vec{n}, \vec{\chi}^{(3)})$ resulting from the matrix calculations:

$$S_{\text{TH}} = q(\vec{d}, \vec{n}, \vec{\chi}^{(3)}) |E_{\text{F},0}|^6 \int dt \int d^2r |\hat{E}_{\text{F}}(t, r)|^6 = q |E_{\text{F},0}|^6 K \quad (6.1)$$

The constant K is the numerical value resulting from the temporal and spatial integration of the laser pulse. The quality parameter q is the figure of merit that is maximized by the optimizations. The FTM coatings presented in this work can be separated into three approaches, labeled A, B, and C. The difference between these design types mainly lies in the way the figure of merit is chosen: Designs of type A are optimized towards the highest absolute THG. Therefore the corresponding figure of merit q_{A} is equal to q from Equation 6.1. Designs of type B use a changed figure of merit q_{B} , with

$$q_{\text{B}} = q_{\text{A}} \left| \frac{E_{\text{F},0}}{E_{\text{F},\text{max}}} \right|^6 =: q_{\text{A}}/f^6 \quad (6.2)$$

Effectively, q_{A} is related to the maximum internal field enhancement f of the layer stack, leading to a preference for designs that create high third harmonic energies at low internal intensities. This assumes that the external intensity can always be increased, for example, by focusing the incident laser beam. The conversion efficiency η for the coating stack can be calculated by dividing the TH-energy S_{TH} by the fundamental energy $S_{\text{F}} = |E_{\text{F},0}|^2 K'$. Here, K' is a numerical constant relating the electric field of the fundamental to its energy.

$$\eta = \frac{S_{\text{TH}}}{S_{\text{F}}} = q_{\text{A}} \frac{1}{f^4} |E_{\text{F},\text{max}}|^4 K'' = q_{\text{C}} |E_{\text{F},\text{max}}|^4 K'' \quad (6.3)$$

The factor $K'' = K/K'$ is again a constant numerical factor related to the temporal and spatial integrals of the fundamental and TH-pulses. The quality parameter $q_{\text{C}} = q_{\text{A}}/f^4$ is the figure of merit for type C-designs. Similar to designs of type B, the figure of merit is normalized in relation to the internal intensity enhancement, but instead of favoring high TH-energies, high conversion efficiencies are preferred.

6 Frequency tripling mirrors

Designs of all three types were manufactured and tested, but since the main goal was to produce an alternative method for high-efficiency THG, the designs investigated in detail in this thesis are of type C.

7 Manufacturing of thin film coatings

After developing the theoretical foundations for this work and a discussion of the required optical materials, this chapter will describe the processes applied for manufacturing the coatings.

There are various ways of achieving a functional surface for optical applications. The most common way of functionalizing polished surfaces, however, is by applying an optical coating. The manufacturing processes for these coatings are commonly divided into two major groups: Chemical vapor deposition and physical vapor deposition [36]. Optical coatings are mainly produced by the latter. Physical vapor deposition itself can be further divided into three groups of processes. The first group consists of so-called conventional coating processes based on evaporation of the coating materials. This group is further subdivided into classical thermal evaporation, where a metal crucible (called boat in this application) containing the coating material is heated by passing an electrical current through it, and electron beam evaporation, where the heating is done by an intense electron beam, which is directed at the coating material [84]. Evaporated coatings show good optical quality and have a wide selection of materials available, but the properties of the deposited thin film materials usually are not as good as that of similar bulk materials. Due to the thermal nature of the process, the evaporated molecules and atoms usually have relatively low kinetic energy, which leads to layers with porous columnar microstructures [85].

The second group of processes contains plasma-based approaches. Here, the coating material is not evaporated but sputtered by a high-energy plasma. Due to the high energy of the sputtered atoms, plasma-based processes produce layers with higher density and lower losses, but they are usually slower than conventional processes. There are many different approaches on how to create a suitable plasma, especially magnetron-sputtering and **Ion-Beam-Sputtering** (IBS) are well-established processes. IBS, especially is known to produce layers with extremely high precision and the lowest achievable losses known so far. The coatings used for the research

done in this work were manufactured by IBS-machines. Therefore, a short overview of the IBS process as well as the machines used for work in this thesis, is given in the following sections.

7.1 Ion beam sputtering

The IBS coating process is based on the generation of plasma, which is spatially separated from the substrates and the target materials. The separated generation allows the plasma to be kept very stable for long process times. By using a charged grid system integrated into the plasma source, ions can be extracted and used for sputtering. The acceleration provided by the grid system provides the kinetic energy for the ions, which typically is in the low, single-digit kV range. To avoid potential build-up of electric charge in the target materials, the ion beam is often neutralized by the insertion of electrons before interacting with the target. A schematic representation of an IBS-machine as it is typical for the coatings presented in this thesis, is depicted in Figure 7.1. After acceleration, the ions or neutralized atoms hit the target material. The interactions between the highly energetic particles and the atoms of the target material are complex, and different possible processes can occur. A detailed investigation of the fundamental solid-state-processes was developed in [86, 87, 88].

The dominant interaction is the so-called linear collision cascade, whereby the energetic particles dissipate their energy in a small volume of approximately 1 nm^3 on the target surface. The resulting probability for emission of a target atom is relatively low (in the order of 5 % to 25 %) [89]. This inefficiency leads to a significant energy transfer to the target material, which, therefore, often requires active cooling during the deposition process. To achieve sufficiently high free path lengths in the coating chamber and reach the substrates in their plane of rotation, the process has to be undertaken in a high vacuum, with evacuation pressures down to 1×10^{-7} mbar and process pressures of approximately 1×10^{-4} mbar. The sputtered target atoms (ad-atoms) leave the target, creating a complicated distribution in the plane of the substrates to be coated, which is the result of a superposition of different effects [90]. Therefore, the distribution of the coating material tends to be strongly inhomogeneous in the plane of substrates, which typically requires masks combined with rotating substrates to reduce the deposited material in certain areas. For even higher lateral homogeneity, planetary rotation or other forms of mechanical averaging can be employed [91]. Since metallic or semiconductor target materials are typically used for IBS coatings, the sputtered atoms require additional oxygen in the

coating process to form the desired dielectric oxide layers on the substrate surface. This oxygen is provided in gaseous form during deposition, making it a reactive sputtering process. The rate of deposition of IBS layers typically depends on the sputtered material and the layout of the specific coating machine but is relatively stable over time. As depicted in Figure 7.1, several target materials are implemented that enable the changing of coating materials necessary for multilayer interference coatings without disturbing the vacuum in the coating chamber.

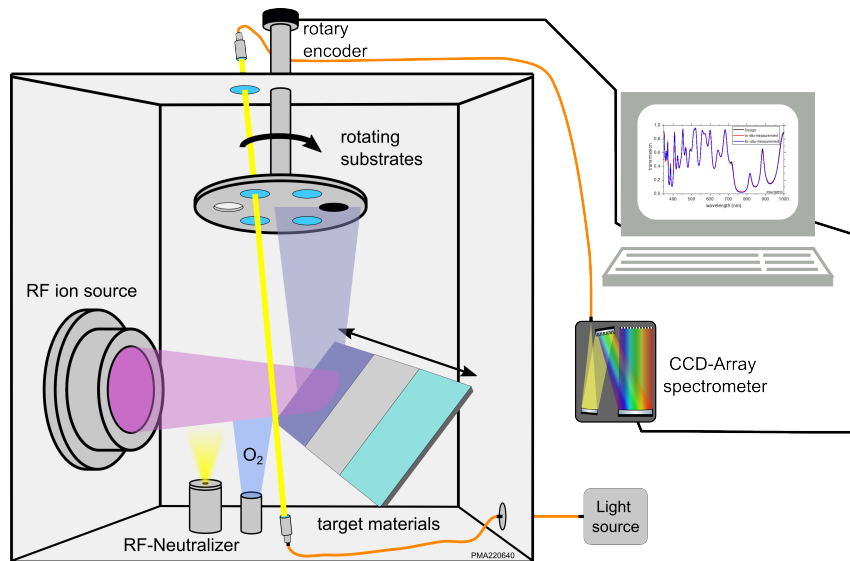


Figure 7.1: An illustration of an IBS coating machine. The accelerated ions from the ion source are neutralized and hit the target material. Sputtered atoms from the target material then move toward the substrates, which are mounted in a rotating holder over the target. To generate oxidic layers from metallic targets, additional oxygen is supplied.

7.1.1 Monitoring of the deposition process

The stable nature of the IBS coating process results in nearly constant deposition rates. In theory, therefore, the layer thicknesses obtained from an IBS deposition can be determined purely by using a well-calibrated coating machine together with precise time control. In practice, however, changing target geometry due to sputtering, changing substrate temperatures other error mechanisms cause small deviations in deposition rate and optical properties of the deposited parameters, which necessitates direct monitoring of the deposited layer.

An effective method for control of optical thicknesses is the measurement of transmitted light through a special, well-known monitoring sample. Since the transmittance of the optical coating depends on the thickness of the applied layers, the transmitted

light can be used to monitor the progress of the coating process. Early implementations measured transmittance at a single wavelength (which may change from layer to layer) and terminated the layers based on the turning points of the transmittance [92]. An example of the transmittance at the central wavelength of a QWOT-stack mirror is presented in Figure 7.2. The extreme points of the transmittance curve are located at the layer boundaries, which enables easy termination of these layers. The software necessary to perform the optimization that calculates the current layer thickness after each measurement and recalculates the material properties during the deposition is developed at LZH [93] and greatly improves the accuracy of layer deposition.

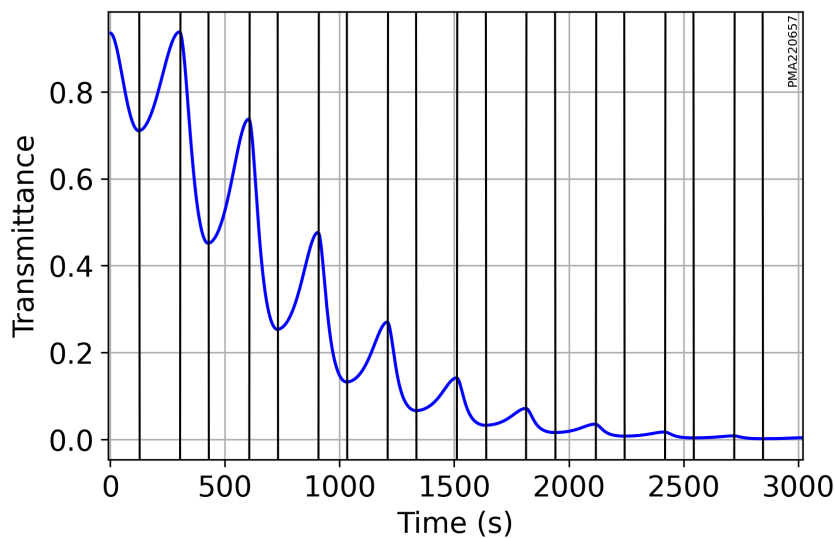


Figure 7.2: An example of the signal created by a single wavelength optical monitor during the deposition of a QWOT-stack mirror coating for 1064 nm with 23 layers of Ta_2O_5 and SiO_2 . The extreme points of the transmittance curve are located at the boundaries of the layer, which enables easy termination of each layer during deposition.

While this works well for designs, which feature mostly QWOT-layers and are intended for use at a dedicated laser wavelength, the number of wavelengths for monitoring as well as the complexity of the required monitoring strategy, increases greatly for more complicated coating designs. Additionally, there is no information about the optical properties of the deposited materials, which then have to be determined beforehand.

A solution to these disadvantages of a single wavelength monitoring approach is offered by the so-called **BroadBand-Monitor** (BBM) [94]. Here, the spectral transmittance is measured in a broad range, typically around the visible spectrum e.g. from 400 nm to 1000 nm. Technically, this is realized by a light source that is cou-

pled via optical fibers into the coating chamber. The light is then irradiated onto the samples' path of rotation, and the transmitted light is collimated back into an optical fiber. The transmitted light is then measured spectrally by at least one fiber-coupled spectrometer. If necessary, special thin film filters can be inserted into the beamline to flatten the spectrum and provide a better signal-to-noise ratio for the spectrometers. To measure the absolute transmittance of the monitoring sample in the coating machine, three measurements have to be taken: First, a dark measurement $I_{\text{dark}}(\lambda)$ containing the offset of the spectral intensity measurement and any scattered light that might result from light sources in the coating chamber e.g. the ion source or the neutralizer. Secondly, a 100%-measurement is recorded by measuring the spectral intensity distribution $I_{100}(\lambda)$ of the light source without the sample in the beamline. Finally, the spectral intensity distribution $I_{\text{sample}}(\lambda)$ transmitted by the sample is recorded. The absolute transmittance of the sample T_{sample} .

$$T_{\text{sample}} = \frac{I_{\text{sample}}(\lambda) - I_{\text{dark}}(\lambda)}{I_{100}(\lambda) - I_{\text{dark}}(\lambda)} \quad (7.1)$$

The different measurements in the same beamline are possible due to the arrangements of the samples in their rotating holder. The holder features at least one spot for a monitor sample, and in addition, a hole without any sample where the 100 %-measurement can be recorded as well as a closed spot for the dark measurement. The different angular positions at which the measurements are recorded are set once by the user of the coating machine and are then reproduced by an encoder coupled with the axis of rotation. Therefore, by spinning the sample holder, these measurements can be taken each once per revolution, enabling the possibility of frequent sampling of the sample's spectral transmittance.

These measurements alone do not yet provide insight into the state of a coating in progress. Only in combination with the known coating design as well as suitable software to fit the current layer thickness to the recorded spectral transmittance a thickness value can be retrieved. In contrast to single wavelength monitoring, the availability of complete spectral information over the coating allows not only the determination of the layer thickness but also the in-situ calculation of the refractive index and its spectral dispersion over the measured spectral range [93].

7.2 Coating of Kerr-band-switches

The coating process of KBS does not deviate significantly from the process for coating more typical optical components, except for the active materials involved. In this thesis, an IBS coating machine based on a commercial 16 cm *Veeco* RF high-power ion source is used. The source is operated with an acceleration voltage of 1000 V and beam currents between 450 mA for the dielectric materials and 350 mA were applied. Argon is utilized as process gas for the ion source. The targets for the dielectric materials consist of pure tantalum and silicon. As active material, ITO is sputtered from an alloy target consisting of 90 % indium and 10 % tin. To obtain oxidic layers, oxygen gas is supplied during the sputtering process. The vacuum chamber of the coating machine is evacuated with a combination of a mechanical pre-pump and a turbomolecular pump, reaching a baseline pressure of approximately 1×10^{-6} mbar and a pressure of approximately 3×10^{-4} mbar. The inside of the coating machine is depicted in Figure 7.3.

The coating process is controlled with a BBM using an incandescent lamp as light source and an *AvaSpec-2048x16-ULS-USB2* spectrometer. This combination of a light source and spectrometer allows the measurement of spectral transmittance in a range between 400 nm and 1050 nm with a resolution of approximately 1 nm.



Figure 7.3: The coating machine used for the production of KBS. In the bottom right, the three target materials can be seen (arranged front to back). In the upper center, the rotating substrate carrier can be observed next to the ion source on the left.

7.3 Coating of frequency tripling mirrors

The frequency tripling mirrors described in Section 6 are very challenging to manufacture when compared to more typical optical coatings. The conversion efficiency of the components relies on the internal intensity enhancement of the fundamental wavelength in the coating designs. This, in turn, is strongly dependent on the optical layer thickness of the resonant layers. From this demand for an accurate optical thickness, it follows that both the physical thickness of the deposited layers, as well as the refractive index of the coating materials, need to be well-known. In addition to these requirements, which similarly have to be met for all high-precision designs, frequency tripling mirrors have to meet additional targets for the third harmonic of the fundamental wavelength. Because of the critical phase matching in the layer stack, which relies on the designed path length differences and index differences in the layer stack, all layer parameters in the coating process have to match those used for the simulation of the coating design.

This leads, in effect, to a close feedback loop between the coating process and the design process. The material parameters of the coating process have to be determined precisely and continuously monitored over the operation of the machine. This requires high-end monitoring systems, both in-, and ex-situ, as well as evaluation software for the recorded data. The gained information about the coating process is then used for the creation of a tailor-made coating design, which is (in theory) only valid for one coating run. However, because the operation of the coating machine during the deposition of further designs typically causes minute changes in the optical properties of the materials, a new design has to be generated for every coating run. To fulfill these critical requirements for the coating process, a coating machine was adapted for high-precision operation.

The coating machine employed for the production of frequency tripling mirrors is based on a commercial 6 cm *Veeco* RF-ion source operating at 13.5 MHz. The source is comprised of a discharge chamber, where the plasma is generated and a grid extraction system. The extraction system contains three grids, which accelerate and focus the ion beam onto the target material. As indicated in Figure 7.1, an additional RF-neutralizer supplies electrons for the neutralization of the charged ions in the beam to avoid charging of the target materials. The source can be operated using argon or xenon gases, but the coatings presented in this work were produced using argon exclusively. The source can supply ion beams with currents of up to 150 mA at acceleration voltages of up to 1500 V. To change the coating material during deposition, the target materials are mounted on a mechanical translation stage (modified *Aerotech-Pro165*) with a range of 300 mm. The targets are mounted at an

angle of 55° to the incoming ion beam. A mechanical, oil-free scroll pump (*Edmunds XDS46i*) is used to create the pre-vacuum at approximately 1×10^{-1} mbar and a turbomolecular pump (*Trinos*) for generation of high vacuum with levels down to 1×10^{-6} mbar. During the deposition process, the chamber pressure is slightly increased to approximately 3×10^{-4} mbar due to the argon and oxygen gases necessary for the deposition process.

The materials employed for the deposition of the frequency tripling mirrors are HfO_2 as a high refracting material and SiO_2 as low refracting material. Both materials are sputtered from pure elemental targets, and deposition rates of approximately 0.05 nm/s for HfO_2 and 0.1 nm/s for SiO_2 could be achieved.

7.3.1 High-resolution broadband-monitor

To match the requirements for the production of frequency tripling mirrors, the standard BBM was changed to a high-resolution UV broadband monitor (HR-BBM), which enables the direct observation of the dispersive properties of the applied optical materials in the relevant spectral regions around the fundamental at 800 nm and the third harmonic at 266 nm. The high resolution, in conjunction with extended spectral range, was achieved by splitting the transmitted light between seven separate spectrometers (*AvaSpec-2048x16-ULS-USB2*), each with a spectral range that slightly overlaps those of its neighbors. The spectral ranges and resolution in each range are listed in Table 7.1.

To generate the relatively high amounts of light needed for this splitting and to extend the spectral range of the monitoring system into the UV-region, a **Laser-Driven Light Source** (LDLS, *Energetiq EQ-99X-FC*) was employed. The light source provides an emission spectrum from 190 nm up to 2500 nm, of which an effective spec-

Table 7.1: The spectral ranges and resolutions for the high-resolution broadband monitor.

Spectrometer no.	Spectral range (nm)	Resolution (nm)
1. (UV-range)	200 - 360	0.10-0.15
2. (UV-range)	305 - 410	0.10-0.15
3. (VIS-range)	400 - 540	0.10-0.18
4. (VIS-range)	530 - 650	0.10-0.18
5. (VIS-range)	640 - 735	0.10-0.18
6. (VIS-range)	735 - 915	0.20-0.28
7. (IR-range)	910 - 1060	0.20-0.28

trum from 240 nm up to 1050 nm can be used for monitoring. The limiting of the usable spectral range results from the limits of the applied spectrometers. Figure 7.4 shows the spectral intensity distribution of the LDLS.

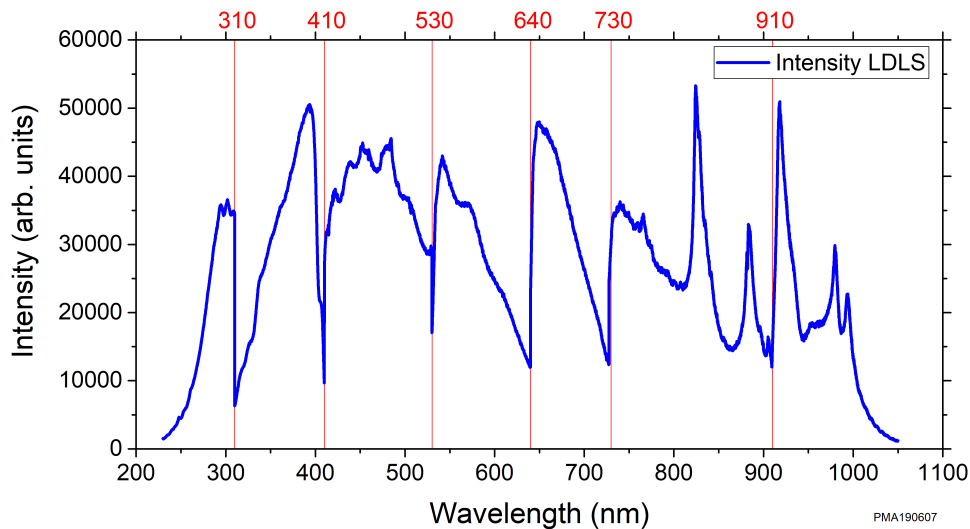


Figure 7.4: The spectral intensity distribution of the LDLS as measured by the HR-BBM. The transitions between the different spectrometers can be clearly observed and are marked by red lines.

7.3.2 Coating stability considerations

The simulations performed by the UNM for frequency tripling mirrors show that stability of 1% has to be achieved both for the refractive index of the employed materials as well as for the physical layer thicknesses to obtain designs with high-quality parameters [95]. Although the IBS coating process is qualitatively known to be very stable, its actual stability is hard to quantify. Therefore, over a period of several months, the results of the coating runs in the project were monitored, characterized, and evaluated systematically. During each coating run, the transmittance spectrum after each deposited layer was recorded with the HR-BBM, which made it possible to accurately calculate the material data for each individual coating run. This availability of material data makes a detailed view of the development of the refractive index of the coating materials possible. Figure 7.5 (a) shows the absolute values of the refractive index of the employed HfAlO-mixture. It can be observed, that the most significant changes in the refractive index can be correlated to cleaning or other mechanical maintenance of the coating chamber. For the production of frequency-tripling mirrors, however, the absolute refractive index is not critical. Instead, its stability from one coating run to the next is of interest, since this dictates if the design of the layer stack used in the last coating run is still valid for the next

one. This relative variation is presented in Figure 7.5 (b). The required accuracy of 1% is met by the majority of the coatings, and most of the points that exceed this value can be correlated to chamber maintenance.

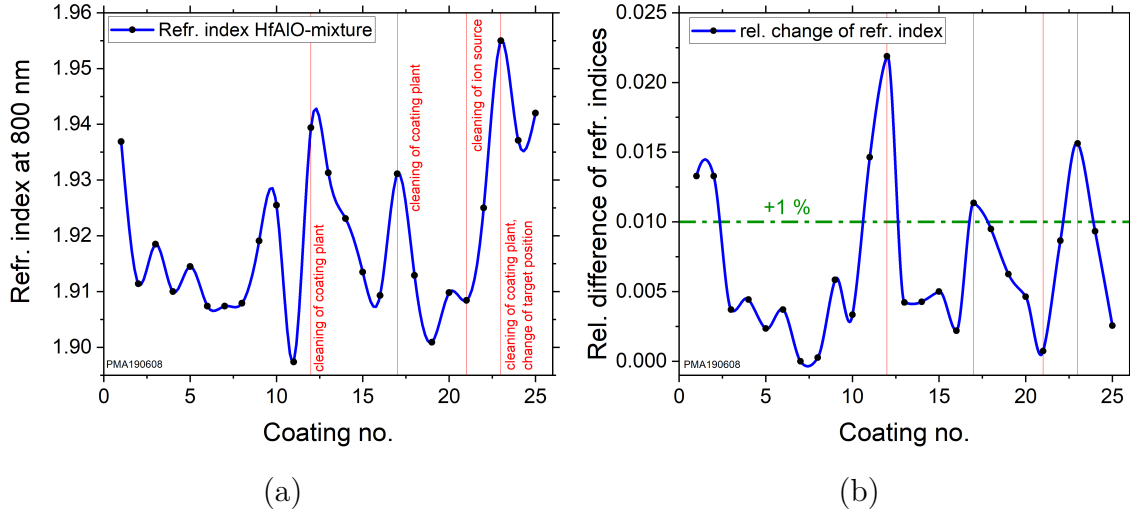


Figure 7.5: The variation of the refractive index of the employed HfAlO mixture over several coating runs. (a) depicts the variation of the absolute refractive index, with clear jumps visible where the coating machine or its components were cleaned or serviced. (b) shows the relative change from coating run to coating run. Most coatings stay below the 1% threshold, with those that exceed it mostly correlated to changes in the coating machine.

The available data after completion of each coating was then used for the production of the next coating run, subsequently improving the results with each run. The resulting accuracy for a 25-layer FTM is presented in Figure 7.6, together with the results of the same design, but manufactured before the continuous refitting of material parameters. A significant improvement of the layer thickness accuracy can be observed, with almost every layer of the design deposited after the process optimization featuring a thickness error below 1%.

Summarizing, the coating process presented in this section meets the requirements set by the UNM and should be suitable for the production of FTMs.

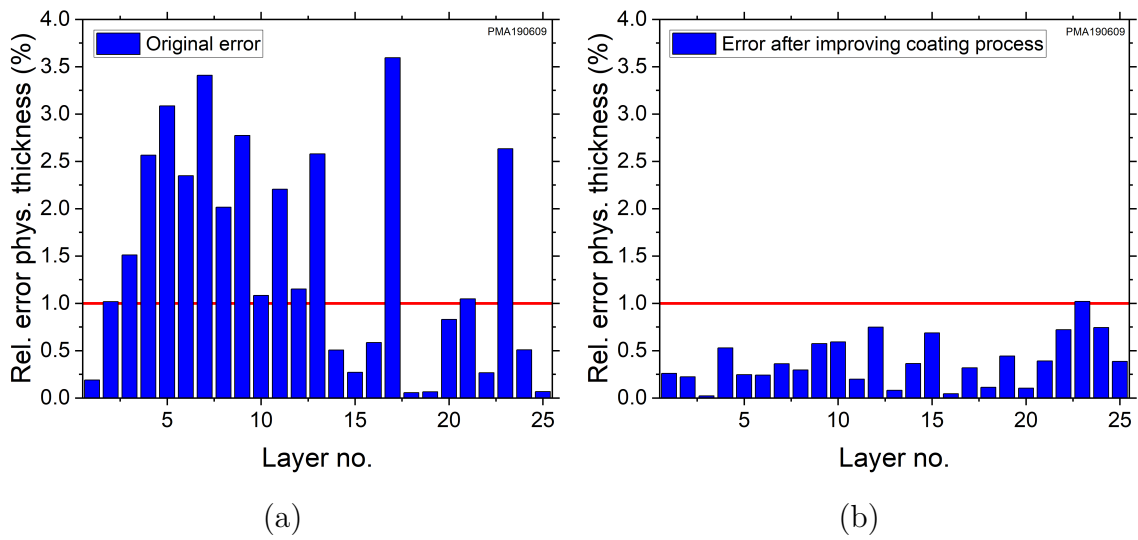


Figure 7.6: The relative error of layer thickness for every layer in a 25-layer FTM before and after process optimization. By continuously recording and evaluating the material data of the produced FTM, the layer accuracy could be improved to less than 1% in almost every layer.

8 Manufacturing and characterization of active materials

This chapter gives insight into the characterization of the previously identified active materials as well as their implementation of active materials in KBS-components.

8.1 Indium tin oxide

One of the active materials utilized in this thesis is Indium Tin Oxide (ITO), which is a transparent conductive oxide and falls into the category of **Epsilon-Near-Zero**-materials (ENZ-materials). The nonlinear properties of this material class are discussed in Chapter 3. To effectively apply ITO in optical switches, a parameter study was conducted to identify the best coating and annealing parameters. The results of this study were published in [96] during the work in this thesis and are summarized here.

8.1.1 Deposition process and thermal treatment

To test the properties of ITO, layers with a thickness of 315 nm were deposited on fused silica substrates with 25 mm in diameter and a thickness of 1 mm. The deposition was done using the coating machine presented in Section 7.2. For the ion source, a beam voltage of 1000 V with a beam current of 250 mA and an accelerator voltage of 300 V were chosen. The coating chamber was evacuated to a base pressure of 1×10^{-5} mbar. For the ion source and neutralizer, 14 sccm and 6 sccm argon were supplied as process gas. The target consisted of 90 % indium and 10 % tin. Due to this metallic nature of the target material, additional oxygen is required, to deposit oxidic layers in a reactive sputtering process. 9 sccm of oxygen were supplied, which was previously tested to deliver high optical transmittance with conductive layers. During the deposition process, the pressure in the chamber resulted to approximately 2×10^{-4} mbar. The deposition process was monitored by an optical BBM, which provides high accuracy for the thicknesses of the deposited layers. To observe the changes in the ITO layers, the samples were thermally treated after deposition. The

annealing was performed in ambient atmosphere in a temperature-controlled oven. Each annealing step was done for a duration of 10 h at temperatures between from 100 °C and 330 °C. The untreated samples were assigned a temperature of 60 °C, which is the approximate temperature during the coating process. As an example, the spectral transmission of an ITO-layer before and after annealing is illustrated in Figure 8.1 (a).

8.1.2 Characterization methods

The deposited layers were characterized for their relevant optical, electrical, and structural parameters. Different measurement procedures were applied for this characterization. An optical microscope (*Carl Zeiss AxioScope*) in differential interference contrast mode was used to get a visual impression of the samples' surface. A scanning electron microscope (*Quanta 400 FEG, Thermo Fisher scientific Inc., formerly FEI company*) was utilized to obtain a more detailed insight into the samples' surface structure. To check for any crystallization in the layers, **X-Ray Diffraction** (XRD) measurements were performed by the Institute for Inorganic Chemistry at the LUH. The XRD measurements were recorded with an Iso-DebyeFlex 3003 (*Stoe*) between 20° and 70° of 2θ , a step size of 0.05° and a time of 2 s per step with 40 kV and 30 mA. A *Perkin Elmer L19* spectrophotometer was used to measure the samples' spectral transmittance. The measurements were fitted using the *OptiChar* software [97]. To retrieve the thickness, refractive index, and extinction coefficient k of the deposited layers, the models for normal dispersion and tabulated k -values were applied. Figure 8.1 (b) depicts an example of the performed fits. Because the determination of the k -value only from the spectral transmittance is often unreliable, the absorption was measured with laser calorimetry at a wavelength of 1064 nm. The measurement procedure is detailed in [98, 99].

Another essential optical property of the samples is the **Laser Induced Damage Threshold** (LIDT). The LIDT was measured applying a *Coherent Monaco* laser system with a wavelength of 1030 nm, and a pulse duration that can be varied between 250 fs and 1000 fs. The laser spot on the samples was focused to an effective diameter of 66 μm , and the measurements were performed with a repetition rate of 10 kHz. The measurements were done following a 200.000-on-1 routine as per ISO21254-2 [100]. Figure 8.2 (a) depicts a complete schematic of the setup. During testing, each sample was irradiated at 126 sites. After the testing, the status of the irradiated spots was verified with optical DIC-microscopy. Figure 8.2 (b) shows examples of the damage morphology. With the statistics obtained from the measurements, the lifetime LIDT H_∞ for each layer was calculated [100].

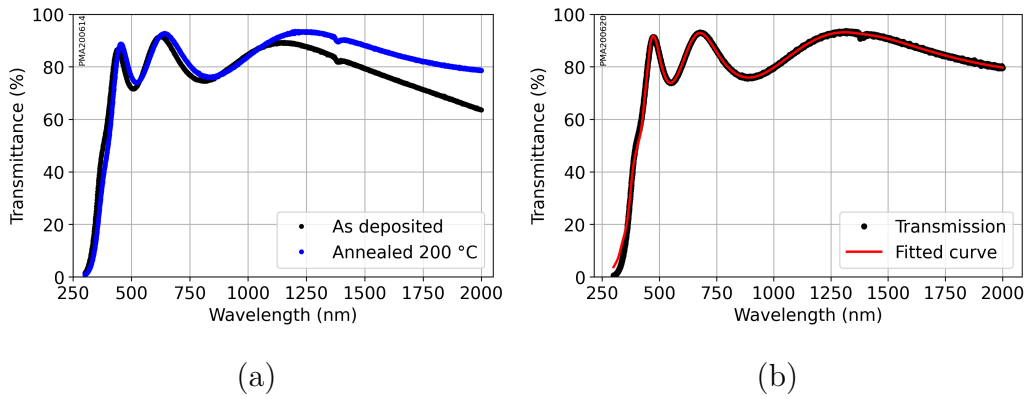


Figure 8.1: (a) Exemplary transmittance curves for an annealed (blue) and as-deposited (black) ITO single layer. The transmittance was fitted using commercially available software, the resulting fit is presented in (b). Graphs adapted from [96].

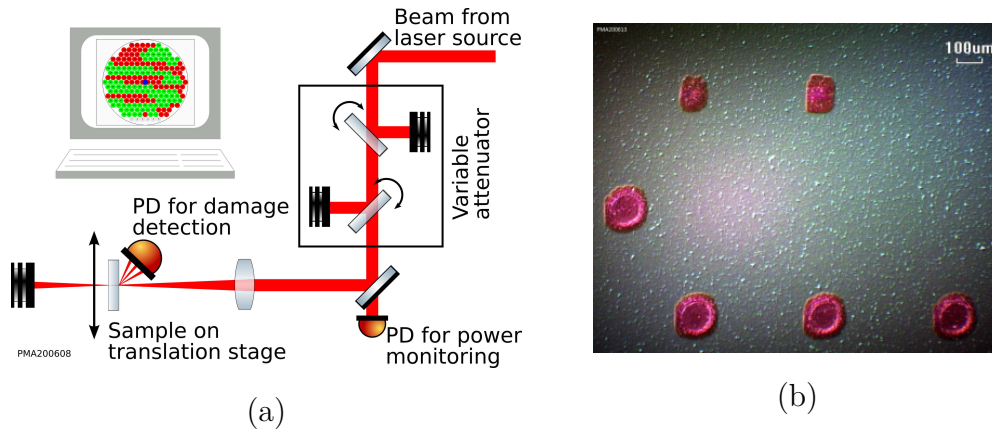


Figure 8.2: Schematic representation of the setup for LIDT measurements (a) and a microscopic picture of several destroyed spots after the LIDT test (b). Images from [96].

In addition to the optical and structural properties, the electrical properties of the ITO-layer are of interest since they depend on the free carriers of the material [101], which are also critical for the nonlinear properties of the material. Therefore, a four-terminal sensing method was utilized to reliably measure the material's resistance [102]. Four gold-coated, spring-loaded pins were applied as contacts to the coating surface. The pins are arranged in one row with a distance of 2.54 mm to each neighbor. The resistances R were recorded with a *Rigol DM3058E* digital multimeter.

Since the pins provide equidistant points of contact, the sheet resistance R_S of a layer can be directly calculated [103]:

$$R_S = \frac{\pi}{\ln(2)} R \quad (8.1)$$

The thickness d of the layers is known from the optical transmittance measurements, so the sheet resistance can be applied to calculate the material's resistivity:

$$\rho = d \cdot R_S = d \frac{\pi}{\ln(2)} R \quad (8.2)$$

8.1.3 Structural investigations

DIC-microscopy, as detailed in Section 8.1.2, gives insight into the changes in the optical properties of the ITO layers caused by the annealing process after deposition. Figure 8.3 shows four ITO samples after treatment at various temperatures. It must be noted that colors observed in DIC-microscopy are somewhat arbitrary, and the interpretation of pictures may be misleading. To compensate for this, colors and contrast in the images presented here were adjusted for better visibility of the layers' features. In consequence, the black color of the observed artifacts does not imply optical losses or opaqueness.

Figure 8.3 (a) shows the layer at 200 °C, where no clear changes in the structure can be observed. Figure 8.3 (b) shows the state after annealing at 250 °C, where the layer develops small black dots. These dots seem to expand further during annealing at 275 °C, as can be observed in Figure 8.3 (c). Figure 8.3 (d) shows the layers' state after annealing at 325 °C. The dark areas observed in the previous annealing steps seem to cover the surface. Similar changes have been observed in ITO by other investigations, where they were linked to the crystallization of ITO at elevated temperatures. [104, 105].

To investigate the suspected crystallization of the ITO layers in more detail, XRD-measurements were recorded for the different samples. Figure 8.4 presents the resulting diffraction curves. The results show a clear transition of the materials state from an amorphous to a crystalline state between 250 °C and 275 °C. The diffraction patterns fit a structure for ITO with small tin doping, which agrees with the expectations for the ITO layers under consideration[106]. Furthermore, the XRD-results match the observations of the microscopy, as the significant increase of the supposedly crystallized area at 275 °C observed in Figure 8.3 (c) can be correlated with the crystallization observed at the same temperature. The samples were inspected using the SEM introduced in Section 8.1.2 to explore the structural changes caused by the

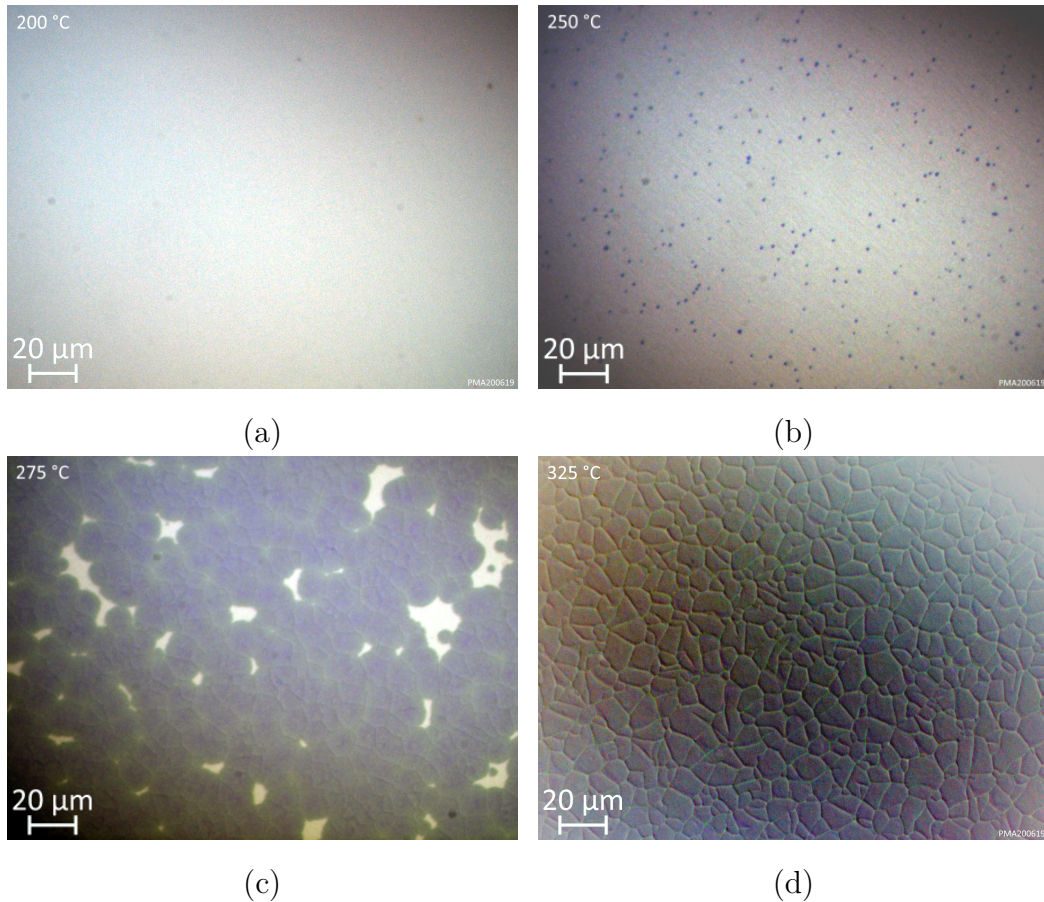


Figure 8.3: Analysis of ITO-samples annealed at different temperatures. (a) shows the layer after annealing at 200 °C. No significant features can be observed. After annealing at 250 °C, small black dots are visible (b). Annealing at 275 °C seems to cause growth of the black dots (c). After annealing at 325 °C, the surface is completely covered by the changed material (d). Images from [96].

different annealing temperatures in more detail. Since electron microscopy is less sensitive to changes in the optical properties of the samples, most changes observed with the DIC-microscope are not visible with this technique. Only the crack-like features observed on the sample annealed at 325 °C can also be seen in Figure 8.5. The size of the cracked areas is similar to that of the crystallization zones observed in Figure 8.3. It is therefore assumed that the cracked zones are identical to the areas observed with the optical microscope.

8.1.4 Index of refraction and extinction coefficient

The optical parameters usually of the highest significance for optical materials in any application are the index of refraction n and the extinction coefficient k . Therefore, a spectrophotometer in combination with suitable thin-film software was utilized to

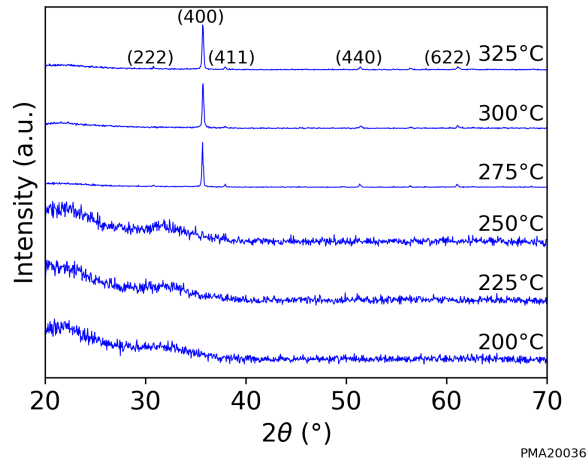


Figure 8.4: XRD-measurements for samples annealed at different temperatures. Between 250°C and 275°C a clear transition from an amorphous state to a crystalline one can be observed. Graph from [96].

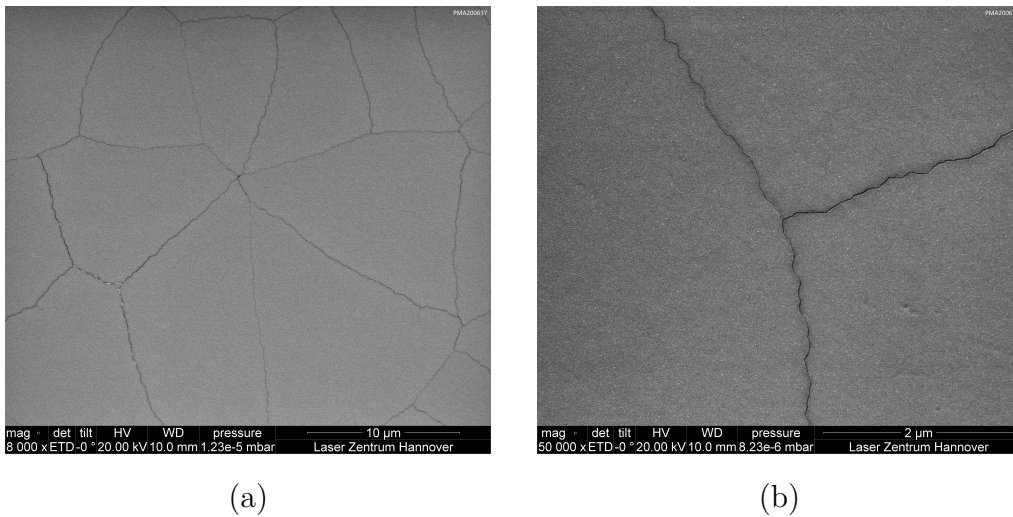


Figure 8.5: After annealing at higher temperatures, cracks in the ITO layers are visible. (a) illustrates the approximate size of the cracked areas, and (b) shows the cracks in detail. Images from [96].

measure the refractive index for the thermally treated ITO layers. The measurement of the k -value from transmission measurements alone often is unreliable. Therefore, laser calorimetric measurements were employed to measure the extinction in the ITO layers more accurately. Figure 8.6 depicts the results of these measurements for the different annealing temperatures. A corresponding behavior can be observed for the two optical parameters over the temperature range. At lower annealing temperatures, the refractive index of the layers increases while the absorption decreases. A maximum of approximately 2 for the refractive index and a minimum of approxi-

mately 1.2×10^{-3} for the k-value reaches are reached at a temperature of 200 °C. At higher annealing temperatures, the refractive index decreases, and the absorption increases due to the crystallization of the layers at temperatures up to 275 °C. At 300 °C, further annealing causes another decrease in absorption and an increase in the refractive index before the breaking of the layers at 330 °C reverses this trend.

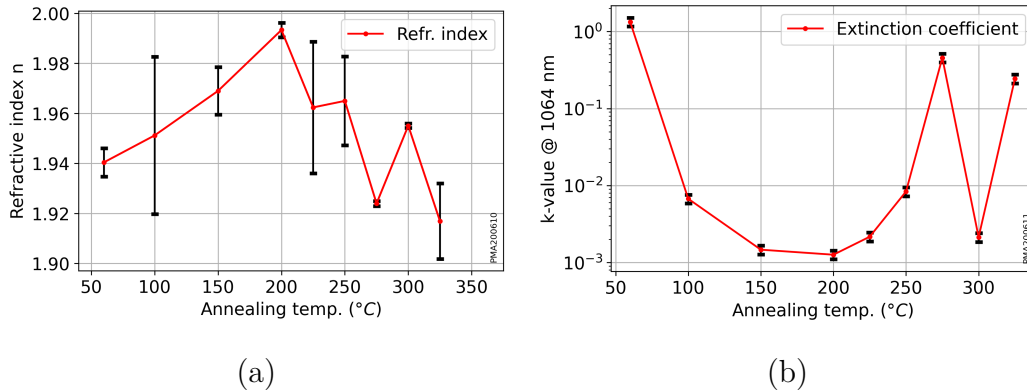


Figure 8.6: Index of refraction n and k-value for the thermally treated ITO layers. The refractive index was determined for the intended application wavelength of 1035 nm. The absorption measurements were performed at 1064 nm and the absolute absorption values converted to the k-value. Graphs from [96].

8.1.5 Electrical properties

In many applications, ITO is mainly used for its transparency in combination with its electrical conductivity and not for its ENZ-properties. In these cases, the electrical properties of ITO are of main interest. In addition, the electrical properties are related to the material's free carriers, which play a significant part in its nonlinear properties. Consequently, the electrical resistivity of the thermally treated ITO layers was measured as specified in Section 8.1.2. Figure 8.7 presents the resulting resistivities for the different annealing temperatures. After the deposition process, and without thermal annealing, the samples feature a low resistivity. Annealing at temperatures up to 200 °C causes this resistivity to increase by two orders of magnitude. This increase is less pronounced for annealing at temperatures between 200 °C and 250 °C. Annealing at 275 °C causes resistivity to decrease rapidly, and annealing at higher temperatures again increases resistivity. The temperature dependency of the electrical resistivity and the optical properties can be understood when the mechanisms that cause the unique electric properties of ITO are considered. The properties of ITO are the result of its two metals and the included oxygen. When oxygen vacancies are present in In_2O_3 , two free carriers are created, which decrease

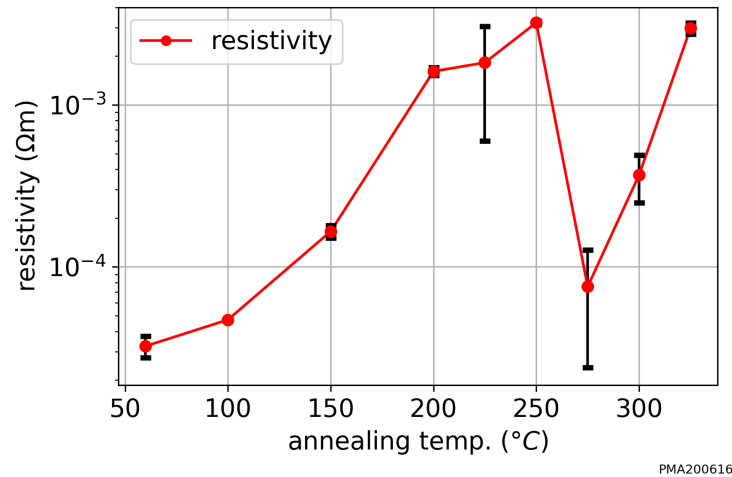


Figure 8.7: The electrical resistivity of thermally treated ITO layers. For temperatures up to 200 °C, the resistivity increases quickly. Between 200 °C and 250 °C, the change is more slowly, and at 275 °C, the resistivity decreases rapidly. At higher temperatures, the resistivity increases again. Graphs from [96].

resistivity. Similarly, when Sn-atoms are integrated into the crystal grid of In_2O_3 , four free carriers are created [107]. However, it was shown that the included Sn-atoms do not contribute free carriers and therefore do not lower resistivity when the ITO is in an amorphous state [108]. After deposition, the only source of free carriers are the oxygen vacancies, which can be controlled by the amount of oxygen supplied during deposition. Annealing in ambient atmosphere, however, promotes oxidization of the layers, which reduces the number of vacancies and therefore increases resistivity. This trend continues with increasing annealing temperatures until 250 °C is reached. Here, as shown in Figure 8.3, the first signs of crystallization can be observed. This leads to the inclusion of Sn-atoms, increasing the number of free carriers and decreasing the material's resistivity. This initially slows the growth of the resistivity caused by oxidation between 200 °C and 250 °C and completely reverses the trend during the transition from 250 °C to 275 °C, as observed in Figure 8.7. The increase in resistivity at higher temperatures is attributed to the material cracking, as observed in Figure 8.5, probably due to thermally induced stress between the substrate and the layer.

8.1.6 Laser-induced damage threshold

The intensities typically utilized in nonlinear optical applications are very high to maximize the nonlinear effects. Consequently, the maximum intensity a material can withstand must be considered when high nonlinear effect strengths are to be

achieved. Therefore, the setup described in Section 8.1.2 was employed to measure the LIDT of the ITO layers for the different thermal treatments. The results for the respective temperatures are depicted in Figure 8.8.

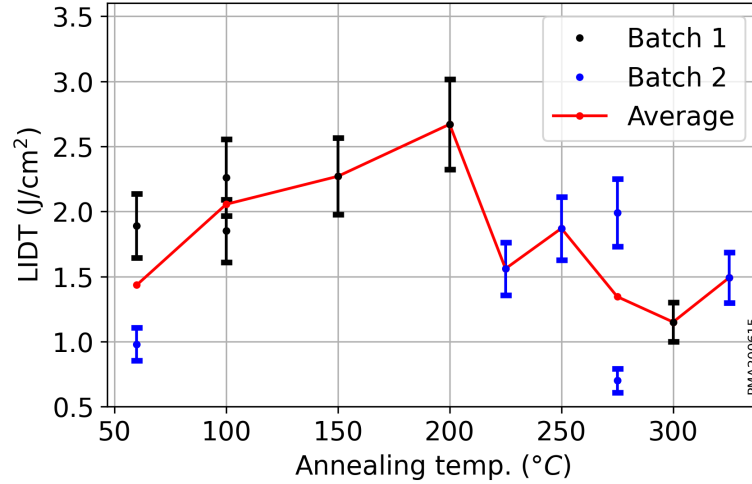


Figure 8.8: The LIDT of thermally treated ITO. The LIDT increases for annealing temperatures up to 200 °C. Annealing at higher temperatures decreases the LIDT again. Graph from [96].

The damage threshold for samples that were not thermally treated is measured at 1.4 J/cm². Annealing up to temperatures of 200 °C increases the LIDT to 2.7 J/cm². If the temperature is further increased, the LIDT reduces again, reaching 1.2 J/cm² at 300 °C. Figure 8.9 shows the differing damage morphologies of the layers after annealing. In their initial state and for annealing at temperatures of up to 250 °C, the damage morphology is typical for damages in the regime of ultrashort pulsed lasers. Between 250 °C and 275 °C, a clear transition in the damage behavior can be observed. The damage at 275 °C seems to show a stronger influence of thermal effects. When annealed at higher temperatures, the morphology returns to its initial state.

These measurements agree with the results presented in the previous section. It can be assumed that the LIDT correlates negatively with the free carriers present in the layer material. The measurements of the optical losses and the electrical conductivity indicate a higher density of free carriers directly after the coating process and at annealing temperatures around 275 °C, where the tin is incorporated. Therefore, the low initial LIDT, the increase observed for annealing at temperatures up until 200 °C, and the decrease afterward can be explained. The slight increase at higher temperatures may be explained by the reduction of free carriers due to continued oxidation of the In₂O₃. However, with the observed cracking of the layers at these temperatures, an interpretation cannot be easily made.

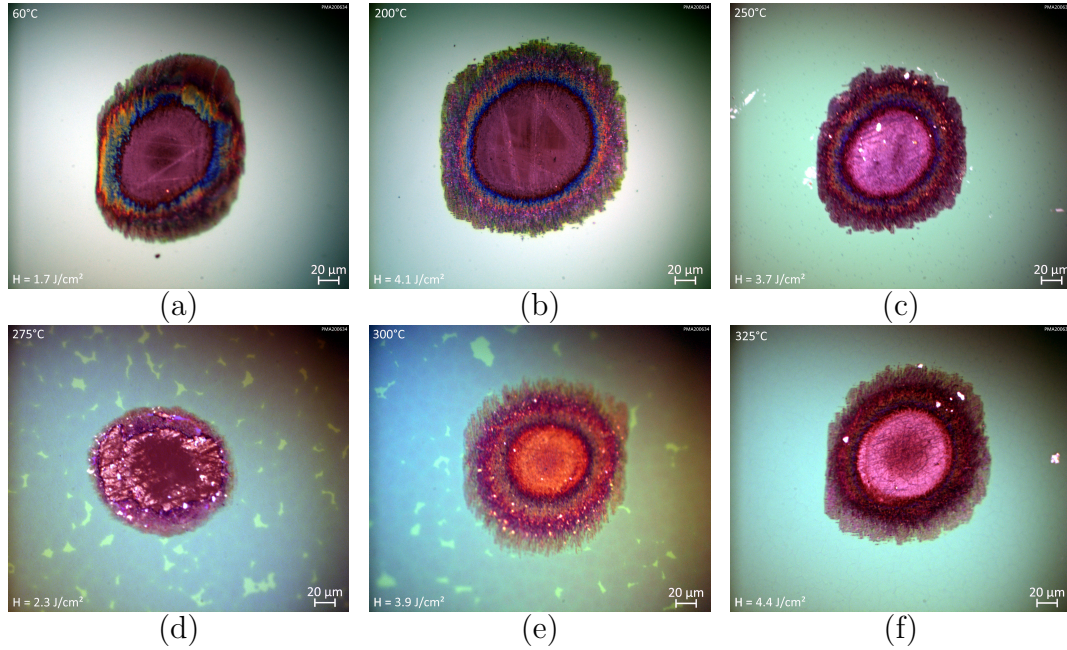


Figure 8.9: Damage morphologies for the different annealing temperatures. The temperature is 60 °C for (a), 200 °C for (b), 250 °C for (c), 275 °C for (d), 300 °C for (e), and 325 °C for (f). At 275 °C, a change in morphology due to the crystallization of the coating can be observed. Pictures from [96].

8.2 Gallium arsenide

The second active material applied in this thesis is gallium arsenide (GaAs). As a semiconductor material, it features a very high nonlinear refractive index, as explained in more detail in Section 3.3. This section explains the working principle and manufacturing of KBS based on GaAs as active material.

8.2.1 The concept of GaAs-KBS

Semiconductor materials can feature extremely high nonlinear refractive indices, similar to ENZ-materials. The strength of this nonlinear interaction depends on the relation between the material's band gap energy and the energy of the incident photons (see also 3.3). Under this criterion, Gallium Arsenide (GaAs) with its band gap energy of 1.42 eV is well suited for application as active material in KBS-switches intended for wavelengths around 1 μm, which equal photon energies of 1.24 eV.

GaAs is frequently used in optical applications for the infrared range [109], and even more prevalent as a superior semiconductor material in high-end electronics, such as highly efficient solar cells [110] and light emitting diodes [111]. In contrast to ITO and similar materials, however, the deposition of GaAs is more challenging due to the related safety hazards. The arsenic contained in GaAs can form strongly

toxic and carcinogenic oxides when the bond to gallium is broken [112]. All classical PVD processes create particles of the coating material as a byproduct, and the IBS coating processes used in this thesis are almost certain to split the molecular bond of GaAs during sputtering of the target material.

The direct deposition of GaAs is, therefore, not topic of this thesis, and alternative approaches were considered. To still achieve a component similar to the KBS designs introduced in Section 5.1, the principle was transferred to substrate free-optics. Since the active material GaAs has to form a central spacer layer for the switching to work as intended, the coating was deposited in two batches on both sides of special, very thin GaAs wafers. The principle is illustrated in Figure 8.10. In this case, the finished component is even closer to a Fabry-Perot-resonator than the KBS-concept when it is realized in a single thin film coating. The bandwidth of the pass-bands is determined mainly by the thickness of the GaAs wafer but can be influenced by the reflective properties of the coatings on both wafer surfaces. Figure 8.11 shows an example of this. The spectral transmittance of a GaAs-Wafer is plotted, once with simple QWOT-stack-mirrors in (a) and once with coatings tuned to achieve a higher bandwidth of approximately 0.4 nm.



Figure 8.10: The schematic representation of a GaAs-KBS. Instead of a single coating on an optical substrate, a GaAs-wafer functions as the central spacer and the coating is deposited on both wafer surfaces.

8.2.2 Manufacturing of GaAs-KBS

The GaAs chips chosen for this application are reclaimed wafers available from the semiconductor industry. The reclaiming of these wafers includes additional polishing steps, which reduces their overall thickness. The wafers are only available in relatively large sizes, which is why the chips used for the actual coating process were smaller rectangles of approximately 10 mm by 5 mm that were created by breaking the larger wafers. The coating process is performed with the same machine that is used to manufacture the KBS based on ITO and which is featured in Section 7.2. SiO_2 and Ta_2O_5 were chosen as coating materials. Due to the substrate-free

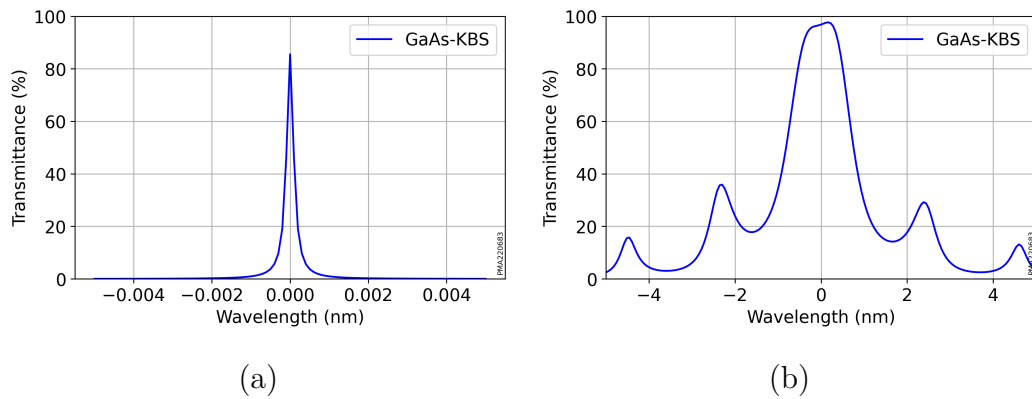


Figure 8.11: The transmission of a GaAs-KBS based on simple QWOT-stack mirrors (a) and with altered mirrors for increased bandwidth (b). Due to the relatively high thickness of the central spacer, the bandwidth in (a) is too small for the application with pulsed lasers. Changing the design of the outer mirror coatings can mitigate this to some degree.

approach of the GaAs-KBS, the manufacturing process consists of two separate coatings, one for each side of the GaAs chip. During deposition, the chips were glued to glass-carrier substrates with vacuum-capable poly amide tape. An example of a GaAs-chip after the coating process still glued to its glass-carrier substrate is shown in Figure 8.12.

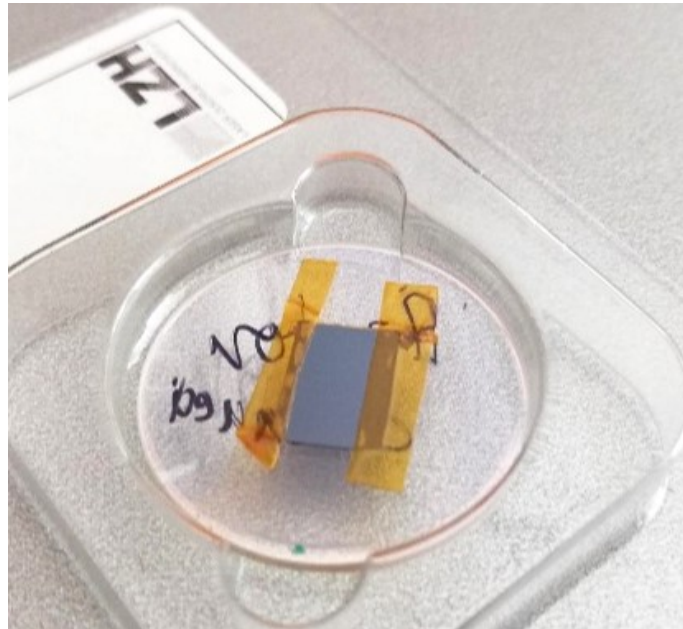


Figure 8.12: A GaAs-KBS after the deposition process still glued to its glass-carrier substrate. After coating the first side of the GaAs chip, the tape is cut, and the chip is turned around for the coating of the second side.

9 Experimental setups

This chapter introduces the different experimental setups and methods employed to characterize the produced optical components for their intended nonlinear optical properties.

9.1 Characterization of frequency tripling mirrors

First measurements of FTMs yielded efficiencies of about 1 %, which is greatly improved over a normal high reflective mirror, but still below the values expected from the simulations, which were 5 % and higher [80]. Therefore, in a first step, the accuracy of the deposition process was characterized and improved as described in Section 7.3. In parallel, the physical mechanisms causing the low conversion efficiency were investigated in more detail. To undertake these investigations and measure the conversion efficiency of the samples deposited with the improved process, an optical experiment was set up at the UNM, and measurements were done in cooperation in the frame of this thesis. A schematic of the experimental setup is depicted in Figure 9.1.

The laser source used for the investigations is an amplified titanium-doped sapphire laser with a central wavelength of 815 nm and a pulse duration of 42 fs. The optical laser spectrum is depicted in Figure 9.2. The laser system features a repetition frequency of 1 kHz and an average power of 2.3 W, which equals a pulse energy of 2.3 mJ. The spectral intensity distribution of the laser system features an FWHM-bandwidth of 33 nm. To estimate the influence of this bandwidth on the TH-signal, the fundamental spectrum is recorded by an *ANDOR Shamrock* spectrometer utilizing a matching *ANDOR Newton* CCD-camera. An additional filter can be inserted into the beamline, which limits the bandwidth to a Gaussian distribution (see Figure 9.3) with an FWHM-width of 14.11 nm.

The third harmonic generated in reflection of the FTM is separated from the fundamental using a dichroic mirror. The spectral intensity distribution of the generated TH is then recorded by an *Avaspec-2048-USB* UV-spectrometer. At the third harmonic wavelength, the spectrometer features a resolution of 0.14 nm and is sensitive

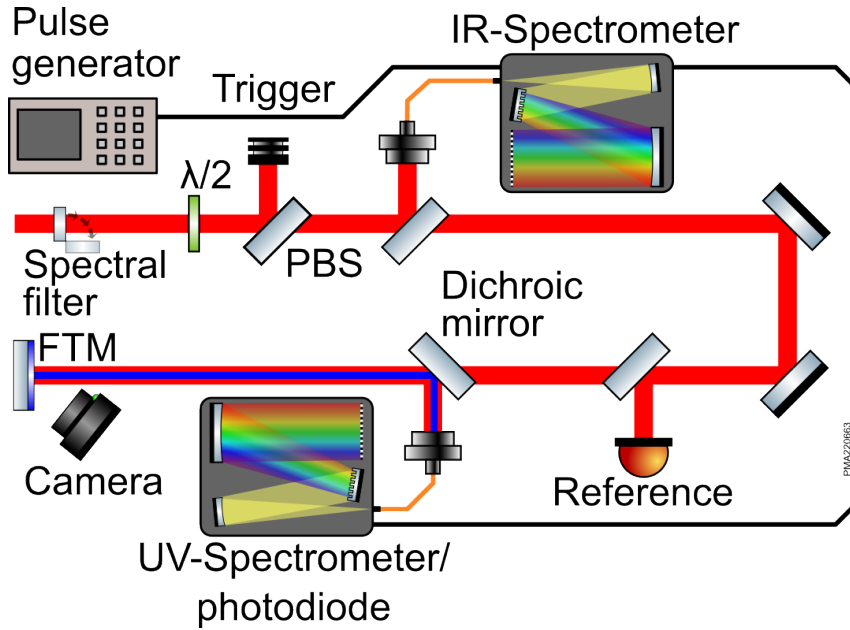


Figure 9.1: The setup applied for the characterization of frequency tripling mirrors. The laser is attenuated by a combination of $\lambda/2$ -waveplate and Polarizing Beam Splitter (PBS). The spectrum of the fundamental wave is measured by a spectrometer for the infrared range, referenced by a photodiode, and propagates onto the FTM. The third harmonic is generated in reflection and separated by a dichroic mirror, which reflects it into a spectrometer for the ultraviolet range. The spectrometer is exchanged with a photodiode to measure the power of the generated third harmonic. A camera is used to monitor the surface of the FTM for damage. The laser and the spectrometers are triggered by a pulse generator.

between approximately 200 nm and 450 nm. Alternatively, the power of the third harmonic can be measured by a calibrated photodiode to measure conversion efficiency. A camera is used to monitor the surface of the FTM for damage. The laser and spectrometers are triggered by a pulse generator, which enables irradiation of the FTM with pulse trains or single pulses.

9.2 Measurement of the nonlinear refractive index

For the manufacturing of KBS-samples, the nonlinear refractive index of the applied coating materials is of high significance. This is both true for the typical coating materials used in the mirror coatings and the active materials integrated into the coating design to perform the switching. To measure this critical parameter, an interferometric measurement method was developed in [113] and further refined in this thesis. The experiment is based on the z-scan method, which is a well-established method for measuring the strength of the optical Kerr effect in transparent samples

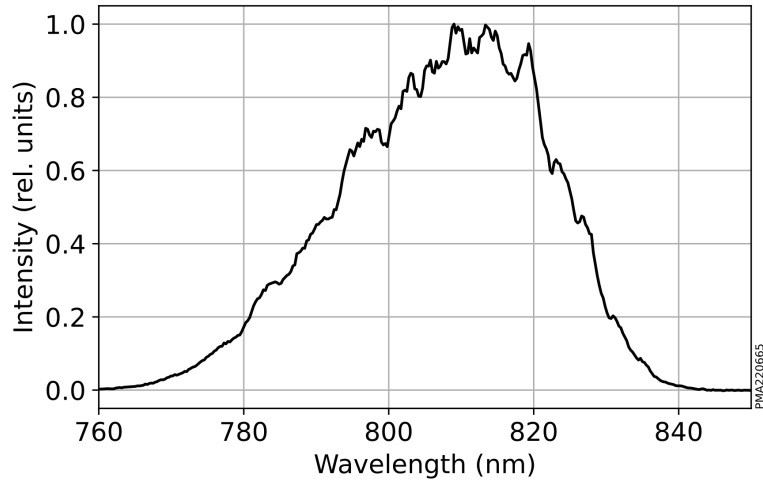


Figure 9.2: The spectral intensity distribution of the laser system used for characterization of frequency tripling mirrors.

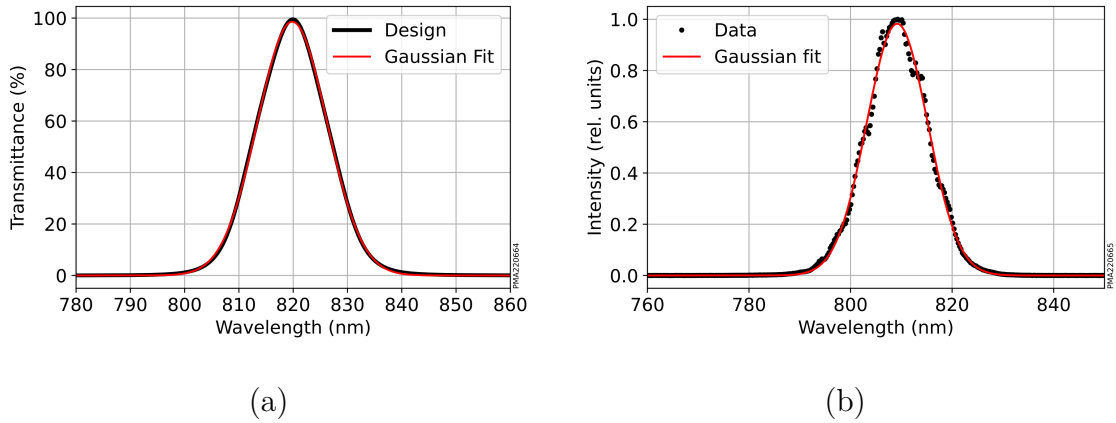


Figure 9.3: (a) The transmittance of the utilized spectral filter. The transmittance profile was designed to approximate a Gaussian spectral shape as closely as possible. The fitting of a Gaussian distribution (red) results in an FWHM-width of 15.04 nm. (b) The laser spectrum after filtering with the manufactured coating. Again, a Gaussian distribution is fitted, yielding an FWHM-width of 14.11 nm. The filter was angled slightly to achieve maximum transmission of the laser power, which causes a slight shift of its central wavelength.

[114]. But instead of monitoring the change in beam diameter, the interferometric implementation allows the monitoring of the wavefront of the beam transmitted through the sample under test. A schematic layout of the experimental setup is depicted in Figure 9.4. In contrast to the classic z-scan, approach, the interferometric method is insensitive to nonlinear absorption and can be more sensitive. This allows the measurement of the nonlinear refractive index of thin film materials as was shown in [115, 116].

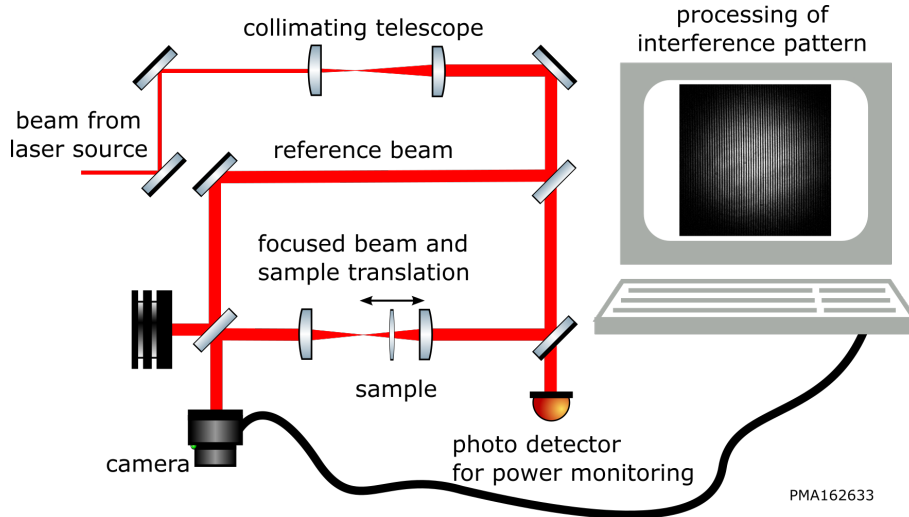


Figure 9.4: The interferometric setup for the determination of the nonlinear refractive index. The incoming laser beam is split into a high-power sample beam and a low-power reference beam. The sample beam is focused on the sample under test and re-collimated afterwards. The reference and sample beam are then superimposed on a CMOS camera sensor and the interferogram is recorded for later evaluation. Image from [113].

The information about the wavefront curvature can be retrieved from the interferogram by superimposing the two beams under an angle. When the two wavefronts interfere under the selected angle, a stripe pattern is created, which allows the separation of the wavefront information from the overall brightness gradients and other irregularities in the beam profile. The separation is achieved by calculating a **F**ast **F**ourier **T**ransformation (FFT) of the recorded interferogram. When a suitable angle and, therefore, stripe frequency is chosen, the stripe pattern appears as clearly separated maxima in the 2D-spectrum of the interferogram.

An exemplary interferogram together with the corresponding 2D-spectrum is depicted in Figure 9.5. In Figure 9.5 (a), a typical stripe pattern created by interference of the two beams, in this case vertical, can be observed. Figure 9.5 (b) shows the corresponding 2D-spectrum calculated with the FFT. The vertical stripes create symmetric maxima along the x-axis of the spectrum. When one of these maxima is isolated, shifted back to the origin of the spectrum, and an inverse FFT is performed, the 2D-wavefront information is retrieved. An example of the retrieved 2D-information is presented in Figure 9.6. The absolute calibration of the stripe frequencies and coordinates of the wavefront information is retrieved from the size of the camera's pixels. The camera model employed in the measurements (*Basler pulse - puA1600-60um*) features square pixels with a size of $4.5\ \mu\text{m}$ and a resolution of $1600\ \text{px} \times 1200\ \text{px}$.

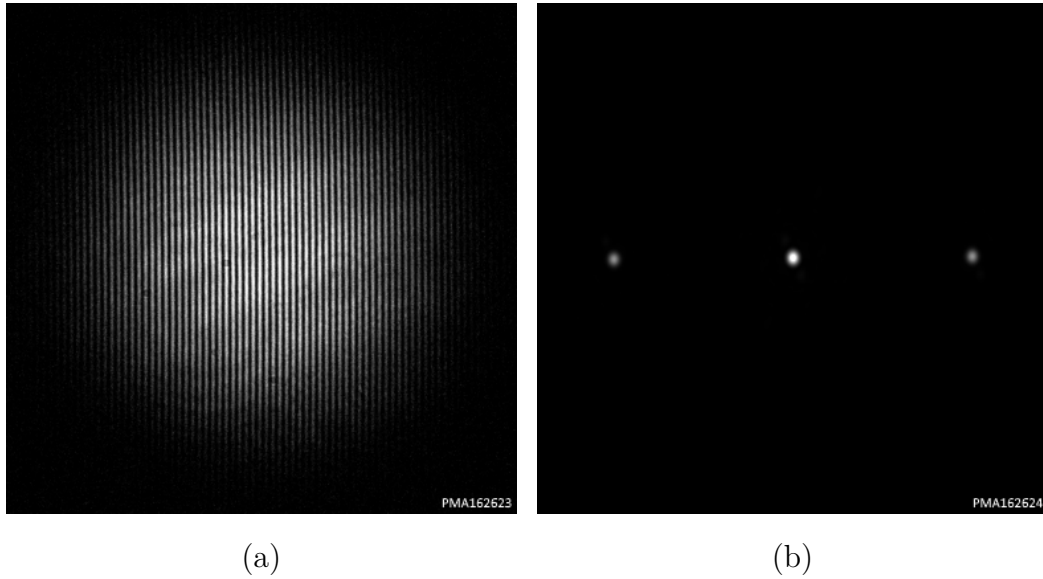


Figure 9.5: An exemplary interferogram and its FFT. In (a), a typical interferogram created by superposition of reference and sample beam is shown. The stripe pattern (in this instance, vertically), can be clearly seen. (b) shows the corresponding 2D-spectrum calculated utilizing the FFT. The vertical stripe pattern creates two symmetric maxima along the x-axis. Image from [113].

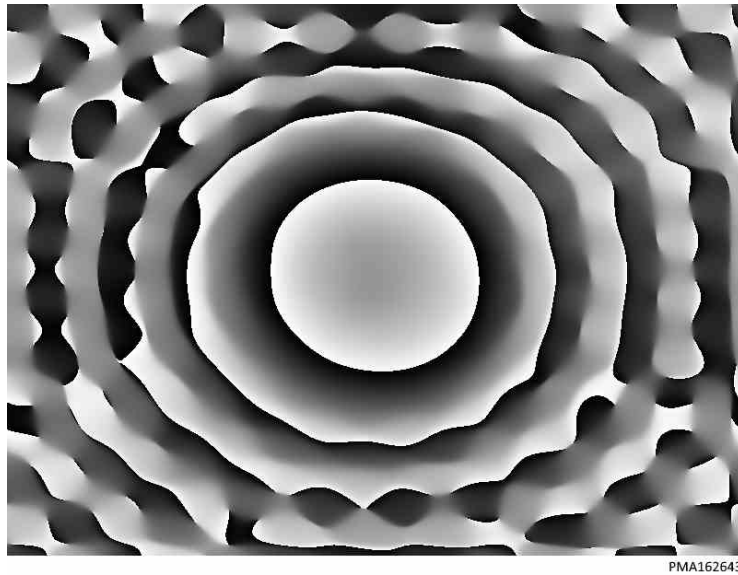


Figure 9.6: The 2D-phase distribution retrieved from the 2D-spectrum of the recorded interferogram. A circular phase pattern with 2π -jumps can be observed. Image from [113].

This 2D-information has to be unwrapped to calculate the radius of curvature of the sample beams wavefront. 2D-phase unwrapping is not easily achieved and may be impossible. Therefore, a simpler 1-D approach was chosen. For evaluation, the values of the 2D-phase pattern are read along lines through the center of the pattern.

Along these lines, a simple 1D-compensation of the 2π jumps can be performed. An example of a line profile with phase jumps and with compensated jumps is presented in Figure 9.7. A circle can then be fitted to the compensated profile to obtain the radius of curvature of the recorded wavefront.

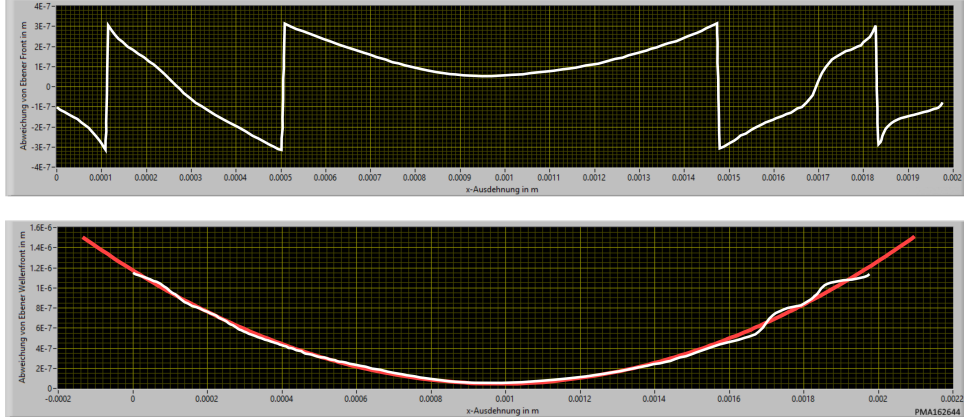


Figure 9.7: From the 2D-phase distribution, line profiles through the center of the waveform can be retrieved (upper image). The phase jumps present in these profiles can be compensated easily (lower image). A fitted function (red) is used to calculate the radius of curvature of the recorded wavefront. Image from [113].

The method for the retrieval of the nonlinear refractive index is explained in more detail in [116], so only a brief overview is given here. In principle, the retrieved radius of curvature is compared to a theoretical model based on the optical ray transfer matrix formalism as described in [117]. The experimental setup is modeled using this formalism, with a special approximation for thick samples applied [118]. The experimental parameters of the setup are transferred into the model, and the curve retrieved from the measurement is fitted with the nonlinear refractive index of the sample as free parameter. An example of a measurement and the fitted curve is presented in Figure 9.8. The measurement results are in good agreement with the curvatures retrieved from the matrix calculations. The retrieved value of n_2 at the laser wavelength of 1064 nm is $7.1 \times 10^{-16} \text{ W/cm}^2$, which compares well with values from literature, which are $6.5 \times 10^{-16} \text{ W/cm}^2$ [119] and are $7.7 \times 10^{-16} \text{ W/cm}^2$ [120].

9.3 Measurement of optical switching

For the validation of the simulated and deposited Kerr-band-switches, an experiment is necessary. At low intensities, a KBS should show maximum transmittance and a reflectance of almost 0%, if adjusted correctly. When the laser intensity is

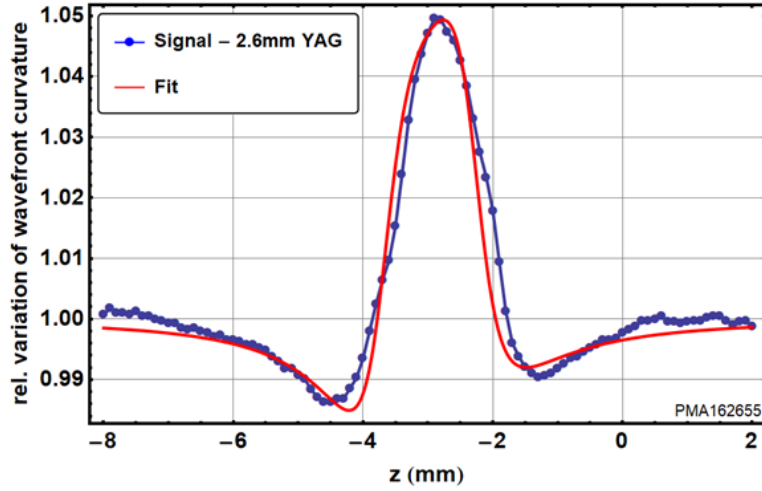


Figure 9.8: An exemplary measurement of the nonlinear refractive index for a YAG-crystal with a thickness of 2.6 mm. The blue dots represent the curvature values recorded in the interferometer, and the red curve is the model fitted with the n_2 of YAG as free parameter. The resulting value for n_2 is $7.1 \times 10^{-16} \text{ W/cm}^2$. Image from [113].

increased, the pass-band shifts to longer wavelengths and transmittance decreases. Simultaneously, this causes an increase in reflectance since the laser wavelength is now in a reflective region of the KBS-spectrum. Therefore, the optical experiment should monitor transmittance and reflectance, while the laser intensity can be continuously varied.

The setup chosen for this task is depicted in Figure 9.9. The radiation incoming from the laser source is attenuated by a combination of a $\lambda/2$ -waveplate and a polarising beamsplitter. The remaining s-polarized light is then sampled by an optical substrate with an anti-reflective coating on one side. Afterwards, the laser radiation interacts with the KBS, and both reflectance and transmittance are recorded by photodiodes. The angle of incidence on the KBS has to be chosen carefully to achieve maximum transmittance at low intensities so that a good alignment of laser wavelength and the KBS's band of transmission is achieved. To achieve absolute measurements of reflectance and transmittance, a 100 %-reference is necessary for both properties. For the transmittance, a simple measurement without sample can be recorded and used as 100 %-baseline. For reflectance, a dielectric mirror with suitably high reflectivity ($R > 99.99$) can be employed. Since the laser wavelength is well-defined in these measurements, the bandwidth of typical dielectric mirrors is sufficient, and the error related to employing this reference is only small.

The setup can, in principle, be used with any laser source. The intensities necessary to produce a meaningful optical Kerr effect require short pulse durations. Therefore,

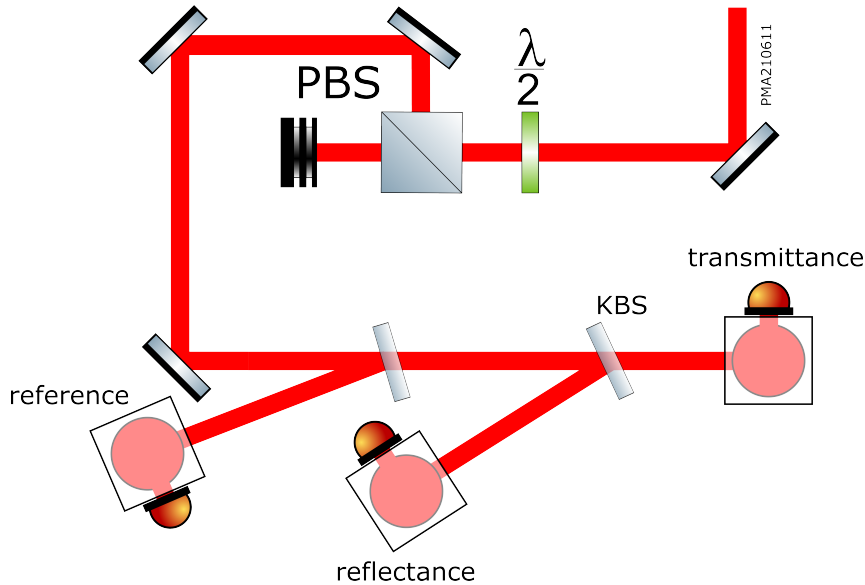


Figure 9.9: The experimental setup for measurement of the optical switching. The intensity of the incoming laser beam is attenuated by a $\lambda/2$ -waveplate and a polarising beamsplitter. The intensity of the laser beam is sampled by an optical substrate with a one-sided anti-reflective coating. The angle of the KBS has to be adjusted precisely to achieve maximum transmittance at low intensities to align the band of transmission with the laser wavelength. Transmittance and reflectance are then recorded by photodiodes.

only laser sources in the few picosecond to femtosecond regime are suited for the investigations. The measurements done in this thesis were recorded using a *TruMicro 5050* picosecond laser system by *Trumpf*. The system is capable of delivering pulses with a duration of 10 ps with a pulse energy of up to 250 μJ . The system can deliver average powers of up to 50 W at repetition rates of up to 200 kHz. The laser wavelength is 1030 nm. The spectral intensity distribution of the laser system is depicted in Figure 9.10.

During measurements, a certain number of pulses is recorded by a digital oscilloscope (*Siglent SDS1104X-E*) and evaluated with a LabVIEW program developed in this work. Using the trigger signal, the maximum voltage of the individual pulses is detected and saved. An example of the recorded signals is depicted in Figure 9.11. The three different signals for the reference (Ref), transmittance (T), and reflectance (R) are clearly visible. By rotating the waveplate, the intensity on the KBS can be varied. Since a $\lambda/2$ -plate is used, for each angle θ that the plate is rotated, the polarization of the transmitted laser beam is rotated by 2θ . For the presented measurements, the wave plate was rotated in small steps up to a total angle of 90° . In the initial position, the p-polarized laser beam is not influenced by the waveplate, and nothing is reflected onto the KBS. When the waveplate reaches

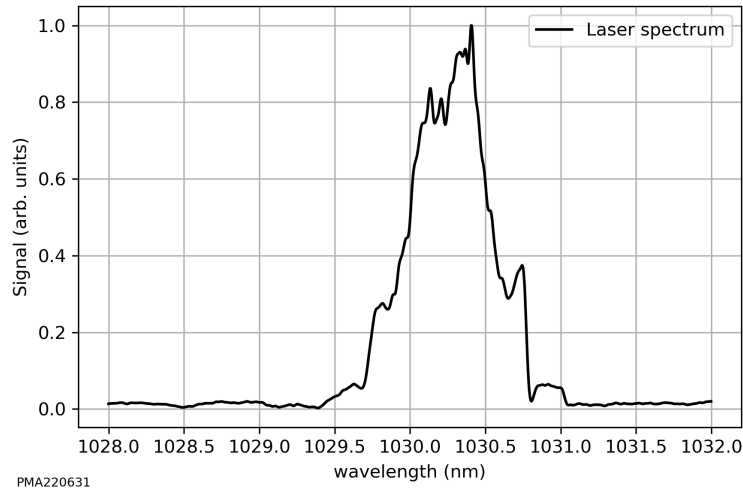


Figure 9.10: The spectral intensity distribution of the TruLase 5050 laser system. The plot is centered around 1030 nm. It can be observed that the laser spectrum is centered around a slightly higher wavelength. The FWHM-bandwidth is 0.5 nm, which limits the theoretically possible shortest pulse duration to 2.2 ps.

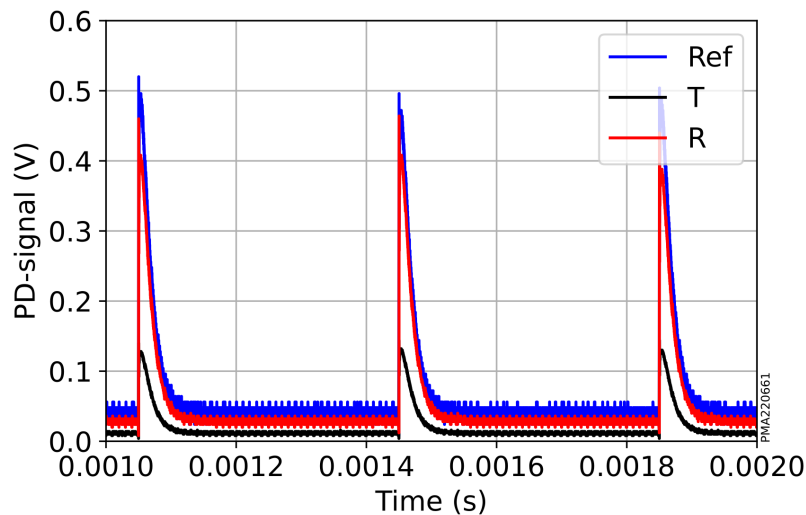


Figure 9.11: The three signals recorded during a measurement. The graph shows three laser pulses as seen by the photodiodes recording the reference (Ref), transmittance (T), and reflectance (R).

45°, the polarization of the laser beam is rotated by 90°, and the intensity on the KBS reaches its maximum. Further rotation of the waveplate towards 90° returns the polarization back to its initial state, and the intensity on the KBS is reduced again. Figure 9.12 shows the power during a measurement cycle as measured by the reference diode, which matches the expected behavior, illustrated by a fitted $\sin^2(\theta)$ -function. To monitor the power incident on a KBS, an absolute calibration

of the reference diode's signal is necessary. The calibration is performed by substituting the KBS-sample with an optical power meter and recording the power values together with the signal of the reference diode. The results of an exemplary calibration are depicted in Figure 9.13. A very linear behavior between incident power and the signal of the reference diode can be observed. Each set of calibration data is fitted with a linear function that is used to calculate power during the corresponding measurements.

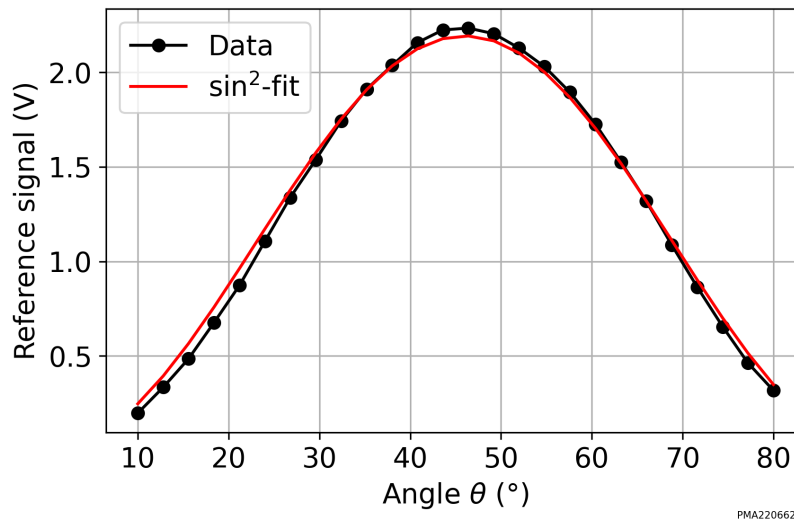


Figure 9.12: The signal as recorded by the reference diode over the angle of the $\lambda/2$ -plate. The signal starts at a minimum and reaches a maximum at approximately 45° , where the polarization is rotated completely to s-polarized. A $\sin^2(\theta)$ -fit is added to check if the behavior matches the theoretical expectation.

9.3.1 LIDT measurement

In addition to the characterization of the switching behavior, the laser-induced damage threshold can be determined utilizing the same laser system. To determine the LIDT, the setup depicted in Figure 9.9 is augmented as shown in Figure 9.14. The KBS-sample is irradiated with the intensity set by the combination of waveplate and polarizing beamsplitter. The power during irradiation is monitored by a reference-photodiode. The measurements are performed at a repetition frequency of 2.5 kHz. In accordance with ISO 21254 [100], a 20.000-on-1 measurement was performed. The scattering that occurs in case of surface damage is recorded and used as damage criterion. After irradiation, the damaged spots on the sample's surface are investigated with a *Zeiss AxioImager.M2*.

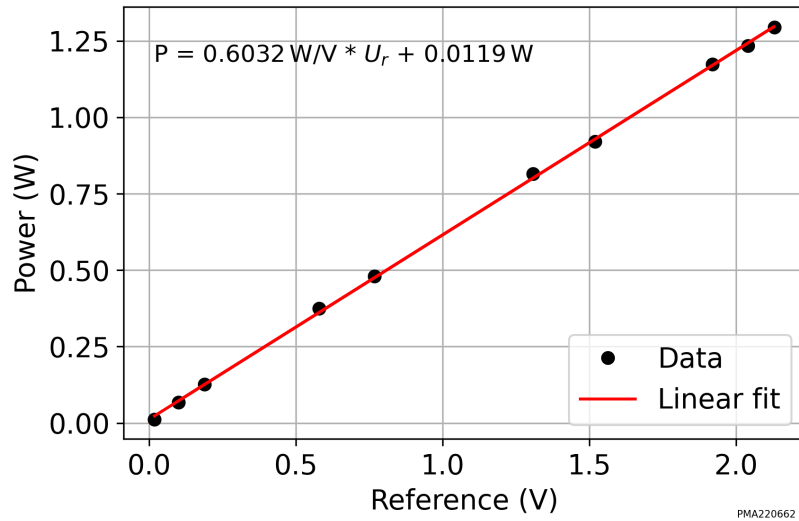


Figure 9.13: The calibration of the KBS-measurements. The power at the location of the KBS is measured with an optical power meter and recorded together with the signal from the reference diode. A linear fit (red) is used for later calculation of power during the measurements.

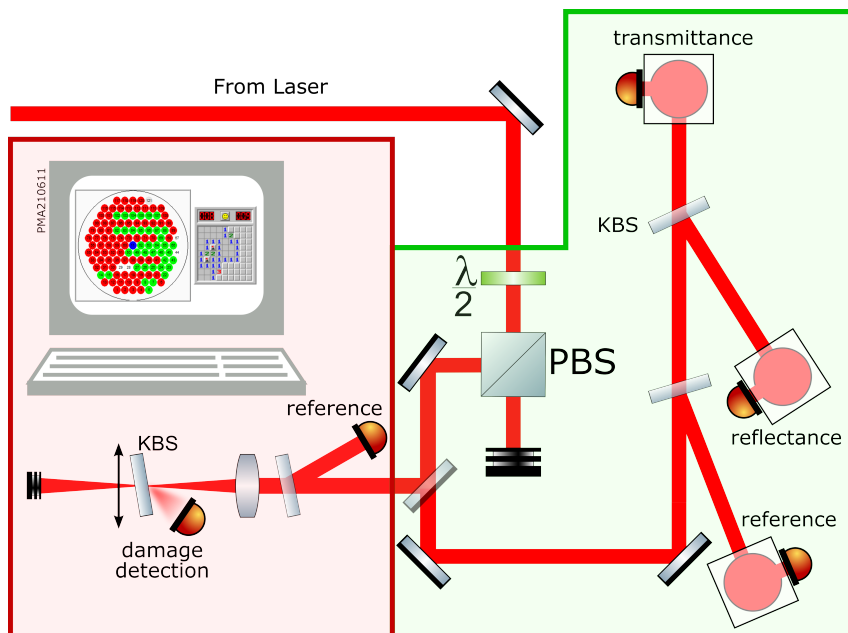


Figure 9.14: A setup for LIDT measurement and characterization of optical switching. The area highlighted in green is identical to the setup depicted in Figure 9.9, the area in red is used for LIDT measurements. Image from [121].

10 Results and discussion

This chapter presents the results of the experiments introduced in Chapter 9, separated by their defining nonlinear effects.

10.1 Frequency tripling mirrors

To investigate the reasons for lower-than-expected conversion efficiencies of the produced FTMs, the experimental setup detailed in Section 9.1 was used to characterize the conversion process. Besides the conversion efficiency itself, the spectral distribution of the generated third harmonic and the influence of the spectral intensity distribution of the fundamental is of main interest. The results presented here were obtained in cooperation with the UNM and published in [95].

The sample under test is a design of type C (compare Chapter 6) with 25 layers. It is intended for a fundamental wavelength of 815 nm, which results in a third harmonic at 272 nm (a) and (b). The sample was coated with the coating machine specified in Section 7.3. The targeted spectral transmittance of the design from 250 nm to 1000 nm, the resulting curve measured after the coating process as well as the field distribution of the design are depicted in Figure 10.1. The layer mainly responsible for the conversion process can be recognized by the internal intensity profile depicted in Figure 10.1 (b). Layer 19 shows a clear maximum of the internal intensity enhancement, which results from the tuning of the design, to be in resonance with the fundamental wavelength.

The total third harmonic generated by this FTM was measured for different energies of the incident laser pulses. The results are presented in Figure 10.2. For low pulse energies, the energy of the generated third harmonic follows the cubic relation with the pulse energy of the fundamental expected for third harmonic conversion processes (compare Equation 2.22). At higher pulse energies close to the LIDT of the sample, the actually generated third harmonic deviates from this relation, which decreases the conversion efficiency.

To further investigate the origins of this decreased efficiency, the spectral intensity distribution of the generated third harmonic was recorded for the different funda-

10 Results and discussion

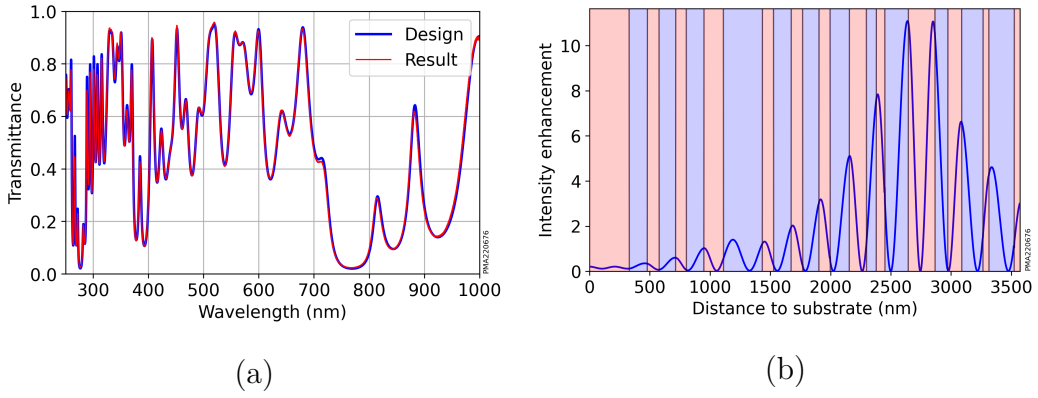


Figure 10.1: The spectral transmittance and internal intensity enhancement of an FTM of type C. (a) shows the spectral transmittance that was targeted with the calculated coating (blue) and the spectral transmittance measured after the coating process (red). The curves are in good agreement. (b) shows the internal intensity enhancement of the layer stack. The different materials of the coating process are highlighted by color, with HfO_2 in light red and SiO_2 in light blue. A clear maximum of the internal intensity is observed in layer 19.

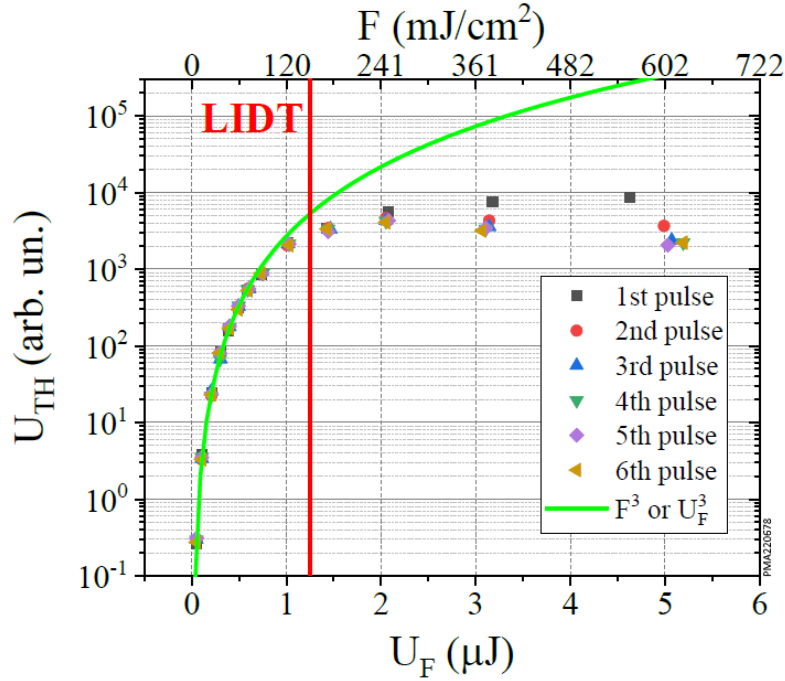


Figure 10.2: The pulse energy of the generated third harmonic (U_{TH}) for different fundamental pulse energies (U_{F}). A clear deviation from the expected curve can be observed at higher intensities. The red vertical line indicates the sample's LIDT. Graph from [95].

mental pulse energies. Figure 10.3 depicts the results of the spectral investigation. Figure 10.3 (a) shows the spectrum of the third harmonic for two energies. At a pulse energy of $0.85 \mu\text{J}$ below the LIDT, the spectral intensity distribution is nar-

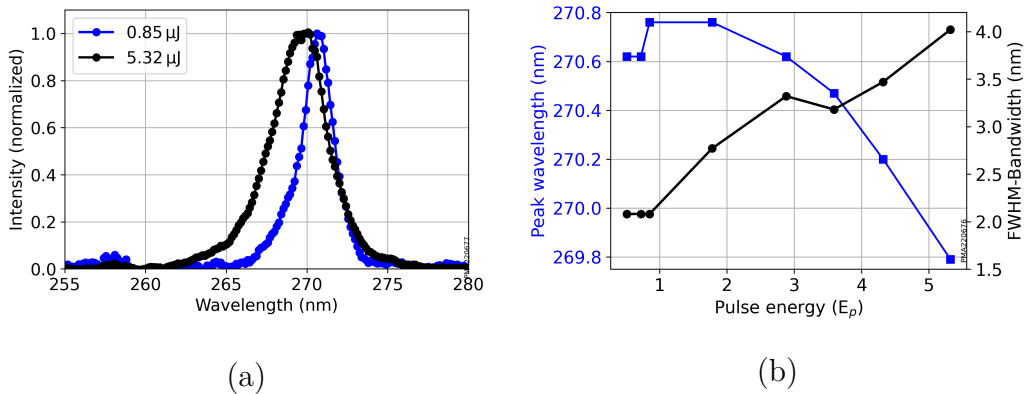


Figure 10.3: Spectral intensity distribution of the generated third harmonic. (a) shows two exemplary intensity distributions, one at low pulse energy and one above the sample’s LIDT. At higher pulse energies, the spectral distribution is much wider, and the peak wavelength is blue-shifted. (b) shows a more systematic evaluation of the observed effects. A clear trend towards lower peak wavelengths and broader spectra is observed.

row and centered around 270.62 nm. At 5.32 μJ above the LIDT, the distribution is much wider, and the peak wavelength is shifted to 269.79 nm. Figure 10.3 (b) shows this trend for all recorded pulse energies. For rising pulse energies, a clear trend towards a broader spectral intensity distribution with shorter peak wavelengths can be observed.

To gain more insight into the reasons for the observed blueshift and spectral broadening of the third harmonic, the relatively broad spectrum around the fundamental wavelength was constrained with the Gaussian filter introduced in Section 9.1. The results of this experiment are depicted in Figure 10.4. In contrast to what is depicted using the full spectrum of the fundamental in Figure 10.3, the behavior of the third harmonic generated by the filtered spectrum does not change significantly with increased pulse energy. Figure 10.4 (a) shows the spectrum of the third harmonic for a pulse energy of 0.5 μJ below the LIDT and a spectrum for an energy of 6.2 μJ, which is far above the LIDT of the sample. At the higher energy, the spectral intensity distribution is slightly wider, but the effect is much less pronounced than that observed in the unfiltered measurements, and the peak wavelength does not shift visibly. (b) shows the width of the third harmonic’s spectrum as well as the position of the highest intensity. Both properties show only minor changes for the different pulse energies.

When these results are viewed in sum, it seems that a physical effect that causes the reduced conversion efficiency and the spectral shift simultaneously takes place at high pulse energies. The observed spectral shift does only occur for the full spectrum

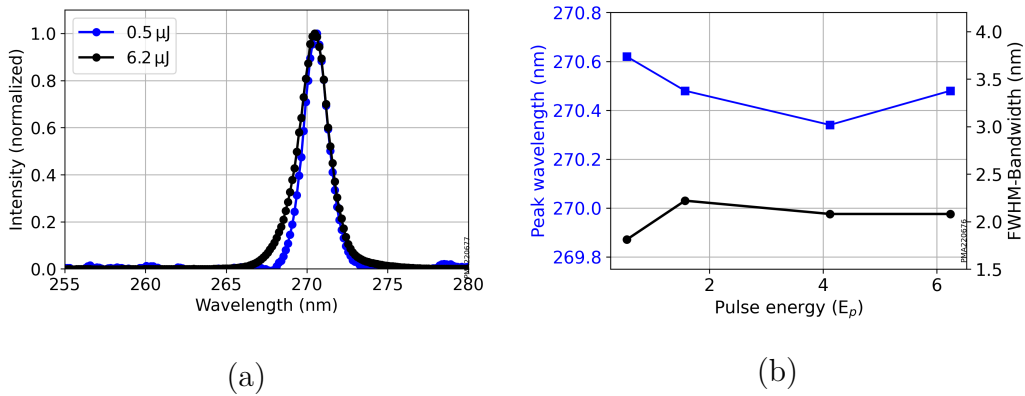


Figure 10.4: The spectral intensity distribution of the generated third harmonic created by a spectrally filtered fundamental. (a) shows two exemplary intensity distributions, one at low pulse energy and one above the sample’s LIDT. In contrast to the unfiltered case, the spectral intensity distribution does not change significantly with pulse energy. (b) shows the evaluation of the observed effects plotted over the fundamental’s pulse energy. No clear trend can be observed for the spectral width of peak wavelength.

of the fundamental pulses, which is much wider than the conversion bandwidth of the FTM. When the bandwidth of the fundamental pulse is restricted to this conversion bandwidth, the spectral shift and broadening are reduced to nearly zero.

The shift of the generated third harmonic to smaller wavelengths is assumed to result from a change of the refractive index caused by high intensities of fundamental radiation in the resonant layer 19 of the design. This change would shift the wavelength of resonance of the FTM. When sufficient intensity of the fundamental pulse is present at this temporarily shifted wavelength, the shifted FTM will generate third harmonic radiation at a correspondingly changed wavelength. If no intensity of the fundamental is available outside of the initial conversion bandwidth, no real shift could be observed. In Chapter 2, two effects that could cause a corresponding change of the refractive index at high laser intensities are introduced. The first effect is the optical Kerr effect, which can be ruled out with high certainty in this case, because the change in refractive index caused by the optical Kerr effect for dielectric material such as the HfO₂ utilized in the FTM under test is positive. Any spectral shifts caused by the optical Kerr effect, therefore, would be towards larger wavelengths, which is contrary to the experimental results.

The second effect is a change in refractive index due to the creation of an electron-hole plasma by the different mechanisms introduced in Section 2.4. The high intensities of the fundamental pulses can excite electrons into the material’s conduction band, where they act as free carriers. Free carriers were shown to reduce the refractive index of dielectric materials as well as introduce additional absorption [35].

This, therefore, matches well with the observed effects, where the spectral shift of the third harmonic is caused by a reduction of the refractive index (mostly) in layer 19 of the FTM, and the reduction of conversion efficiency is caused by the corresponding increase in losses in the FTM.

Since the spatial beam profile of the fundamental beam is not homogeneous, an intensity-dependent reduction of the refractive index would, in parallel to the effects discussed so far, also cause a defocusing of the reflected third harmonic. To test the hypothesis of a refractive index that is reduced by the electron plasma, the spatial beam profile of the third harmonic was recorded for different pulse energies. The images are presented in [95] and show a defocusing of the laser beam in accordance with the expectation.

10.2 Nonlinear refractive index

The nonlinear refractive index of the active materials used in this thesis was measured with the interferometric setup introduced in Section 9.2. The results for the different nonlinear materials applied during this thesis are presented in the following sections.

10.2.1 ITO

The nonlinear refractive index of indium tin oxide was measured during this thesis, and the results were published in [116], where the measurement procedure is discussed in more detail. A short overview of the measurement and its results will be provided in this section.

The interferometric setup detailed in Section 9.2 was used in combination with a commercial Nd:YVO₄ *Lumera Rapid* laser system. A single pass *NeoLase* amplifier was used to augment the available intensity. The laser system features a pulse duration of 12 ps, a repetition frequency of 10 kHz and pulse energies of up to 100 μ J. The sample tested for its nonlinear properties was manufactured with the coating machine described in Section 7.2. A 10 μ m layer of ITO was deposited on a sample of fused silica with a thickness of 1 mm.

To achieve an accurate measurement, two sets of wavefront data were recorded, one at a low pulse energy of 0.04 μ J and another one at a higher pulse energy of 2.45 μ J. The measurement for low energies was used as reference to calculate the relative change of the laser beam's wavefront, which was then evaluated to determine the nonlinear refractive index of the ITO-layer. The relative variation of the wavefront curvature with the corresponding fit is depicted in Figure 10.5. The determined

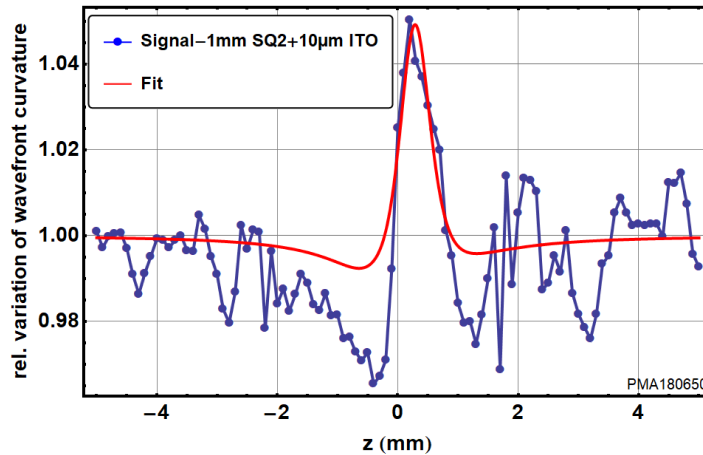


Figure 10.5: The relative change of the wavefront transmitted by the sample. The blue points represent the recorded data, and the red line is a fit for retrieval of the nonlinear refractive index. Graph from [116].

nonlinear refractive index for the ITO-layer is $2.3 \times 10^{-13} \text{ cm}^2/\text{W}$, which is approximately three orders of magnitude higher than that of the substrate material, which features an n_2 of approximately $3 \times 10^{-16} \text{ cm}^2/\text{W}$ [37]. The confirmation of the very high nonlinearity of ITO manufactured by the IBS process utilized in this thesis is essential for the successful integration of ITO layers in the nonlinear optical coatings.

10.2.2 GaAs

To evaluate the capability of GaAs as an active material for the application in KBS, a GaAs sample was characterized for its nonlinear refractive index. The sample under investigation consists of a GaAs-layer with a thickness of $5 \mu\text{m}$ bonded to a fused silica substrate with a thickness of 1.5 mm . The setup presented in Section 9.2 was applied together with a *Satsuma* laser system from *Amplitude Laser*, delivering pulse durations of 300 fs at a central wavelength of 1030 nm and a repetition frequency of 250 kHz .

The measurement was performed at a pulse energy of 96 nJ . The resulting relative change of the transmitted wavefront of the laser beam is depicted in Figure 10.6. A nonlinear refractive index of $5.3 \times 10^{-13} \text{ cm}^2/\text{W}$ was calculated from the measured data. The best reference available from literature is a value of $3 \times 10^{-13} \text{ cm}^2/\text{W}$ and was measured at a wavelength of 1550 nm . This is in good agreement with the measured value. The nonlinear refractive index of GaAs is therefore well suited for the intended applications with lasers of wavelengths around $1 \mu\text{m}$.

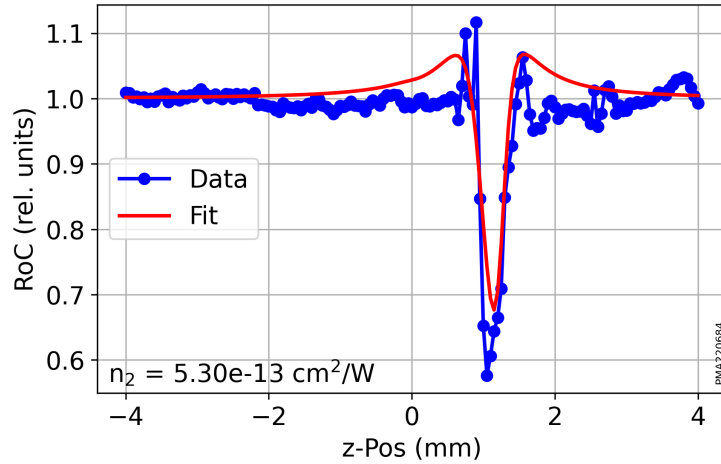


Figure 10.6: Relative change of the wavefront transmitted by the GaAs-sample. The blue points represent the recorded data, and the red line is a fit for retrieval of the nonlinear refractive index.

10.3 Kerr-Band-Switches

After manufacturing of the KBS-samples with the methods described in Chapter 7 using the active materials introduced in Chapter 3, this section will provide insight into the switching performance of the KBS to test the concept of optical switches. The setup applied for characterizing the switching behavior is described in Section 9.3. The results for the validation of the optical switching as well as the relation to the samples LIDT, were published in the frame of this thesis [122, 121].

10.3.1 Optical switching

This subsection details the results obtained for the optical switching of the produced KBS. Transmittance and reflectance were measured utilized to calculate the absorption in the samples under test.

ITO as active material

The design chosen for the validation of the optical switching has the fundamental form of $(HL)^6\text{ITO}(\text{LH})^6$ with a central ITO-layer with a thickness of 2 QWOT. The design was optimized numerically with the process described in Chapter 5. The spectral transmittance of the design as well as that of the sample measured after coating, are presented in Figure 10.7. The sample is intended for measurement with a laser system operating at 1030 nm. To allow precise tuning of the peak transmittance to the laser wavelength during the measurement, the design was shifted to slightly higher wavelengths. The peak transmittance of the initial design at the

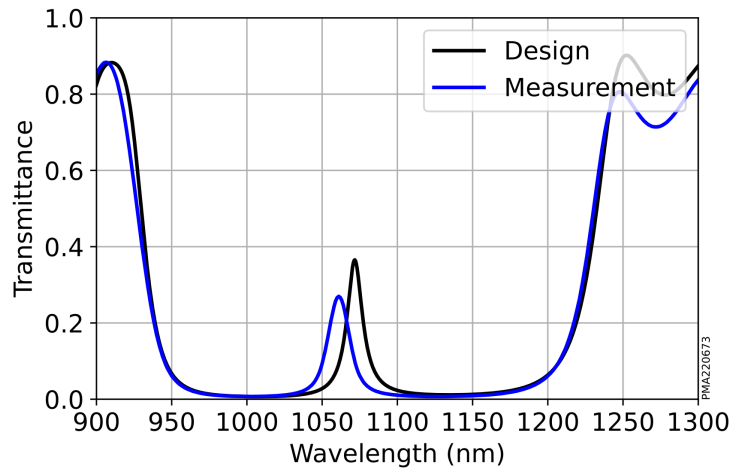


Figure 10.7: The transmittance of the KBS as designed (black) and as measured after the coating process (blue). The sample is intended for applications at 1030 nm and designed for slightly longer wavelengths, which allows tuning of the transmittance peak with the angle of incidence during the measurement. Graph from [122].

central wavelength is 36%. The value measured by the spectrophotometer after deposition is 27%. The difference probably results from small changes in the losses of the ITO that can vary between different batches of coatings. The spectral shift between design and measurement is assumed to result from small thickness errors in the spacer layer and is compensated by tuning the angle during measurement. The spectral bandwidth of the transmittance peak is approximately 17 nm, which is much larger than the bandwidth of the lasers system, which is approximately 0.5 nm (as depicted in Figure 9.10).

The results of the intensity-dependent measurement of transmittance and reflectance are presented in Figure 10.8. Figure 10.8 (a) shows the transmittance, which decreases from initially 26%, which closely matches the value expected from the spectrophotometric measurements, to 14% before the sample started to change irreversibly due to irradiation. For the same change in intensity, the reflectance depicted in Figure 10.8 (b) increases from 55% to 77%. No significant hysteresis can be observed when the curves for increasing and decreasing intensity are compared. The calibration of transmittance and reflectance with known 100%-references allow the determination of the total losses in the KBS during irradiation at varying intensity levels by calculating $1 - T - R$. Due to the high absorption observed in ITO at low annealing temperatures, absorption is assumed to be the main contributor to the losses observed in the KBS-sample. The resulting total losses are shown in Figure 10.9. A clear decrease of the losses from approximately 20% to below 10% can be observed.

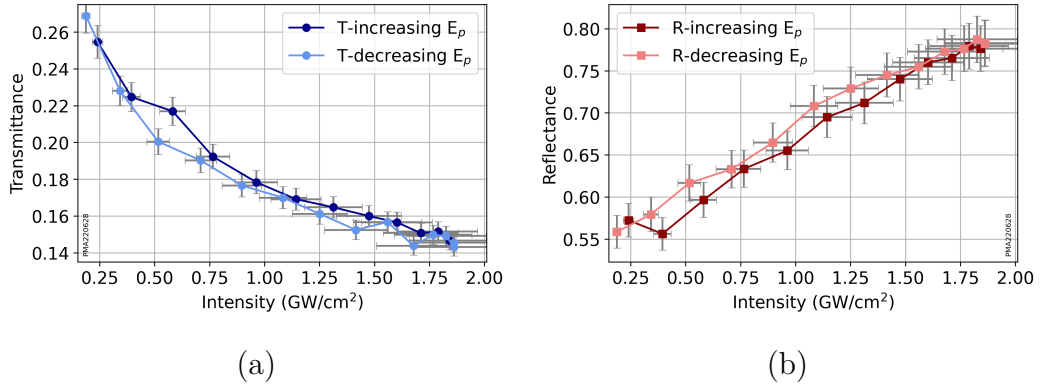


Figure 10.8: The transmittance (a) and reflectance (b) of the ITO-KBS for increasing (darker shade) and decreasing (lighter shade) intensities. Transmittance decreases, and reflectance increases for higher intensities. The curves show no significant hysteresis. Graph adapted from [122].

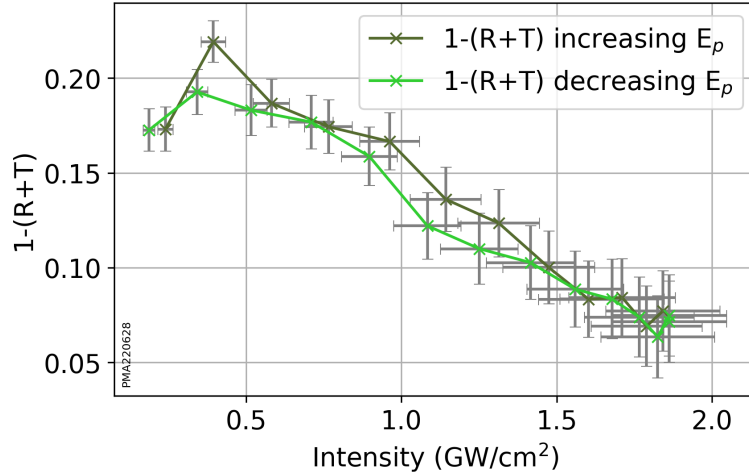


Figure 10.9: Total optical losses of an ITO-KBS for different intensity levels. For increasing intensity on the KBS, a decrease in losses can be observed. Graph adapted from [122].

The decrease in transmittance, in combination with the increase in reflectance, is in line with the expectation of the KBS's behavior. For high intensities, the refractive index of the central spacer layer changes, and the peak of transmittance shifts to higher wavelengths due to this. Since the KBS is initially aligned for maximum transmittance, this shift causes the transmittance to drop with a simultaneous increase in reflectance. The drop in optical losses can be explained similarly. Initially, the design is in resonance with the laser wavelength, causing a high internal intensity enhancement in the central ITO layer. This enhancement, in combination with the relatively high losses of the material, causes the high initial losses in the KBS. When the design switches, the intensity in this layer is reduced since the laser wavelength

is no longer resonant with the layer stack, the intensity enhancement in the spacer layer decreases, which in turn leads to lower absolute losses in the component. The reduction in optical losses, therefore, is an indicator of the desired optical switching. To test the repeatability of the observed effects, and exclude the possibility that the changes in reflectance and transmittance result from annealing effects or damage to the optical coating, the measurement was repeated several times without changing the laser parameters or the spot on the KBS-sample. The results are presented in Figure 10.10. All three measurements show very similar behavior. The first one shows small differences from the other two that may result from thermal effects, and could cause small changes to reflectance and transmittance if the sample heats up during measurement. However, the behavior of the KBS is repeatable over several measurements, which excludes any damage or annealing effects as source for the observed modulation of reflectance and transmittance.

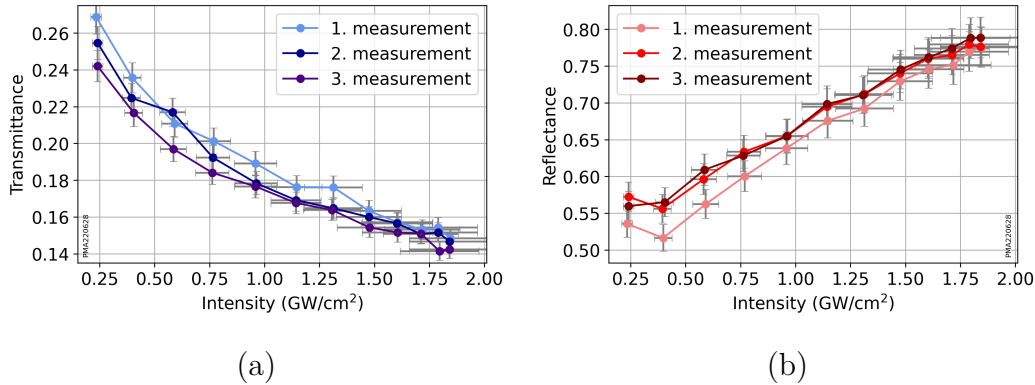


Figure 10.10: The transmittance (a) and reflectance (b) of the GaAs-KBS for increasing (darker shade) and decreasing (lighter shade) intensities. The behavior of the sample does not change with several repetitions of the same measurement, excluding damage effects or permanent material modification as source of the observed changes. Graph adapted from [122].

GaAs as active material

The second active material selected for the validation of optical switching is GaAs. The samples were produced as described in Section 8.2 in a substrate-free form where a GaAs-wafer forms the central spacer layer, and both surfaces are coated to achieve the desired band-pass-like structures. The manufactured sample was tested for its reflectance and transmittance in the setup introduced in Section 9.3. The results are depicted in Figure 10.11.

To cover a wider range of intensities, two measurements were combined. Up to an intensity of approximately 8 GW/cm^2 , the transmittance decreases from 26 %

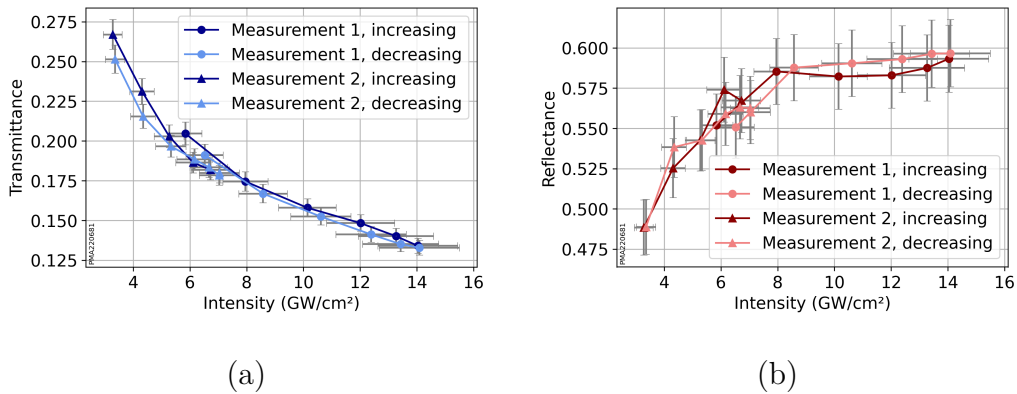


Figure 10.11: The transmittance (a) and reflectance (b) of the GaAs-KBS-sample for increasing (dark shade) and decreasing (lighter shade) intensities. Two measurements were performed to cover the necessary intensity range. For increasing intensities, transmittance decreases and reflectance increases. At approximately 8 GW/cm², the reflectance reaches an almost constant level, while the transmittance continues to decrease.

to approximately 17.5%. For the same intensity range, the reflectance increases from approximately 49% to over 58%. This behavior at low intensity values is similar to that observed for ITO-KBS with anti-parallel behavior for reflectance and transmittance. However, when the intensity is increased further, the behavior starts to change. Transmittance continues to decrease, albeit with a shallower slope, only decreasing to 13.4% between 8 GW/cm² and the maximum value of 14 GW/cm². In the same intensity range, the reflectance almost stays at a constant value of approximately 59%. This effect can also be observed in the losses of the component. Figure 10.12 displays the losses calculated from the transmittance and reflectance. For the lower intensity range, the losses are constantly around 25%. In the higher intensity range, the losses increase due to the lower transmittance and constant reflectance. It has to be noted, however, that the observed change is relatively small compared to the measurements' uncertainty.

This behavior matches the expectations for a semiconductor material like GaAs that is irradiated with photons that possess energies higher than half the materials band gap. In this constellation, the interaction with intense radiation causes free carriers to be generated by two-photon absorption. At low intensities, the free carriers only cause minor changes to the properties of the material, such as a change in the refractive index, in this experiment made visible by the optical switching of the KBS. When the intensity is further increased, the amount of free carriers increases and they start to absorb light themselves (detailed in Section 2.4), as can be seen by the increasing losses calculated from the measurements.

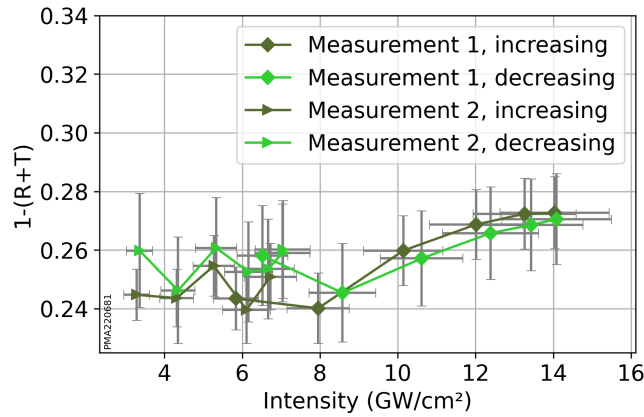


Figure 10.12: Total optical losses of a GaAs-KBS for different intensity levels. For low intensities, the losses stay almost constant at approximately 25 %. At intensities above 8 GW/cm², the losses start to increase.

10.3.2 Thermal effects

To investigate the possible influence of thermal effects on KBS-performance, another set of measurements was performed. When the modulation of transmittance and reflectance observed in the previous section are the results of thermal effects, they should scale with the average power and, therefore, with repetition frequency of the laser system. The optical Kerr effect, however, scales with intensity, which is not directly correlated to the repetition frequency for the laser system applied in the tests presented here. Therefore, measurements at repetition rates of 2.5 kHz and 10 kHz were recorded. The results of this investigation are presented in Figure 10.13.

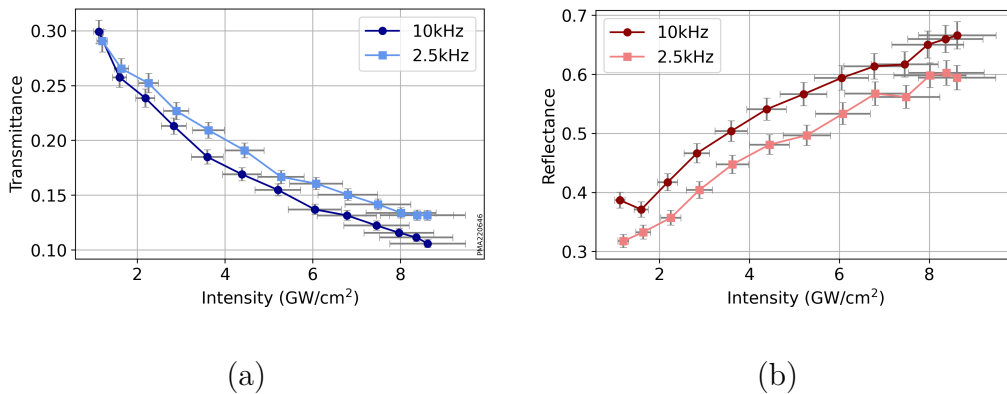


Figure 10.13: The transmittance (a) and reflectance (b) of the KBS-sample for increasing (dark shade) and decreasing (lighter shade) intensities. Transmittance decreases and reflectance increases for higher intensities. The curves show no significant hysteresis.

The transmittance in Figure 10.13 (a) seems to show a slightly reduced amplitude for the lower repetition frequency, which could indicate an influence of the reduced average power. This behavior, however, is not matched by the reflectance depicted in Figure 10.13 (b), which shows an unchanged amplitude of its change, and rather an almost constant offset between the two curves.

The results do not indicate a significant influence of thermal effects on the functioning of the KBS-samples, but more detailed investigations are needed to gain a clearer picture.

10.3.3 Relation to the LIDT

An essential property of the KBS-concept is the dynamic range. The intensity range in which the optical switching takes place and its relation to the damage threshold of the component, e.g. it is desirable, that the switch works before it is destroyed by the intense laser radiation. Ideally, there is sufficient modulation of reflectance and transmittance at low intensities, that the component does not need to be used at intensities near its LIDT.

To characterize this relation, a KBS-sample was tested for its switching behavior, after which the LIDT of the same sample was measured with the combined setup introduced in Section 9.3.1. The intensity-dependent transmittance and reflectance of the sample are presented in Figure 10.14. Similar to the samples tested in the previous section, a clear decrease in transmittance, together with an increase in reflectance can be observed for rising fluences. To allow better comparability with

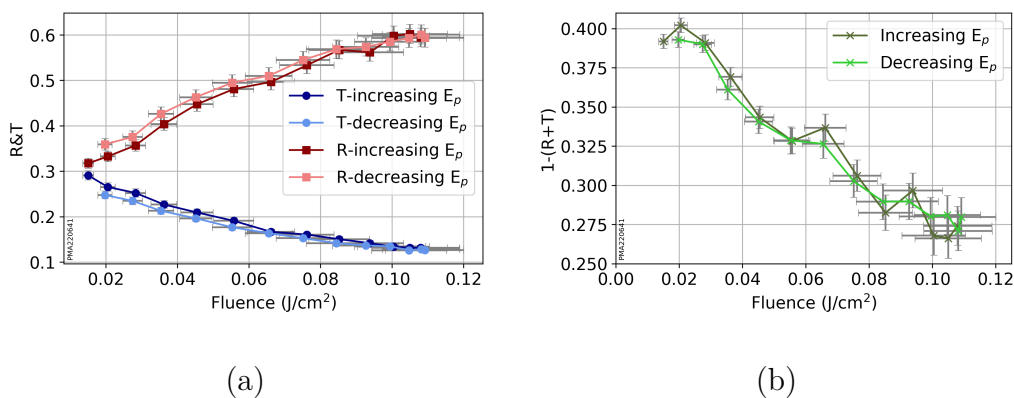


Figure 10.14: The results of the switching test before the LIDT measurement. A clear decrease of transmittance with a parallel increase of reflectance can be observed for rising fluences on the sample (a). From transmittance and reflectance, the optical losses of the KBS-sample can be calculated, which decrease significantly with rising fluences (b). Graphs adapted from [121].

10 Results and discussion

the LIDT measurement, fluence instead of intensity is used as parameter in this investigation. The transmittance decreases from 29 % to 13 %, while the reflectance increases from 32 % to 60 %. From the transmittance and reflectance of the KBS-samples, their total optical losses can be calculated. Again, in parallel to what was observed before, the optical losses of the sample decrease from 39 % to 27 % with rising intensity, which is attributed to the optical shift of the central spacer layer and the corresponding reduction of intensity when the design shifts out of resonance with the laser wavelength. Overall, the sample shows significant changes of transmittance and reflectance in the range of considered fluences up to 0.11 J/cm^2 .

After the optical switching was validated for the sample, LIDT measurements were performed. The characteristic damage curve as well as the morphology of an exemplary damaged spot on the sample's surface are presented in Figure 10.15. Figure 10.15 (a) shows the characteristic damage curve of the samples, where a decrease of the LIDT with higher pulse numbers can be observed. Since the intended applications of a KBS as mode-locking- or power-limiting-device require continuous use, the LIDT for high pulse numbers is of interest and indicated by a horizontal red line. The sample's LIDT was determined to be 0.13 J/cm^2 .

In summary, the sample under investigation shows a significant change of almost a factor of two for transmittance and reflectance for fluences up to 0.11 J/cm^2 , which is below the determined LIDT of 0.13 J/cm^2 . The criterion that was initially set for a realistic application of the KBS-concept is therefore fulfilled. The optical switching already occurs at fluences well below the LIDT, so that the component can be used without the risk of damage.

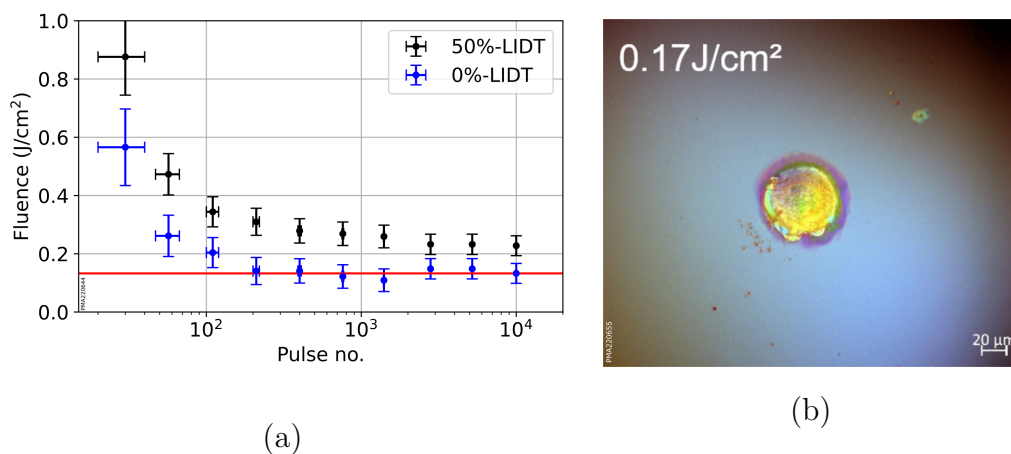


Figure 10.15: Characteristic damage curve for the KBS-sample (a). The red line indicates the assumed limit of the LIDT of 0.13 J/cm^2 for the case on infinite pulses. The damage morphology displayed in (b) is typical for short pulse durations as applied in this measurement. Graph and image adapted from [121].

11 Conclusion and outlook

In this thesis, the implementation of nonlinear optical effects in thin film interference coatings was investigated. The amorphous materials utilized in thin film coatings focused the investigations on nonlinear effects of the third order, of which third harmonic generation for later application in **F**requency-**T**ripling-**M**irrors (FTMs) and the optical Kerr effect for application in **K**err-**B**and-**S**witches (KBS) were selected for integration into specially designed coating systems.

To this end, the theoretical foundations for nonlinear effects of the third order were established, and the generation and influence of free electrons in dielectric and semiconductor materials were introduced. Special attention was given to the optical Kerr effect in dielectric materials and related effects, which enhance the nonlinear refractive index in epsilon-near-zero materials and semiconductors.

For integration of these nonlinear effects into the thin film coatings, the fundamentals and calculation procedures of dielectric interference coatings were introduced, featuring a more detailed description of band-pass-coatings, and the special requirements of KBS and FTM were discussed. To obtain a better understanding of the interaction between the refractive index shift caused by the optical Kerr effect and the intensity enhancement in the optical coatings, a simulation procedure was proposed and developed. This procedure allows to observe the interaction of single pulses with a thin film design and was applied to optimize the switching behavior of band-pass designs toward more efficient KBS. In addition to more typical dielectric materials, the simulation showed a highly beneficial influence of strongly nonlinear materials in specially selected, so-called 'active' layers of the coatings.

After these theoretical foundations were laid, the manufacturing of the optical coatings by ion beam sputtering was explained. FTM and KBS were manufactured with differing approaches to the coating process because of their different requirements in accuracy and materials. FTMs require precise monitoring of layer thickness and dispersion of the refractive indices of the utilized materials. Therefore, the corresponding coating machine was equipped with a newly developed high-resolution broadband monitor capable of monitoring the transmittance of the components for both the fundamental and the third harmonic wavelengths. KBS do not necessar-

ily require the same amount of resolution and bandwidth in the optical monitoring but depend on highly nonlinear optical materials for an efficient switching process. Therefore, the coating process was adapted to include epsilon-near-zero-materials and semiconductors as active materials.

This allowed the investigation of these highly nonlinear materials for the KBS. As semiconductor material, GaAs was selected, and measurements confirmed the significantly increased nonlinear refractive index compared to the dielectric materials in the coatings suggested by literature. However, implementing GaAs in optical coatings is problematic, and special wafers were selected to form KBS as substrate-free optics with coatings on both wafer surfaces. Another class of active materials are the so-called epsilon-near-zero materials, which are reported to feature extremely high nonlinear refractive indices. Indium-Tin-Oxide (ITO) was chosen from this group, and measurements confirmed the reported high nonlinear refractive index. The manufacturing via IBS, the general optical and electrical properties of ITO, and the material's laser-induced damage threshold were investigated in more detail to find a parameter set suitable for the integration into KBS and a strong dependence on oxygen and thermal treatment after deposition could be identified.

Finally, the properties of the produced components were investigated. The frequency-tripling mirrors showed increased conversion efficiency of about 1 %, but the values remained below the theoretical expectations. A spectral shift observed in the third harmonic indicates the generation of free carriers during the conversion process. The absorption caused by these carriers could explain the observed deviation from the expected behavior.

The performance of the KBS was measured by a combined measurement of reflectance and transmittance for varying the incident intensities, which also allows the calculation of the intensity-dependent losses in the components. For both the ITO-KBS and the variant based on GaAs, optical switching could be observed, with decreasing transmittance and a simultaneous increase in reflectance. The highest switching amplitudes were reached for KBS based on ITO, with a reduction in transmittance of almost 20 % and an increase in reflectance of approximately 30 %. Since the LIDT of the components limits the maximum intensity available for optical switching, the relation of the switching to this damage threshold was investigated and was measured at fluences higher than those necessary to achieve optical switching.

In summary, this thesis investigated two concepts for integrating nonlinear optical effects into thin film interference coatings. Materials for the different applications were examined and manufactured, the optical coatings produced and characterized

for their intended functions. The optical switches investigated in this thesis showed the desired function with strong modulation of reflectance and transmittance. However, to reach their intended application as mode-locking components, their currently relatively high initial losses need to be reduced further. Therefore, the next steps in their development are further improvements of the manufacturing process and the continuation of research on different active materials that could show improved properties. Good candidates for alternative materials are semiconductors with a more advantageous band gap energy when compared to GaAs, such as GaP or SiC in its 3C-form. The exact course and speed of the optical switching also remain to be determined. A pump-probe experiment could be applied to obtain improved insight into these properties and properly reveal the single pulse interaction, as well as perhaps the spectral width of the caused shift of spectral properties.

Overall, integrating nonlinear optical effects into thin film interference coatings seems highly promising. FTMs are still limited by the material interactions but could already be shown to increase the conversion efficiency by five orders of magnitude compared to standard coatings. Especially the optical switches presented in this work show significant potential not only for laser applications in mode-locking or power-limiting but could be a start to an optical transistor that enables controlled ultrafast switching of light for many applications.

Bibliography

- [1] Maiman, T.H. Stimulated optical radiation in ruby. *Nature*, 187(4736):493–494, August 1960. doi: 10.1038/187493a0.
- [2] Franken, P.A., Hill, A.E., Peters, C.W., and Weinreich, G. Generation of optical harmonics. *Physical Review Letters*, 7(4):118–119, August 1961. doi: 10.1103/physrevlett.7.118.
- [3] Nauta, J., Oelmann, J.H., Borodin, A., Ackermann, A., Knauer, P., Muhammad, I.S., Pappenberger, R., Pfeifer, T., and López-Urrutia, J.R.C. XUV frequency comb production with an astigmatism-compensated enhancement cavity. *Optics Express*, 29(2):2624, January 2021. doi: 10.1364/oe.414987.
- [4] Zander, J., Rembe, C., and Schnabel, R. 10 dB interferometer enhancement by squeezing of photon shot noise with sub-femtometer resolution and eye-safe optical power. *Quantum Science and Technology*, 8(1):01LT01, October 2022. doi: 10.1088/2058-9565/ac9ad5.
- [5] Abramczyk, H., Brozek-Pluska, B., Jarota, A., Surmacki, J., Imiela, A., and Kopec, M. A look into the use of raman spectroscopy for brain and breast cancer diagnostics: linear and non-linear optics in cancer research as a gateway to tumor cell identity. *Expert Review of Molecular Diagnostics*, 20(1):99–115, January 2020. doi: 10.1080/14737159.2020.1724092.
- [6] Lamb, W.E. Theory of an optical maser. *Physical Review*, 134(6A):A1429–A1450, June 1964. doi: 10.1103/physrev.134.a1429.
- [7] Fujimoto, J.G., Weiner, A.M., and Ippen, E.P. Generation and measurement of optical pulses as short as 16 fs. *Applied Physics Letters*, 44(9):832–834, May 1984. doi: 10.1063/1.94957.
- [8] *FEMTOKITS FOR THIRD HARMONIC GENERATION OF FEMTOSECOND Ti:Sapphire LASER*. Eksma Optics, Dvarčionių g. 2B, 10233 Vilnius, Lithuania, rev. 20220510 edition, 2022.

Bibliography

- [9] Plinius Secundus, G. *Naturalis Historiae/Naturkunde - Buch XXXIII: Metallurgie*. De Gruyter, 2013. ISBN 3050062061. URL https://www.ebook.de/de/product/21505553/buch_33_metallurgie.html.
- [10] Greene, J.E. Review article: Tracing the recorded history of thin-film sputter deposition: From the 1800s to 2017. *Journal of Vacuum Science & Technology A: Vacuum, Surfaces, and Films*, 35(5):05C204, September 2017. doi: 10.1116/1.4998940.
- [11] Taylor, H.D. Improvements in lenses. Patent, November 1894.
- [12] CARL ZEISS FA. Verfahren zur Erhöhung der Lichtdurchlässigkeit optischer Teile durch Erniedrigung des Brechungsindex an den Grenzflächen dieser optischen Teile. Patent, November 1936. URL <https://worldwide.espacenet.com/patent/search/family/007625750/publication/DE685767C?q=pn=DE685767>.
- [13] Willemsen, T., Chaulagain, U., Borneis, S., and Ebert, W. New IBS coatings boost performance of petawatt laser mirrors. *PhotonicsViews*, 19(2):54–58, April 2022. doi: 10.1002/phvs.202200016.
- [14] Degallaix, J., Michel, C., Sassolas, B., Allocca, A., Cagnoli, G., Balzarini, L., Dolique, V., Flaminio, R., Forest, D., Granata, M., Lagrange, B., Straniero, N., Teillon, J., and Pinard, L. Large and extremely low loss: the unique challenges of gravitational wave mirrors. *Journal of the Optical Society of America A*, 36(11):C85, October 2019. doi: 10.1364/josaa.36.000c85.
- [15] Wang, J., Sciarrino, F., Laing, A., and Thompson, M.G. Integrated photonic quantum technologies. *Nature Photonics*, 14(5):273–284, oct 2019. doi: 10.1038/s41566-019-0532-1.
- [16] Boyd, R.W. *Nonlinear Optics*. Elsevier Acad. Press, 2008.
- [17] Reider, G.A. *Photonik*. Springer Nature, 2012. doi: 10.1007/978-3-7091-1521-3. URL <http://dx.doi.org/10.1007/978-3-7091-1521-3>.
- [18] Demtröder, W. *Experimentalphysik 2*. Springer Berlin Heidelberg, 2013. ISBN 978-3-642-29943-8. doi: 10.1007/978-3-642-29944-5.
- [19] New, G. *Introduction to Nonlinear Optics*. Cambridge University Press, April 2011. doi: 10.1017/cbo9780511975851.

Bibliography

- [20] *Nonlinear Crystals: LBO - Lithium triborate*. Eksma Optics, Dvarčionių g. 2B, 10233 Vilnius, Lithuania, rev. 2022051 edition, 2022.
- [21] Hum, D.S. and Fejer, M.M. Quasi-phasematching. *Comptes Rendus Physique*, 8(2):180–198, March 2007. doi: 10.1016/j.crhy.2006.10.022.
- [22] Stryland, E.W.V., Woodall, M.A., Vanherzeele, H., and Soileau, M.J. Energy band-gap dependence of two-photon absorption. *Optics Letters*, 10(10):490, October 1985. doi: 10.1364/ol.10.000490.
- [23] Ams, M., Little, D., and Withford, M. Femtosecond-laser-induced refractive index modifications for photonic device processing. In *Laser Growth and Processing of Photonic Devices*, pages 305–332. Elsevier, 2012. doi: 10.1533/9780857096227.3.305.
- [24] Mero, M., Liu, J., Rudolph, W., and Starke, K. Scaling laws of femtosecond laser pulse induced breakdown in oxide films. *Physical Review B*, 71(115109), 2005. doi: 10.1103/PhysRevB.71.115109. URL <https://journals.aps.org/prb/abstract/10.1103/PhysRevB.71.115109>.
- [25] Keldysh, L.V. Ionization in the Field of a Strong Electromagnetic Wave. *J. Exp. Theor. Phys.*, 20(5):1307–1314, 1965.
- [26] Bettis, J.R. Electron tunnel ionization: the pulse length and wavelength dependence. In Exarhos, G.J., Guenther, A.H., Kozlowski, M.R., Lewis, K.L., and Soileau, M.J., editors, *SPIE Proceedings*. SPIE, March 2000. doi: 10.1117/12.379295.
- [27] Rethfeld, B. Unified model for the free-electron avalanche in laser-irradiated dielectrics. *Physical Review Letters*, 92(18):187401, May 2004. doi: 10.1103/physrevlett.92.187401.
- [28] Ristau, D., Jupé, M., and Starke, K. Laser damage thresholds of optical coatings. *Thin Solid Films*, 518(5):1607–1613, December 2009. doi: 10.1016/j.tsf.2009.07.150.
- [29] Tien, A.C., Backus, S., Kapteyn, H., Murnane, M., and Mourou, G. Short-pulse laser damage in transparent materials as a function of pulse duration. *Physical Review Letters*, 82(19):3883–3886, May 1999. doi: 10.1103/physrevlett.82.3883.
- [30] Drude, P. Zur elektronentheorie der metalle. *Annalen der Physik*, 306(3): 566–613, 1900. doi: 10.1002/andp.19003060312.

Bibliography

- [31] Drude, P. Zur elektronentheorie der metalle; II. teil. galvanomagnetische und thermomagnetische effecte. *Annalen der Physik*, 308(11):369–402, 1900. doi: 10.1002/andp.19003081102.
- [32] Mero, M., Liu, J., Sabbah, A.J., Zeller, J., Rudolph, W., Starke, K., and Ristau, D. Laser breakdown of dielectric oxide films from 20 fs to 1 ps. In *Frontiers in Optics, OSA Technical Digest (CD)*, number MT15. Optica Publishing Group, 2003. doi: 10.1364/fio.2003.mt15.
- [33] Melninkaitis, A., Šiaulys, N., Smalakys, L., Momgaudis, B., Vaicenavičius, J., Barkauskaitė, S., Sirutkaitis, V., Gallais, L., and Guizard, S. What time-resolved measurements tell us about femtosecond laser damage? In Exarhos, G.J., Gruzdev, V.E., Menapace, J.A., Ristau, D., and Soileau, M., editors, *Laser-Induced Damage in Optical Materials: 2015*. SPIE, November 2015. doi: 10.1117/12.2195333.
- [34] Alam, M.Z., Leon, I.D., and Boyd, R.W. Large optical nonlinearity of indium tin oxide in its epsilon-near-zero region. *Science*, 352(6287):795–797, May 2016. doi: 10.1126/science.aae0330.
- [35] Mero, M., Sabbah, A., Zeller, J., and Rudolph, W. Femtosecond dynamics of dielectric films in the pre-ablation regime. *Applied Physics A*, 81(2):317–324, July 2005. doi: 10.1007/s00339-005-3216-2.
- [36] Macleod, H.A. *Thin-film optical filters*. Taylor & Francis, 2010. ISBN 9781420073027.
- [37] Milam, D. Review and assessment of measured values of the nonlinear refractive-index coefficient of fused silica. *Applied Optics*, 37(3):546, January 1998. doi: 10.1364/ao.37.000546.
- [38] Gao, L., Lemarchand, F., and Lequime, M. Refractive index determination of SiO₂ layer in the UV/vis/NIR range: spectrophotometric reverse engineering on single and bi-layer designs. *Journal of the European Optical Society: Rapid Publications*, 8, January 2013. doi: 10.2971/jeos.2013.13010.
- [39] Boidin, R., Halenkovič, T., Nazabal, V., Beneš, L., and Němec, P. Pulsed laser deposited alumina thin films. *Ceramics International*, 42(1):1177–1182, January 2016. doi: 10.1016/j.ceramint.2015.09.048.

Bibliography

- [40] Adair, R., Chase, L.L., and Payne, S.A. Nonlinear refractive index of optical crystals. *Physical Review B*, 39(5):3337–3350, February 1989. doi: 10.1103/physrevb.39.3337.
- [41] DeSalvo, R., Said, A., Hagan, D., Stryland, E.V., and Sheik-Bahae, M. Infrared to ultraviolet measurements of two-photon absorption and n^2 in wide bandgap solids. *IEEE Journal of Quantum Electronics*, 32(8):1324–1333, 1996. doi: 10.1109/3.511545.
- [42] Major, A., Yoshino, F., Nikolakakos, I., Aitchison, J.S., and Smith, P.W.E. Dispersion of the nonlinear refractive index in sapphire. *Optics Letters*, 29(6):602, March 2004. doi: 10.1364/ol.29.000602.
- [43] Bright, T., Watjen, J., Zhang, Z., Muratore, C., and Voevodin, A. Optical properties of hfo₂ thin films deposited by magnetron sputtering: From the visible to the far-infrared. *Thin Solid Films*, 520(22):6793–6802, September 2012. doi: 10.1016/j.tsf.2012.07.037.
- [44] Carvalho, D., Hernandez Figueroa, H., and Lipson, M. Self phase modulation measurement of the nonlinear index of hfo₂. In *Proceedings: Seminatec 2017 - XII Workshop on semiconductions and micro & nano technology*, 2017.
- [45] Bright, T.J., Watjen, J.I., Zhang, Z.M., Muratore, C., Voevodin, A.A., Koukis, D.I., Tanner, D.B., and Arenas, D.J. Infrared optical properties of amorphous and nanocrystalline ta₂o₅ thin films. *Journal of Applied Physics*, 114(8):083515, August 2013. doi: 10.1063/1.4819325.
- [46] Tai, C.Y., Wilkinson, J.S., Perney, N.M.B., Netti, M.C., Cattaneo, F., Finlayson, C.E., and Baumberg, J.J. Determination of nonlinear refractive index in a ta₂o₅ rib waveguide using self-phase modulation. *Optics Express*, 12(21):5110, 2004. doi: 10.1364/opex.12.005110.
- [47] Siefke, T., Kroker, S., Pfeiffer, K., Puffky, O., Dietrich, K., Franta, D., Ohlídal, I., Szeghalmi, A., Kley, E.B., and Tünnermann, A. Materials pushing the application limits of wire grid polarizers further into the deep ultraviolet spectral range. *Advanced Optical Materials*, 4(11):1780–1786, July 2016. doi: 10.1002/adom.201600250.
- [48] Caspani, L., Kaipurath, R., Clerici, M., Ferrera, M., Roger, T., Kim, J., Kinsey, N., Pietrzyk, M., Falco, A.D., Shalaev, V., Boltasseva, A., and Faccio, D. Enhanced nonlinear refractive index in ϵ -near-zero materials. *Physical Review Letters*, 116(23):233901, June 2016. doi: 10.1103/physrevlett.116.233901.

Bibliography

- [49] Reshef, O., Leon, I.D., Alam, M.Z., and Boyd, R.W. Nonlinear optical effects in epsilon-near-zero media. *Nature Reviews Materials*, 4(8):535–551, June 2019. doi: 10.1038/s41578-019-0120-5.
- [50] Ciattoni, A., Rizza, C., and Palange, E. Extreme nonlinear electrostatics in metamaterials with very small linear dielectric permittivity. *Physical Review A*, 81(4):043839, April 2010. doi: 10.1103/physreva.81.043839.
- [51] Ciattoni, A., Rizza, C., and Palange, E. Transmissivity directional hysteresis of a nonlinear metamaterial slab with very small linear permittivity. *Optics Letters*, 35(13):2130, June 2010. doi: 10.1364/ol.35.002130.
- [52] Argyropoulos, C., Chen, P.Y., D’Aguanno, G., Engheta, N., and Alù, A. Boosting optical nonlinearities in ϵ -near-zero plasmonic channels. *Physical Review B*, 85(4):045129, January 2012. doi: 10.1103/physrevb.85.045129.
- [53] Maier, S.A. *Plasmonics*. Springer, 2007. ISBN 9780387331508.
- [54] Carnemolla, E.G., Caspani, L., DeVault, C., Clerici, M., Vezzoli, S., Bruno, V., Shalaev, V.M., Faccio, D., Boltasseva, A., and Ferrera, M. Degenerate optical nonlinear enhancement in epsilon-near-zero transparent conducting oxides. *Optical Materials Express*, 8(11):3392, October 2018. doi: 10.1364/ome.8.003392.
- [55] Feigenbaum, E., Diest, K., and Atwater, H.A. Unity-order index change in transparent conducting oxides at visible frequencies. *Nano Letters*, 10(6): 2111–2116, May 2010. doi: 10.1021/nl1006307.
- [56] Campione, S., Brener, I., and Marquier, F. Theory of epsilon-near-zero modes in ultrathin films. *Physical Review B*, 91(12):121408, March 2015. doi: 10.1103/physrevb.91.121408.
- [57] Silveirinha, M.G. and Engheta, N. Theory of supercoupling, squeezing wave energy, and field confinement in narrow channels and tight bends using ϵ -near-zero metamaterials. *Physical Review B*, 76(24):245109, December 2007. doi: 10.1103/physrevb.76.245109.
- [58] Bello, F., Page, A.F., Pusch, A., Hamm, J.M., Donegan, J.F., and Hess, O. Combining ϵ -near-zero behavior and stopped light energy bands for ultra-low reflection and reduced dispersion of slow light. *Scientific Reports*, 7(1), August 2017. doi: 10.1038/s41598-017-08342-x.

Bibliography

- [59] Hamachi, Y., Kubo, S., and Baba, T. Slow light with low dispersion and nonlinear enhancement in a lattice-shifted photonic crystal waveguide. *Optics Letters*, 34(7):1072, March 2009. doi: 10.1364/ol.34.001072.
- [60] Mero, M., Clapp, B.R., Jasapara, J.C., Rudolph, W.G., Ristau, D., Starke, K., Krüger, J., Martin, S., and Kautek, W. On the damage behavior of dielectric films when illuminated with multiple femtosecond laser pulses. *Optical Engineering*, 44(5):051107, May 2005. doi: 10.1117/1.1905343.
- [61] Streetman, B. and Banerjee, S. *Solid State Electronic Devices*. Pearson Education, Limited, 2014. ISBN 9780133356038.
- [62] Amotchkina, T., Trubetskov, M., Hahner, D., and Pervak, V. Characterization of e-beam evaporated Ge , YbF_3 , ZnS , and LaF_3 thin films for laser-oriented coatings. *Applied Optics*, 59(5):A40, December 2019. doi: 10.1364/ao.59.000a40.
- [63] Papatryfonos, K., Angelova, T., Brimont, A., Reid, B., Guldin, S., Smith, P.R., Tang, M., Li, K., Seeds, A.J., Liu, H., and Selviah, D.R. Refractive indices of MBE-grown $\text{Al}_x\text{Ga}_{1-x}\text{As}$ ternary alloys in the transparent wavelength region. *AIP Advances*, 11(2):025327, February 2021. doi: 10.1063/5.0039631.
- [64] Green, M.A. Self-consistent optical parameters of intrinsic silicon at 300k including temperature coefficients. *Solar Energy Materials and Solar Cells*, 92(11):1305–1310, November 2008. doi: 10.1016/j.solmat.2008.06.009.
- [65] Tsang, H.K., Wong, C.S., Liang, T.K., Day, I.E., Roberts, S.W., Harpin, A., Drake, J., and Asghari, M. Optical dispersion, two-photon absorption and self-phase modulation in silicon waveguides at 1.5 μm wavelength. *Applied Physics Letters*, 80(3):416–418, January 2002. doi: 10.1063/1.1435801.
- [66] Garmire, E. Resonant optical nonlinearities in semiconductors. *IEEE Journal of Selected Topics in Quantum Electronics*, 6(6):1094–1110, November 2000. doi: 10.1109/2944.902158.
- [67] Sheik-Bahae, M., Hagan, D.J., and Stryland, E.W.V. Dispersion and band-gap scaling of the electronic kerr effect in solids associated with two-photon absorption. *Physical Review Letters*, 65(1):96–99, July 1990. doi: 10.1103/physrevlett.65.96.
- [68] Liddell, H.M. *Computer-aided techniques for the design of multilayer filters*. A. Hilger, 1981. ISBN 0852742339.

Bibliography

- [69] Diekmann, M. Spektrum: software for optical interference coatings. Software, 2002. Laser Zentrum Hannover e.V., Hollerithallee 8, 30419 Hannover, Germany.
- [70] Van Rossum, G. and Drake, F.L. *Python 3 Reference Manual*. CreateSpace, Scotts Valley, CA, 2009. ISBN 1441412697.
- [71] Chen, W., Liu, B., Song, Y., Chai, L., Cui, Q., Liu, Q., Wang, C., and Hu, M. High pulse energy fiber/solid-slab hybrid picosecond pulse system for material processing on polycrystalline diamonds. *High Power Laser Science and Engineering*, 6, 2018. doi: 10.1017/hpl.2018.20.
- [72] Wu, C., Li, M., Huang, Y., and Rong, Y. Cutting of polyethylene terephthalate (PET) film by 355 nm nanosecond laser. *Optics & Laser Technology*, 133: 106565, January 2021. doi: 10.1016/j.optlastec.2020.106565.
- [73] Jeong, S.Y., Lee, C.W., Lee, J.U., Ma, Y.W., and Shin, B.S. Laser-induced biochar formation through 355 nm pulsed laser irradiation of wood, and application to eco-friendly pH sensors. *Nanomaterials*, 10(10):1904, September 2020. doi: 10.3390/nano10101904.
- [74] Miyata, K., Petrov, V., and Noack, F. High-efficiency single-crystal third-harmonic generation in BiB_3O_6 s. *Optics Letters*, 36(18):3627, September 2011. doi: 10.1364/ol.36.003627.
- [75] Vernay, A., Boutou, V., Félix, C., Jegouso, D., Bassignot, F., Chauvet, M., and Boulanger, B. Birefringence phase-matched direct third-harmonic generation in a ridge optical waveguide based on a KTiOPO_4 single crystal. *Optics Express*, 29(14):22266, June 2021. doi: 10.1364/oe.432636.
- [76] Dmitriev, V.G., Gurzadyan, G.G., and Nikogosyan, D.N. *Handbook of Non-linear Optical Crystals*. Springer, 2013. ISBN 9783540467939.
- [77] Gapontsev, V.P., Tyrtyshtnyy, V.A., Vershinin, O.I., Davydov, B.L., and Oulianov, D.A. Third harmonic frequency generation by type-i critically phase-matched LiB_3O_5 crystal by means of optically active quartz crystal. *Optics Express*, 21(3):3715, February 2013. doi: 10.1364/oe.21.003715.
- [78] Walther, T., Larsen, M.P., and Fry, E.S. Generation of fourier-transform-limited 35-ns pulses with a ramp-hold-fire seeding technique in a ti:sapphire laser. *Applied Optics*, 40(18):3046, June 2001. doi: 10.1364/ao.40.003046.

Bibliography

- [79] Rodríguez, C. and Rudolph, W. Modeling third-harmonic generation from layered materials using nonlinear optical matrices. *Optics Express*, 22(21):25984, October 2014. doi: 10.1364/oe.22.025984.
- [80] Rodríguez, C., Günster, S., Ristau, D., and Rudolph, W. Frequency tripling mirror. *Optics Express*, 23(24):31594, November 2015. doi: 10.1364/oe.23.031594.
- [81] Škoda, V., Vanda, J., and Uxa, S. A comparison of LIDT behavior of metal-dielectric mirrors in ns and ps pulse regime at 1030 nm with regard to the coating technology. In Exarhos, G.J., Ristau, D., Gruzdev, V.E., Menapace, J.A., and Soileau, M., editors, *Laser-Induced Damage in Optical Materials 2017*. SPIE, November 2017. doi: 10.1117/12.2280628.
- [82] Negres, R.A., Stolz, C.J., Thomas, M.D., and Caputo, M. 1064-nm, nanosecond laser mirror thin film damage competition. In Gruzdev, V.E., Carr, C.W., Ristau, D., and Menoni, C.S., editors, *Laser-induced Damage in Optical Materials 2019*. SPIE, November 2019. doi: 10.1117/12.2531861.
- [83] Oskouei, A.K. *Design and Characterization of Frequency Tripling Mirrors*. phdthesis, University of New Mexico, April 2022. URL https://digitalrepository.unm.edu/ose_etds/85.
- [84] Piegari, A. and Flory, F. *Optical Thin Films and Coatings, From Materials to Applications*. Elsevier Science & Technology, 2013. ISBN 9780857095947.
- [85] Macleod, A. *Introduction to Optical Coatings and Thin Film Production*, chapter 13, pages 343–383. Taylor & Francis Group, 2014. ISBN 9780429193712.
- [86] Brandt, W. and Laubert, R. Unified sputtering theory. *Nuclear Instruments and Methods*, 47(2):201–209, February 1967. doi: 10.1016/0029-554x(67)90431-4.
- [87] Sigmund, P. Theory of sputtering. i. sputtering yield of amorphous and polycrystalline targets. *Physical Review*, 184(2):383–416, August 1969. doi: 10.1103/physrev.184.383.
- [88] Thompson, M.W. II. the energy spectrum of ejected atoms during the high energy sputtering of gold. *Philosophical Magazine*, 18(152):377–414, August 1968. doi: 10.1080/14786436808227358.

Bibliography

- [89] Wehner, G.K. and Anderson, G.S. The nature of physical sputtering. In Maisel, L.I. and Glang, R., editors, *Handbook of Thin Film Technology*, chapter 3. International Business Machines Corporation, Hopewell Junction, NY, USA, 1970. ISBN 0070397422.
- [90] Sakiew, W., Schrameyer, S., Jupé, M., Schwerdtner, P., Erhart, N., Starke, K., and Ristau, D. Influence of ion beam parameters onto two-dimensional optical thin film thickness distributions deposited by ion beam sputtering. *Thin Solid Films*, 682:109–120, July 2019. doi: 10.1016/j.tsf.2019.05.027.
- [91] Oliver, J.B. Analysis of a planetary-rotation system for evaporated optical coatings. *Applied Optics*, 55(30):8550, October 2016. doi: 10.1364/ao.55.008550.
- [92] Zhang, C. Single-wavelength monitoring method for optical thin-film coating. *Optical Engineering*, 43(6):1439, June 2004. doi: 10.1117/1.1719027.
- [93] Schlichting, S., Heinrich, K., Ehlers, H., and Ristau, D. Online re-optimization as a powerful part of enhanced strategies in optical broadband monitoring. In Lequime, M., Macleod, H.A., and Ristau, D., editors, *Advances in Optical Thin Films IV*, volume 8168, page 81681E. International Society for Optics and Photonics, SPIE, September 2011. doi: 10.1117/12.898557. URL <https://doi.org/10.1117/12.898557>.
- [94] Sainty, W.G. and Sainty, D.W. Multiwavelength monitoring of thin film growth using a fiber spectrometer. In Fulton, M.L., editor, *Optical and Infrared Thin Films*. SPIE, October 2000. doi: 10.1117/12.404756.
- [95] Oskouei, A.K., Emmert, L., Steinecke, M., Jupé, M., Ristau, D., Jensen, L., and Rudolph, W. Third harmonic (TH) generation: a tool to study dielectric material properties near the laser induced damage threshold (LIDT). In Gruzdev, V.E., Carr, C.W., Ristau, D., and Menoni, C.S., editors, *Laser-induced Damage in Optical Materials 2019*. SPIE, November 2019. doi: 10.1117/12.2536440.
- [96] Steinecke, M., Naran, T.A., Keppler, N.C., Behrens, P., Jensen, L., Jupé, M., and Ristau, D. Electrical and optical properties linked to laser damage behavior in conductive thin film materials. *Optical Materials Express*, 11(1): 35, December 2020. doi: 10.1364/ome.410081.

Bibliography

- [97] Tikhonravov, A.V. and Trubetskov, M.K. Optilayer software, ver. 12.83. Software, February 2019. URL <http://www.optilayer.com>. OptiLayer GmbH, Watzmannring 71, 85748 Garching b. München.
- [98] Willamowski, U., Ristau, D., and Welsch, E. Measuring the absolute absorptance of optical laser components. *Applied Optics*, 37(36):8362–8370, 1998. URL <https://doi.org/10.1364/AO.37.008362>.
- [99] Jensen, L., Balasa, I., Starke, K., and Ristau, D. Spectrally resolved laser calorimetric absorptance measurements. In Exarhos, G.J., Guenther, A.H., Lewis, K.L., Ristau, D., Soileau, M.J., and Stolz, C.J., editors, *SPIE Proceedings*. SPIE, October 2007. doi: 10.1117/12.752907.
- [100] ISO. *ISO 21254-2:2011, Lasers and laser-related equipment — Test methods for laser-induced damage threshold — Part 2: Threshold determination*. International Organization for Standardization, 2011.
- [101] Ibach, H. and Lüth, H. *Festkörperphysik*. Springer-Verlag GmbH, 2009. ISBN 9783540857952. URL https://www.ebook.de/de/product/19292250/harald_ibach_hans_lueth_festkoerperphysik.html.
- [102] Heaney, M.B. Electrical conductivity and resistivity. In *Measurement, Instrumentation, and Sensors Handbook*. CRC Press, December 2014. doi: 10.1201/b15664-29.
- [103] Valdes, L. Resistivity measurements on germanium for transistors. *Proceedings of the IRE*, 42(2):420–427, February 1954. doi: 10.1109/jrproc.1954.274680.
- [104] Nishimura, E., Ando, M., ichi Onisawa, K., Takabatake, M., and Minemura, T. Structural change during annealing of amorphous indium-tin oxide films deposited by sputtering with H₂O addition. *Japanese Journal of Applied Physics*, 35(Part 1, No. 5A):2788–2792, May 1996. doi: 10.1143/jjap.35.2788.
- [105] Ahmed, N.M., Sabah, F.A., Abdulgafour, H., Alsadig, A., Sulieman, A., and Alkhoaryef, M. The effect of post annealing temperature on grain size of indium-tin-oxide for optical and electrical properties improvement. *Results in Physics*, 13:102159, June 2019. doi: 10.1016/j.rinp.2019.102159.
- [106] Thirumoorthi, M. and Prakash, J.T.J. Structure, optical and electrical properties of indium tin oxide ultra thin films prepared by jet nebulizer spray pyrolysis technique. *Journal of Asian Ceramic Societies*, 4(1):124–132, March 2016. doi: 10.1016/j.jascr.2016.01.001.

Bibliography

- [107] Vink, T.J., Overwijk, M.H.F., and Walrave, W. The active dopant concentration in ion implanted indium tin oxide thin films. *Journal of Applied Physics*, 80(7):3734–3738, October 1996. doi: 10.1063/1.363324.
- [108] Bellingham, J.R., Phillips, W.A., and Adkins, C.J. Electrical and optical properties of amorphous indium oxide. *Journal of Physics: Condensed Matter*, 2(28):6207–6221, July 1990. doi: 10.1088/0953-8984/2/28/011.
- [109] Harry, G., Billingsley, G., Cole, G.D., Gretarsson, A., Gretarsson, E., and Penn, S. Development of aluminum gallium arsenide (AlGaAs) as an optical coating material for interferometric gravitational wave detectors. In *Optical Interference Coatings Conference (OIC) 2022*. Optica Publishing Group, 2022. doi: 10.1364/oic.2022.wb.3.
- [110] Zhang, W.W., Qi, H., Ji, Y.K., He, M.J., Ren, Y.T., and Li, Y. Boosting photoelectric performance of thin film GaAs solar cell based on multi-objective optimization for solar energy utilization. *Solar Energy*, 230:1122–1132, December 2021. doi: 10.1016/j.solener.2021.11.031.
- [111] Madhusoodhanan, S., Sabbar, A., Tran, H., Lai, P., Gonzalez, D., Mantooth, A., Yu, S.Q., and Chen, Z. High-temperature analysis of optical coupling using AlGaAs/GaAs LEDs for high-density integrated power modules. *Scientific Reports*, 12(1), February 2022. doi: 10.1038/s41598-022-06858-5.
- [112] Nkuissi, H.J.T., Konan, F.K., Hartiti, B., and Ndjaka, J.M. Toxic materials used in thin film photovoltaics and their impacts on environment. In *Reliability and Ecological Aspects of Photovoltaic Modules*. IntechOpen, January 2020. doi: 10.5772/intechopen.88326.
- [113] Steinecke, M. Entwicklung eines messverfahrens zur interferometrischen bestimmung des nichtlinearen brechwertes. Master’s thesis, Gottfried Wilhelm Leibniz Universität Hannover, February 2017.
- [114] Sheik-bahae, M., Said, A.A., and Stryland, E.W.V. High-sensitivity, single-beam n_2 measurements. *Optics Letters*, 14(17):955, September 1989. doi: 10.1364/ol.14.000955.
- [115] Steinecke, M., Kiedrowski, K., Jupé, M., and Ristau, D. Very thick mixture oxide ion beam sputtering films for investigation of nonlinear material properties. *The European Physical Journal Applied Physics*, 80(3):30301, November 2017. doi: 10.1051/epjap/2017170239.

Bibliography

- [116] Steinecke, M., Ristau, D., Jupé, M., and Kiedrowski, K. Measurement of the nonlinear refractive index in optical thin films. In Exarhos, G.J., Ristau, D., Gruzdev, V.E., Menapace, J.A., and Soileau, M., editors, *Laser-Induced Damage in Optical Materials 2017*. SPIE, March 2018. doi: 10.1117/12.2281127.
- [117] Siegman, A.E. *Lasers*. University Science Books, 1986. ISBN 0198557132.
- [118] Sheik-Bahae, M. Nonlinear refraction and optical limiting in 'thick' media. *Optical Engineering*, 30(8):1228, 1991. doi: 10.1117/12.55902.
- [119] Takeuchi, Y., Kawanaka, J., and Fujita, M. Nonlinear refractive index of a yag crystal at low temperature. In *CLEO/Europe and EQEC 2009 Conference Digest*, pages CA–P24. Optica Publishing Group, 2009. URL https://opg.optica.org/abstract.cfm?URI=CLEO_Europe-2009-CA_P24.
- [120] Samuel, P., Ensley, T.R., Hu, H., Hagan, D.J., Stryland, E.W.V., and Gaume, R. Nonlinear refractive index measurement on pure and nd doped YAG ceramic by dual arm z-scan technique. In *AIP Conference Proceedings*. AIP Publishing LLC, 2015. doi: 10.1063/1.4917845.
- [121] Steinecke, M., Kiedrowski, K., Jupé, M., Wienke, A., and Ristau, D. Nonlinear optical switching in thin film coatings in relation to the damage threshold. In Carr, C.W., Ristau, D., and Menoni, C.S., editors, *Laser-Induced Damage in Optical Materials 2022*. SPIE, December 2022. doi: 10.1117/12.2642756.
- [122] Steinecke, M., Jupé, M., Wienke, A., and Ristau, D. Ultrafast switching with nonlinear optics in thin films. *Applied Optics*, December 2022. doi: 10.1364/ao.478075.

List of Figures

2.1	Schematic representation of third harmonic generation	9
2.2	The Effect of different phase mismatches	10
2.3	Spectral dispersion of the refractive index	11
2.4	Phase matching with birefringence in LBO	12
2.5	Schematic of a periodically poled conversion medium	13
2.6	Intensity development for different phase matching approaches	13
2.7	Intensity development for different QPM approaches	14
2.8	Mechanisms of photoionization	16
2.9	Avalanche ionization	17
3.1	Dispersion of the nonlinear refractive index in semiconductors	26
4.1	Reflection, transmission, and refraction at an interface	28
4.2	Angular reflectance for s- and p-polarized light	28
4.3	Internal intensity enhancement in a QWOT-stack.	32
4.4	Spectral transmittance of a band-pass design	33
4.5	Internal intensity enhancement in a band-pass-stack.	34
5.1	The KBS-like characteristics of band-pass designs	36
5.2	The shift of the refractive index caused by the Kerr effect	38
5.3	Behavior of a KBS during a single pulse	40
5.4	Characteristic switching behavior of a KBS	41
5.5	Optimized switching curve	44
5.6	Transmittance of an optimized KBS	44
5.7	KBS-simulation for a Gaussian beam profile	46
6.1	A two-stage THG-process	48
7.1	Schematic drawing of an IBS coating chamber	53
7.2	Example for monitoring at a single wavelength	54
7.3	Picture of the coating machine used for production of KBS	56
7.4	Spectral intensity distribution of the LDLS measured by the HR-BBM	59
7.5	Variation of the refractive index for TM coatings	60

List of Figures

7.6	Layer thickness accuracy for FTM	61
8.1	Spectral transmittance of ITO-single layers	65
8.2	LIDT-setup and exemplary damage morphology of ITO layers	65
8.3	DIC-microscopy of annealed ITO layers	67
8.4	XRD-measurements of differently annealed ITO layers	68
8.5	SEM-images of annealed ITO layers	68
8.6	Refractive index and k-value for thermally treated ITO layers	69
8.7	Electrical resistivity of thermally treated ITO	70
8.8	LIDT of thermally treated ITO	71
8.9	Damage morphologies of ITO for different annealing temperatures	72
8.10	Schematic representation of a GaAs-KBS	73
8.11	Transmission of different GaAs-KBS	74
8.12	Image of a GaAs-KSB after the deposition process	74
9.1	Setup for the characterization of FTM	76
9.2	Original laser spectrum for FTM characterization	77
9.3	Gaussian filter and filtered laser spectrum	77
9.4	Interferometric setup for determination of the nonlinear refractive index	78
9.5	Exemplary interferogram and its FFT	79
9.6	2D-phase distribution retrieved from interferogram	79
9.7	1D-phase distribution retrieved from the 2D-distribution	80
9.8	Exemplary measurement of the nonlinear refractive index	81
9.9	Experimental setup for the measurement of optical switching	82
9.10	Spectral intensity distribution of the TruLase 5050 Laser	83
9.11	Signals recorded during switching measurement	83
9.12	Reference signal over waveplate rotation	84
9.13	Calibration of the reference diode for KBS-measurements	85
9.14	Setup for the measurement of optical switching and LIDT	85
10.1	Spectral transmittance and internal field enhancement of the FTM under test	88
10.2	Third harmonic generated by the FTM under test	88
10.3	Spectral investigation of generated third harmonic	89
10.4	Spectral investigation of generated third harmonic with filtered fun- damental	90
10.5	Measurement of the nonlinear refractive index for an ITO-Layer	92
10.6	Measurement of the nonlinear refractive index for a GaAs-Layer	93
10.7	Transmittance of a KBS design and sample after deposition	94

List of Figures

10.8 Intensity-dependent transmittance and reflectance of an ITO-KBS . . .	95
10.9 Losses of an ITO-KBS at varying intensities	95
10.10 Repeatability of the changes in reflectance and transmittance	96
10.11 Intensity-dependent transmittance and reflectance of a GaAs-KBS . . .	97
10.12 Losses of a GaAs-KBS at varying intensities	98
10.13 Characterization at different repetition frequencies.	98
10.14 Transmittance, Reflectance, and optical losses of KBS-sample for LIDT measurements	99
10.15 Characteristic damage curve and damage morphology for KBS-sample	100

List of Tables

3.1	The nonlinear refractive indices of the most commonly used oxidic coating materials	22
7.1	Spectral ranges and resolutions for the high-resolution broadband monitor	58

Publications

Peer Reviewed

- [1] M. Steinecke, M. Jupé, A. Wienke, and D. Ristau. Ultrafast switching with nonlinear optics in thin films. *Applied Optics*, 62(7):B202, Feb. 2023.
- [2] A. K. Oskouei, M. Lenzner, L. A. Emmert, M. Jupé, T. Willemsen, M. Steinecke, D. Ristau, and W. Rudolph. Damage threshold affected by the spatiotemporal evolution of femtosecond laser pulses in multilayer structures. *Optical Engineering*, 61(7):071602, 2022.
- [3] M. Steinecke, T. A. Naran, N. C. Keppler, P. Behrens, L. Jensen, M. Jupé, and D. Ristau. Electrical and optical properties linked to laser damage behavior in conductive thin film materials. *Optical Materials Express*, 11(1):35–47, 2021.
- [4] M. Steinecke, H. Badorreck, M. Jupé, T. Willemsen, L. Hao, L. Jensen, and D. Ristau. Quantizing nanolaminates as versatile materials for optical interference coatings. *Applied Optics*, 59(5):A236–A241, 2020.
- [5] H. Badorreck, M. Steinecke, L. Jensen, D. Ristau, M. Jupé, J. Müller, R. Tonneau, P. Moskovkin, S. Lucas, A. Pflug, et al. Correlation of structural and optical properties using virtual materials analysis. *Optics Express*, 27(16):22209–22225, 2019.
- [6] M. Steinecke, K. Kiedrowski, M. Jupé, and D. Ristau. Very thick mixture oxide ion beam sputtering films for investigation of nonlinear material properties. *The European Physical Journal Applied Physics*, 80(3):30301, 2017.

Not Reviewed

- [1] D. Zuber, S. Kleinert, A. Tajalli, M. Steinecke, M. Jupé, I. Babushkin, D. Ristau, and U. Morgner. $\chi(3)$ and $\chi(5)$ effects in thin gradient HfO₂-layers. In *Optica Advanced Photonics Congress 2022*. Optica Publishing Group, 2022.
- [2] D. Zuber, S. Kleinert, A. Tajalli, M. Steinecke, M. Jupé, I. Babushkin, D. Ristau, and U. Morgner. Third harmonic generation and $\chi(5)$ effects in thin gradient hfo₂ layers. In *European Physical Journal Web of Conferences*, volume 267, page 01043, 2022.

Publications

- [3] M. Steinecke, K. Kiedrowski, M. Jupé, A. Wienke, and D. Ristau. Nonlinear optical switching in thin film coatings in relation to the damage threshold. In *Laser-Induced Damage in Optical Materials 2022*, volume 12300, pages 101–109. SPIE, 2022.
- [4] M. Steinecke, M. Jupé, A. Wienke, and D. Ristau. Ultrafast switching with nonlinear optics in thin films. In *Optical Interference Coatings*, pages FA–1. Optica Publishing Group, 2022.
- [5] M. Steinecke, M. Jupé, A. Wienke, and D. Ristau. Switching of ultrashort laser pulses by nonlinear optics in thin films. In *Nonlinear Optics and its Applications 2022*, page PC121430Z. SPIE, 2022.
- [6] S. Paschel, M. Steinecke, F. Carstens, M. Jupé, A. Wienke, D. Ristau, T. Tolenis, and L. Ramalis. Environmental dependencies on the lidt of all-silica glad mirrors for 355 nm. In *Laser-Induced Damage in Optical Materials 2022*. SPIE, 2022.
- [7] P. Henning, M. Jupé, S. Bruns, T. Melzig, M. Steinecke, A. Wienke, and M. Vergöhl. Manufacturing of si-based hybrid metamaterials for increasing the refractive index in interference coatings. In *Optical Interference Coatings*, pages MD–1. Optica Publishing Group, 2022.
- [8] D. Zuber, S. Kleinert, A. Tajalli, M. Steinecke, M. Jupé, L. Jensen, D. Ristau, and U. Morgner. Third harmonic generation from thin gradient ternary mixture layers. In *CLEO: Applications and Technology*, pages JTh3A–70. Optica Publishing Group, 2021.
- [9] D. Zuber, S. Kleinert, A. Tajalli, M. Steinecke, M. Jupé, L. Jensen, D. Ristau, and U. Morgner. Study of third harmonic generation from thin gradient hfxalyoz layers. In *The European Conference on Lasers and Electro-Optics*, page ce_9_5. Optica Publishing Group, 2021.
- [10] M. Lenzner, A. K. Oskouei, L. A. Emmert, M. Jupé, T. Willemsen, M. Steinecke, D. Ristau, and W. Rudolph. Spatio-temporal evolution of femtosecond laser pulses in dielectric multi-layers controlling the damage behavior. In *Laser-Induced Damage in Optical Materials 2021*, volume 11910, pages 57–62. SPIE, 2021.
- [11] M. Jupé, E. Atkocaitis, E. Zutautaitė, K. Kiedrowski, M. Steinecke, L. Herrero, L. Jensen, U. Kimbaraite, M. Šciuka, and A. Melninkaitis. Experimental study of lidt scaling laws for metallic coatings: effect of pulse duration within fifteen orders of magnitude. In *Laser-Induced Damage in Optical Materials 2021*, volume 11910, page 119100G. SPIE, 2021.
- [12] S. Balendat, M. Jupé, M. Steinecke, L. Jensen, A. K. Oskouei, W. Rudolph, D. Zuber, U. Morgner, and D. Ristau. Manufacturing and characterization of frequency tripling

Publications

- mirrors. In *The European Conference on Lasers and Electro-Optics*, page cd_p_33. Optical Society of America, 2021.
- [13] M. Steinecke, J. Matthes, L. Jensen, M. Jupé, and D. Ristau. Electrical and optical properties linked to laser damage behavior in indium tin oxide. In *Laser-induced Damage in Optical Materials 2020*, volume 11514, page 115140K. SPIE, 2020.
- [14] W. Rudolph, A. K. Oskouei, L. A. Emmert, M. Steinecke, M. Jupé, L. O. Jensen, and D. Ristau. Nonlinear optics using interference coatings - opportunities and challenges. In *Optical Interference Coatings Conference (OIC) 2019*. OSA, 2019.
- [15] A. K. Oskouei, L. Emmert, M. Steinecke, M. Jupé, D. Ristau, L. Jensen, and W. Rudolph. Third harmonic (th) generation: a tool to study dielectric material properties near the laser induced damage threshold (lidt). In *Laser-induced Damage in Optical Materials 2019*, volume 11173, pages 132–138. SPIE, 2019.
- [16] A. K. Oskouei, L. Emmert, W. Rudolph, M. Steinecke, M. Jupé, L. Jensen, and D. Ristau. Design and conversion scaling laws of frequency tripling mirrors based on dielectric coating stacks. In *Optical Interference Coatings*, pages ThB–2. Optical Society of America, 2019.
- [17] M. Jupé, T. Willemsen, H. Liu, M. Steinecke, L. Jensen, and D. Ristau. Manufacturing of quantized nanolaminates. In *Optical Interference Coatings*, pages TB–4. Optical Society of America, 2019.
- [18] M. Jupé, M. Steinecke, H. Badorreck, L. Jensen, D. Ristau, A. K. Oskouei, and W. Rudolph. Efficient third harmonic generation in optical thin films. In *Nonlinear Optics*, pages NF2A–5. Optical Society of America, 2019.
- [19] L. Jensen, M. Jupé, M. Steinecke, and D. Ristau. Ultra-fast kerr switches on the basis of dielectric multi-layer films. In *Nonlinear Optics*, pages NM3A–6. Optical Society of America, 2019.
- [20] M. Steinecke, T. Kellermann, M. Jupé, D. Ristau, and L. Jensen. Measurement setup for the determination of the nonlinear refractive index of thin films with high nonlinearity. In *Laser-Induced Damage in Optical Materials 2018: 50th Anniversary Conference*, volume 10805, pages 243–250. SPIE, 2018.
- [21] M. Steinecke, M. Jupé, K. Kiedrowski, and D. Ristau. Measurement of the nonlinear refractive index in optical thin films. In *Laser-Induced Damage in Optical Materials 2017*, volume 10447, pages 179–191. SPIE, 2018.
- [22] A. K. Oskouei, S. Baur, L. Emmert, M. Jupe, T. Willemsen, M. Steinecke, L. Jensen, D. Ristau, and W. Rudolph. Femtosecond laser-induced modifications of frequency

Publications

tripling mirrors. In *Laser-Induced Damage in Optical Materials 2018: 50th Anniversary Conference*, volume 10805, pages 236–242. SPIE, 2018.

Curriculum Vitae

Personalien

Name Morten Steinecke
geboren am 08.05.1992 in Hannover
ledig, deutsch

Schulbildung

07/2011 Abitur, Gymnasium Goetheschule Hannover

Studium

10/2011 - 02/2017 Leibniz Universität Hannover, Studium der Physik
Thema der Masterarbeit: *Entwicklung eines Messverfahrens zur interferometrischen Bestimmung des nichtlinearen Brechwertes*, durchgeführt am Laser Zentrum Hannover e.V.

02/17 Abschluss: Master of Science (Physik)

seit 04/17 Promotionsstudium and der Lebniz Universität Hannover

Beruflicher Werdegang

03/2017 - 03/2023 Laser Zentrum Hannover e.V.,
Wissenschaftlicher Mitarbeiter

seit 03/2023 Laser Zentrum Hannover e.V.,
Leiter Arbeitsgruppe Optische Beschichtungen

Danksagung

Zum Gelingen dieser Arbeit haben viele Leute beigetragen. Zuerst möchte ich mich bei Prof. Dr. Detlev Ristau für die Möglichkeit bedanken, die Arbeit unter seiner Betreuung am Laser Zentrum Hannover durchführen zu können. Auch für seine konstruktiven Ratschläge und die wissenschaftliche Anleitung während der Durchführung meiner Arbeit möchte ich mich bedanken. Prof. Dr. Rudolph und Prof. Dr. Morgner möchte ich sowohl für die lehrreiche Zusammenarbeit im THG-Projekt, als auch für die freundliche Übernahme des Korreferats danken. Bedanken möchte ich mich auch bei meinen Abteilungsleitern Dr. Lars Jensen und Dr. Andreas Wienke für die Unterstützung im Vorfeld und beim Verfassen der Arbeit. Ein großer Dank geht an Andreas für das gründliche Korrekturlesen der Arbeit.

Ein Besonderer Dank gebührt Dr. Marco Jupé. Ihm verdanke ich sowohl die grundlegende Idee Kerr-Band-Schalters, als auch eine unschätzbare Menge an moralischer und fachlicher Unterstützung. Ohne diese Hilfe sowohl bei der Theorie als auch im Labor wäre meine Arbeit nicht in dieser Form möglich gewesen.

Meinen Studenten Sebastian Balendat und Tank Ankit Naran danke ich für Ihre engagierte Arbeit und ihre guten Ergebnisse, die viel zu meiner Arbeit beigetragen haben. Für die spannende Mitarbeit im Labor und die allgemein sehr gute Zusammenarbeit während des THG-Projekts möchte ich mich auch bei Dr. Amir Khabbazi Oskouei bedanken.

Ein spezieller Dank geht an meine Kollegen Sebastian Paschel, Kevin Kiedrowski, Jan Steinbeck und Tarik Kellermann. Sie haben mir dabei geholfen, die wichtigen Dinge im Arbeitsalltag nicht aus den Augen zu verlieren. Meinem PMA-Kollegen Holger Baddoreck danke ich mich für die spaßige Zusammenarbeit der letzten Jahre und ganz besonders für die unschätzbare Unterstützung mit klugen Softwarelösungen für meine Probleme. Auch bei meinem Senordoktoranden Thomas Willemsen möchte ich mich für die gute Bürogemeinschaft und meine ersten Unterweisungen im Beschichten bedanken.

Weiter möchte ich mich bei Heiner Mädebach für die viele Hilfe zu LIDT-Messungen und Sebastian Schlichting für das Beantworten meiner unzähligen Fragen zum BBM und der ReCalc-Software bedanken. Besonderer Dank gebührt auch Dr. Man-

Danksagung

fred Diekmann für die vielen hilfreichen Gespräche und dem Erfüllen meiner Änderungswünsche an der *Spektrum32*-Software. Weiter geht ein großes Dankeschön geht an die gesamte Abteilung der optischen Komponenten (und der Laserkomponenten davor) für die dauerhafte große Hilfsbereitschaft. Auch bei Jan Düsing und Jürgen Koch möchte ich mich dafür bedanken, dass ich während der Arbeit als Gast stets freundlich an ihren Lasersystemen aufgenommen wurde.

Schließlich möchte ich mich noch bei meiner Familie und ganz besonders bei meiner Freundin Kezia bedanken, ohne deren nicht endende Unterstützung diese Arbeit so nicht möglich gewesen wäre.

Erklärung der Selbständigkeit

Hiermit versichere ich, dass ich die vorliegende Arbeit selbstständig verfasst und keine anderen als die angegebenen Quellen und Hilfsmittel genutzt habe, dass ich alle Stellen der Arbeit, die wörtlich oder sinngemäß aus anderen Quellen übernommen wurden, als solche kenntlich gemacht habe und dass die Arbeit in gleicher oder ähnlicher Form noch keiner Prüfungsbehörde vorgelegt sowie noch nicht veröffentlicht wurde.

Hannover, den

Morten Steinecke